Master's thesis

NTNU
Norwegian University of Science and Technology
Faculty of Natural Sciences
Department of Materials Science and Engineering

Amalie Grønvold

# $CO_2$-Free Aluminium Production: Production of $AlCl_3$ by Carbochlorination of Bauxite

Master's thesis in Chemical Engineering and Biotechnology
Supervisor: Christian Rosenkilde
June 2021

NTNU
Norwegian University of
Science and Technology

Amalie Grønvold

# $CO_2$-Free Aluminium Production: Production of $AlCl_3$ by Carbochlorination of Bauxite

Master's thesis in Chemical Engineering and Biotechnology
Supervisor: Christian Rosenkilde
June 2021

Norwegian University of Science and Technology
Faculty of Natural Sciences
Department of Materials Science and Engineering

NTNU
Norwegian University of
Science and Technology

# Preface

The present master's thesis entitled «$CO_2$-Free Aluminium Production: Production of $AlCl_3$ by Carbochlorination of Bauxite» is written during the spring of 2021 at the Department of Material Science and Engineering, Norwegian University of Science and Technology (NTNU) as a finalisation of a 5-year Master's degree in Chemical Engineering and Biotechnology. The work is a continuation of a literature review and specialisation project on the same topic, conducted by the author at the department during the summer and autumn of 2020, respectively. Furthermore, the work is a collaboration project between NTNU and Hydro. Supervision has primarily been given by Christian Rosenkilde, Bjørnar Gjesdal and Espen Tjønneland Wefring at Hydro, Porsgrunn. All experimental work was performed by the author at NTNU, with three exceptions; Carbochlorination experiments and XRF measurements, which were conducted at Hydro, Porsgrunn with the assistance of Gjesdal and the ICP-MS measurements, which were performed by Laurentius Tijhuis (NTNU).

Trondheim, June 2021
Amalie Grønvold

# Acknowledgement

Acknowledgements are directed towards Christian Rosenkilde[1], Bjørnar Gjesdal[1] and Espen Tjønneland Wefring[1] for their guidance throughout this and the previous semester, and for being available on short notice whenever I needed help. Their expertise has been vital for this work.

Special thanks are directed towards Yingda Yu[2] for helping me with investigations in SEM. My greatests gratitudes are also directed towards Maria Tsoutsouva[2] for her instructions in sample preparation for XRD measurements, and for helping me interpret the results. Furthermore, I would like to thank Elin Harboe Albertsen[2] for her instructions on sample preparation for BET measurements.

Finally, thanks to all of you for allowing me to take part in such an exiting project.

[1]Hydro, Porsgrunn

[2]Department of Materials Science and Engineering, NTNU, Trondheim

# Abstract

The commercial production of primary Al relies on energy-intensive processes from the late 1800s: the Bayer and the Hall–Héroult process. Large direct emissions of $CO_2$ are associated with the latter, and with the attention directed towards a green transition into a climate neutral society, new routes for the production of Al are sought out. The carbochlorination of Bayer $Al_2O_3$, followed by the electrolysis of $AlCl_3$ into metallic Al poses as an alternative production route. Direct emissions of $CO_2$ are also associated with these processes, as it is produced during the carbochlorination of $Al_2O_3$. However, as the $CO_2$ can be produced in considerably high concentration, technologies such as $CO_2$ capture and storage are possible. The overall production can therefore be regarded as a $CO_2$-free production route for Al. Carbochlorinating Al bearing minerals instead of $Al_2O_3$, allows for the energy intensive Bayer process to be avoided. Research has indicated that the carbochlorination of bauxite serves as the most promising option.

The objective of this work was to obtain a better understanding of how the Al component in bauxite reacts during carbochlorination, and how it is affected by the carbochlorination of the other constituents in bauxite. This was achieved by subjecting calcined bauxite to carbochlorination for 15, 45 and 75 min. A specially built three-stage reactor was utilised during the carbochlorination, to obtain information of how the presence of produced gaseous metal chlorides affect the carbochlorination of unreacted $Al_2O_3$ in the bauxite. To detect any changes in the bauxite due to carbochlorination, the calcined bauxite was characterised before and after carbochlorination. X-ray fluorescence analyses were performed to detect any changes in chemical composition and to calculate the elemental removal during carbochlorination. The elemental removal was also estimated thermodynamically by Gibbs energy minimisation. X-ray diffraction were performed to assess any changes in the phases present at the different stages of carbochlorination. To detect any changes in particle morphology, investigations in scanning electron microscope were performed. Furthermore, the Brunauer–Emmett–Teller surface areas were measured to document any changes during the carbochlorination. The purity of the produced metal chlorides was evaluated by inductively coupled plasma mass spectrometry.

Results revealed that bauxite could be readily carbochlorinated at 700 °C. The reaction sequence on element basis during carbochlorination were found to be Fe, Si/Ti and lastly Al, differing from what was thermodynamically estimated. A near-zero elemental removal of Al was found in the bottom bed after 75 min of carbochlorination, indicating how severely the carbochlorination of Al containing species were affected by the produced metal chlorides. Negative elemental removals for Si, Ti and Al in the bottom bed after 15 min of carbochlorination indicated that the gaseous metal chlorides of these species chlorinated unreacted bauxite, resulting in the deposition of the respective oxides in the reactor bed material. The formation of $\alpha$-$Al_2O_3$ during carbochlorination was revealed by X-ray diffraction, which may be related to the decreasing bauxite surface area observed as the carbochlorination proceeded. A porous structure was found to be developed on

the surface of the $Al_2O_3$ particles during carbochlorination. Furthermore, a significant decrease in particle size could be observed in the longer carbochlorination experiment. It was therefore suggested that the $Al_2O_3$ particles develop a growing porous structure during carbochlorination, which eventually consumes the outer reactive part of the particle, leaving behind a smaller, possibly non-reactive, particle.

# Sammendrag

Den kommersielle produksjonen av primær Al er avhengig av to energiintensive prosesser fra slutten av 1800-tallet: Bayer og Hall-Héroult prosessen. Store direkte $CO_2$-utslipp er knyttet til sistnevnte, og med oppmerksomheten rettet mot en grønn overgang til et klimanøytralt samfunn, har nye produksjonsmetoder for Al blir undersøkt. Karboklorinering av Bayer $Al_2O_3$, etterfulgt av elektrolyse av $AlCl_3$ til metallisk Al, er en mulig produksjonsrute. Direkte $CO_2$-utslipp er også forbundet med disse prosessene, ettersom det produseres under karboklorinering av $Al_2O_3$. Derimot, siden $CO_2$ kan produseres i svært høye konsentrasjoner, er teknologier som $CO_2$-fangst og lagring mulig. Den totale prosessen kan derfor betraktes som en $CO_2$-fri produksjonsrute for Al. Å karboklorinere Al-bærende mineraler i stedet for $Al_2O_3$, gjør det mulig å unngå den energiintensive Bayer-prosessen. Forskning har indikert at karboklorinering av bauxitt er det mest lovende alternativet.

Målet med dette arbeidet var å få en bedre forståelse av hvordan Al komponenten i bauxitt reagerer under karboklorinering og hvordan den påvirkes av karboklorineringen av de andre komponentene i bauxitt. Dette ble oppnådd ved å utsette kalsinert bauxitt for karboklorinering i 15, 45 og 75 min. En spesialbygd treetasjesreaktor ble benyttet under karboklorineringen for å få informasjon om hvordan tilstedeværelsen av produserte metallklorider i gassfasen påvirker karboklorineringen av ureagert $Al_2O_3$ i bauxitten. For å avdekke eventuelle endringer i bauxitt på grunn av karboklorinering, ble den kalsinerte bauxitten karakterisert før og etter karboklorinering. Røntgenfluorescensanalyser ble utført for å avdekke eventuelle endringer i kjemisk sammensetning og for å beregne elementomsetningen under karboklorinering. Dette ble også estimert termodynamisk ved hjelp av Gibbs energiminimering. Røntgendiffraksjon ble utført for å identifisere eventuelle endringer i fasesammensetning ved de forskjellige stadiene av karboklorineringen. For å oppdage endringer i partikkelmorfologi ble det utført undersøkelser i skanning elektronmikroskop. Videre ble Brunauer–Emmett–Teller-overflatearealet målt for å dokumentere eventuelle endringer under karboklorineringen. Renheten til de produserte metallkloridene ble målt ved hjelp av induktivt koblet plasmamassespektrometri.

Resultatene avslørte at bauxitt lett kunne karboklorineres ved 700 °C. Reaksjonsrekkefølgen under karboklorinering på elementbasis ble funnet til å være Fe, Si / Ti og til slutt Al, noe som skilte seg fra det som er termodynamisk estimert. Den nederste etasjen hadde cirka 0% omsetning av faser som inneholdt Al etter karboklorinering i 75 min, noe som indikerte at karboklorinieringen av Al faser ble svært negativt påvirket av tilstedeværelsen av de produserte metallkloridene. Negativ elementomsetning av Si, Ti og Al i den nederste etasjen indikerte at metallkloridene av disse elementene klorinerte ureagert bauxitt, noe som resulterte i avsetningen av deres respektive oksider i reaktormaterialet. Dannelsen av $\alpha$-$Al_2O_3$ under karboklorinering ble påvist ved røntgendiffraksjon, noe som kan vært relatert til den observerte reduksjonen i overflatearealet til bauxitt etterhvert som karboklorineringen foregikk. En porøs struktur ble dannet på overflaten av $Al_2O_3$-partiklene under karboklorinering. I tillegg ble det observert en signifikant reduksjon i partikkelstørrelse i det

lengste karboklorineringsforsøket. Det ble derfor foreslått at $Al_2O_3$-partiklene utvikler en voksende porøs struktur under karboklorinering, som til slutt konsumerer den ytre reaktive delen av partikkelen, og etterlater en mindre, muligens ikke-reaktiv, partikkel.

# Contents

# List of Abbreviations

**Alcoa** Aluminum Company of America

**ASP** Alcoa smelting process

**BET** Brunauer–Emmett–Teller

**DTA** Differential thermal analysis

**EDS** Energy-dispersive X-ray spectroscopy

**GEM** Gibbs energy minimisation

**GHG** Greenhouse gas

**IC** Ion chromatography

**ICP-MS** Inductively coupled plasma mass spectrometry

**LOI** Loss on ignition

**PBR** Packed bed reactor

**RT** Room temperature

**SCM** Shrinking core model

**SEM** Scanning electron microscope

**TGA** Thermogravimetric analysis

**XRD** X-ray diffraction

**XRF** X-ray fluorescence

# Chapter 1

# Introduction

## 1.1 Background

In line with the Paris Agreement, the EU aims towards a climate neutral society by 2050, having net-zero emissions of greenhouse gases (GHGs)[1]. This energy transition requires a high quantity of metals, especially non-ferrous metals[2]. Non-ferrous metals are the building blocks of several climate technologies, including batteries, solar panels, wind turbines and energy-efficient buildings, among others. Al is one such metal. As a conductor of heat and electricity, Al is for instance widely used in renewable energy technologies such as wind and solar power. Furthermore, the light weight of Al allowed European produced cars in 2019 to prevent the emission of 50 million tons of $CO_2$ in vehicle emissions during the lifetime of these cars. Because of its versatile properties, Al has become the second most used metal, only beaten by steel. Its production is only expected to increase, and by 2050, the annual global demand of Al is expected increase twofold to threefold[3].

Despite the many advantages of the use of Al, the commercial production of primary Al relies on energy-intensive processes from the late 1800s: the Bayer and the Hall–Héroult process[4]. The Al production starts with the mining of an aluminous ore, as pure Al cannot be found in nature due to its affinity to oxygen. Typically, this ore is bauxite. Alumina ($Al_2O_3$) is extracted from bauxite through the Bayer process[5]. In this process, Fe and other impurities in the bauxite are removed as red mud, which is an industrial waste which cannot be introduced back into the environment, due to its high alkalinity[2, 6]. Per tonne $Al_2O_3$ produced, 1.5 tonne of red mud is produced[7]. In addition, the Bayer process alone accounts for $\sim$27% of the total cost of Al production[4]. After $Al_2O_3$ is extracted by the Bayer process, it is transferred to the Hall–Héroult process. In this process $Al_2O_3$, dissolved in molten cryolite ($Na_3AlF_6$) with ions of $AlF_4^-$ and $F^-$, is electrolytically converted to metallic Al at $\sim$960 °C[8]. The overall reaction for this process can be written as

$$2\,Al_2O_3 + 3\,C \rightleftharpoons 4\,Al + 3\,CO_2\,. \tag{1.1}$$

As the Hall–Héroult process utilises carbon anodes which are consumed during electrolysis, $CO_2$ is produced in the process. In comparison to other metallurgical processes, the Hall–Héroult process has low productivity and consumes a significant amount of energy[4]. In general, 2.5% of the world anthropogenic $CO_2$ equivalent emissions are due to the production of Al, including both direct and indirect emissions.

Due to the high energy consumption and the resulting carbon footprint from the consumption of the carbon anodes, alternatives to the Hall–Héroult process have been sought out[9]. Only one alternative production route has been attempted at a commercial scale; the Alcoa

smelting process (ASP)[10]. This was a process developed by Aluminum Company of America (Alcoa) in the 1960s-80s, with the goal of producing Al in an more energy efficient manner, with better working conditions and fewer environmental problems[11]. The route for producing Al by the ASP was as follows:

1. extraction of $Al_2O_3$ from bauxite by the Bayer process
2. carbochlorination of $Al_2O_3$ at 900-1200 K, according to

$$2\,Al_2O_3 + 6\,C + 6\,Cl_2 \rightleftharpoons 4\,AlCl_3 + 6\,CO_2 \tag{1.2}$$

3. electrolysis of $AlCl_3$ in a molten salt bath at 700 °C, according to

$$2\,AlCl_3 \rightleftharpoons 2\,Al + 3\,Cl_2[12]. \tag{1.3}$$

Among the several advantages of the ASP over the Hall–Héroult process, the most apparent were the significantly lower working temperature, relatively high current densities, and most importantly, the use of non-reacting graphite anodes[2, 11]. The use of these anodes eliminated the costly production of consumable carbon anodes and the direct emission of $CO_2$ during electrolysis[2]. In theory, the production of 1 kg of Al through the Hall–Héroult process and the ASP creates the same amount of $CO_2$, as $CO_2$ is released in the carbochlorination of $Al_2O_3$[9]. However, the $CO_2$ produced by carbochlorination is fairly pure, due to it being produced in high concentrations. This allows for the implementation of $CO_2$ capture and storage. The advantages of the ASP were partly offset by certain disadvantages, such as the addition of an extra step to the overall process when Bayer $Al_2O_3$ is carbochlorinated prior to electrolysis, and $AlCl_3$ being highly corrosive to several construction materials[11]. By the 1980s the ASP was discontinued, presumably due to the wrong reactor design and operating parameters[10].

The use of chlorination as a step in metal production, is not a new idea[13]. Chlorination has been used as a process in metallurgy, either for the production of metals or for the extraction and separation of oxides from minerals. For instance, the Kroll process, where $TiO_2$ is carbochlorinated into $TiCl_4$ and reacted with Mg to produce metallic Ti and $MgCl_2$. The use of $Cl_2$ in extractive metallurgy has attracted considerable attention due to the high reactivity of certain chlorinating agents, the relatively low temperatures during chlorination and cheap and easy accessibility of reagents, among others[14]. Chlorination of an ore or oxide can be described as

$$MO + Cl_2 \rightleftharpoons MCl_2 + O_2[13]. \tag{1.4}$$

Whether the reaction proceeds to the left or right is determined by whether the metal oxide has a higher affinity for chloride than oxygen. In the cases where the reaction is thermodynamically favoured to proceed to the left-hand-side, a reducing agent must be added for the chlorination to proceed. This is usually some kind of carbon species, and the resulting carbochlorination can be described as

$$MO + Cl_2 + C \rightleftharpoons MCl_2 + CO. \tag{1.5}$$

At the same time as the launch of the ASP, a lot of research was conducted on carbochlorination as a way of producing $AlCl_3$ for the production of metallic Al, and on carbochlorination as a way of extracting $Al_2O_3$ from raw materials[12]. The research consisted mostly of thermodynamical assessments of different reaction routes and the assessment of kinetic properties. As production of Al by carbochlorination, is not directly dependent on the use of pure $Al_2O_3$, the direct carbochlorination of aluminous ores serves as a possible production route. By direct carbochlorination of the raw materials, the energy-intensive Bayer process could be avoided and other aluminous ores in addition to bauxite could be utilised. However, carbochlorination of raw materials is complex, due to several different metal chlorides being produced at the same time[12]. The carbochlorination of raw materials such as leucite rocks, plagioclase and fly ash have been studied, however most of the research has been directed towards the carbochlorination of bauxite and kaolinite[15–31]. A study performed by Landsberg (1975), revealed that bauxite reacts at a significantly higher rate than kaolinite[15].

In line with the discontinuation of the ASP in the 1980s, the interest of carbochlorination of raw materials declined[9]. However, with the need for more environmentally sustainable solutions, the interest has rekindled. A recent investigation by Namboothiri and Mallick (2017), about the carbochlorination of bauxite to produce metallic Al, shows promise[7]. They achieved an overall bauxite conversion of up to 94% during carbochlorination. The produced $AlCl_3$ had a purity of more than 90% and was purified by simple condensation and reductive distillation, which resulted in a purity of more than 99.8%. The production of metallic Al was successfully achieved, by electrolysis of this $AlCl_3$.

In the context of a green transition into a climate neutral society, Hydro is investigating the possibility of a $CO_2$-free production route of Al, through the ASP. The economic advantage of this process over the Hall–Héroult process, is strongly dependent on how $AlCl_3$ is produced[7]. If Bayer $Al_2O_3$ is used for the carbochlorination, the benefits of this process would be partly negated. In the light of the recent investigations by Namboothiri and Mallick, and several promising studies from the 1970s and 80s, the carbochlorination of bauxite serves as a promising alternative production route for $AlCl_3$. Figure 1.1 displays an suggestion of how an overall process of producing Al by carbochlorination of bauxite could look like. Bauxite would be carbochlorinated using CO as a reduction agent producing several different metal chlorides. After carbochlorination, the produced metal chlorides would have to be separated and purified. $AlCl_3$ would then be converted to metallic Al by electrolysis. Due to the fairly high purity of the produced $CO_2$ during carbochlorination, $CO_2$ could either be stored, or transformed back to CO, essentially making the process $CO_2$-free, in regards to direct emissions. To avoid the loss of $Cl_2$ to carbochlorination of the impurity species of bauxite, the $Cl_2$ would have to be recovered from the produced metal chlorides. This could either be done by directly retrieving the $Cl_2$ from the metal chlorides by reacting it with $O_2$ or $H_2O$, or by selling the metal chlorides commercially and produce new $Cl_2$.

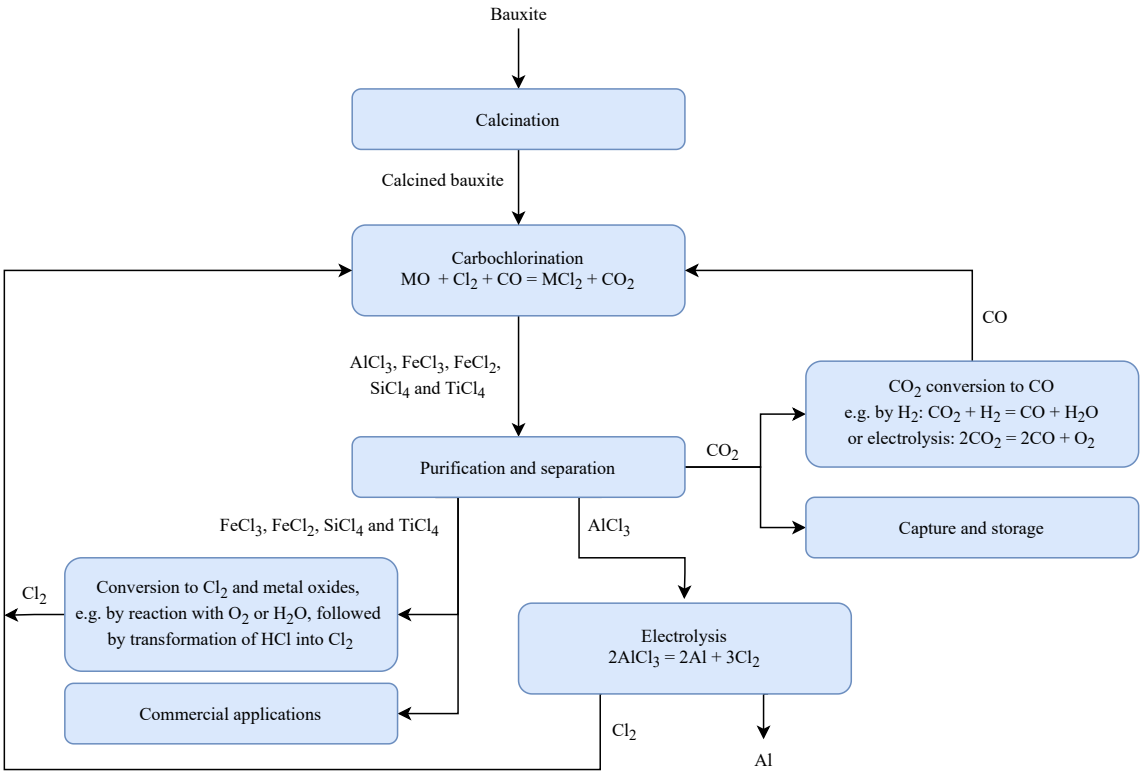


**Figure 1.1:** Overview of a possible reaction route for the production of Al by carbochlorination of bauxite.

## 1.2 Objective

Bauxite is an inhomogeneous material, consisting of several oxides. How these different oxides react, affect the carbochlorination of the other constituents of bauxite. Of special interest is how the Al component is affected by this. As much of the research conducted in the 70s and 80s focused on the kinetics of carbochlorination, little is known about what happens to the different constituents of bauxite as it is carbochlorinated. The objective of this work was therefore to obtain a better understanding of how the Al component in bauxite reacts during carbochlorination, and how it is affected by the carbochlorination of the other constituents of bauxite. To achieve this, bauxite was prepared and subjected to carbochlorination in a specially built packed bed reactor (PBR), with three bauxite powder beds placed on top of each other, as to represent the top, middle and bottom part of a powder bed. The purpose of this reactor was to investigate of how the presence of produced gaseous metal chlorides from the carbochlorination of the other constituents of bauxite in the top bed, affect the carbochlorination of the unreacted Al components in the middle and bottom bed. To measure this effect, and how the Al components were carbochlorinated in relation to the other species in bauxite, the elemental removal of the different constituents of bauxite during carbochlorination were measured. This was also estimated thermodynamically by Gibbs energy minimisation (GEM). Changes in the chemical composition and phases present in bauxite were measured by X-ray fluorescence (XRF) and X-ray diffraction. Brunauer–Emmett–Teller (BET) surface area measurements and investigations

in scanning electron microscope (SEM) were performed to record any changes in surface area and particle morphology. Inductively coupled plasma mass spectrometry (ICP-MS) was performed on the metal chlorides produced by carbochlorination to get an indication of the composition of the produced metal chlorides. The possible scale up of the carbochlorination of bauxite and the application of a kinetic model was also briefly assessed.

# Chapter 2

# Theoretical Background – Earlier Work

## 2.1 Bauxite

Bauxite is a naturally occurring heterogeneous rock consisting of different minerals, typically found in tropical areas. As the worlds primary source of Al, most Al made today is extracted from bauxite[32]. About 50% of bauxite consist of the aluminium (oxy)hydroxides gibbsite ($Al(OH)_3$), diaspore (AlOOH) and boehmite (AlOOH)[5]. The composition of bauxite is somewhat dependent on where it is found as gibbsite is typically the most dominating phase in bauxite found in tropical areas, whereas bauxite found in temperate areas typically consist of more diaspore and boehmite[32]. Water makes up 10-20% of bauxite, while the rest are mainly Si, Ti and Fe containing compounds[7, 15, 20, 33].

## 2.2 Thermal Treatment of $Al_2O_3$

Prior to carbochlorination, bauxite needs to be calcined to remove free and bound moisture[17]. If any moisture is present during carbochlorination, $Cl_2$ can be lost to the formation of HCl. In addition, the produced metal chlorides are very hygroscopic. Therefore, exposure to moisture may make the produced $AlCl_3$ unsuitable for subsequent electrolysis to produce metallic Al. It has been found that the reactivity of bauxite is highly dependent on how it was thermally treated prior to carbochlorination[15].

As bauxite mainly consists of aluminium (oxy)hydroxides, it is relevant to look at how these (oxy)hydroxides behave during thermal treatment. During thermal treatment the (oxy)hydroxides transform into what is referred to as alumina[34]. However, alumina can refer to several different materials, as alumina is characterised by prominent polymorphism. The type of alumina produced is dependent on its precursor. Figure 2.2 gives an overview of the alumina types formed by thermal treatment of the different alumina precursors in bauxite. Ultimately, the thermal treatment of all types of aluminas will lead to the formation of corundum, also known as $\alpha$-$Al_2O_3$, if the temperatures are high enough. $\alpha$-$Al_2O_3$ is the thermodynamically stable polymorph. The intermediate alumina phases, produced on the way to $\alpha$-$Al_2O_3$ are known as transition aluminas. These phases are irreversibly formed and maintained during cooling to room temperature (RT). The reason for the different transformation routes is commonly believed to be a result of the structural similarities between the precursors and the transition aluminas formed.

The thermal treatment of gibbsite has two possible transformation routes, dependent on particle size and the heating rate. It has been reported that using a particle size smaller than 5 µm and heating rate smaller than 1 K $min^{-1}$, results in the formation of $\chi$-$Al_2O_3$[35].

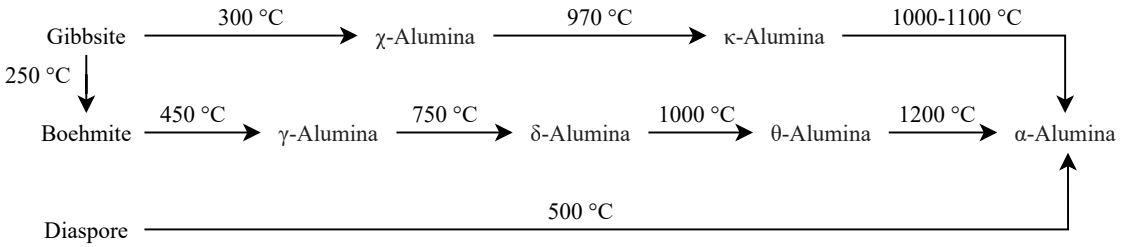


**Figure 2.1:** Overview of the alumina phases produced during thermal treatment of typical (oxy)hydroxides in bauxite. The temperatures are indicative. Adapted from [34].

Using a particle size larger than 80 µm and heating rate higher than 10 K $min^{-1}$, however, results in the formation of boehmite. The reason for the different reaction paths, is believed to be because of local hydrothermal conditions occurring when the particle size and heating rate are too large, promoting the formation of boehmite[36]. When $\chi$-$Al_2O_3$ is thermally treated at higher temperatures, it turns into $\kappa$-$Al_2O_3$ before transforming into $\alpha$-$Al_2O_3$[37]. Boehmite, on the other side, is transformed into $\gamma$-$Al_2O_3$ when the temperature increases, before transforming into $\delta$-, $\theta$- and finally $\alpha$-$Al_2O_3$. Diaspore is the only alumina precursor which directly transforms into $\alpha$-$Al_2O_3$.

The thermal transformations of boehmite, gibbsite and diaspore have been reported as topotactical[34, 37, 38]. This means that the morphology of the precursor material is retained in their respective transition aluminas[34]. For instance, by thermally treating fibrous boehmite, fibrous $\gamma$-$Al_2O_3$ can be obtained. Boehmite, produced by the thermal treatment of bauxite, typically has a lamellar structure. Several different habits of boehmite have been reported, including rhombic and hexagonal. Gibbsite has an hexagonal lattice with an lamellar structure[39]. Diaspore has a hexagonal close packed structure[35].

The transformation of both gibbsite and boehmite into transition aluminas result in a significant increase in surface area[34]. Figure 2.2 displays the surface area development of pseudoboehmite (poorly crystalline boehmite) during thermal treatment, as an example of how the surface area can develop through the transition aluminas. The obtained surface areas are highly dependent on how the transition alumina is produced. For instance, when very small platelets of gibbsite are thermally treated, they can produce $\chi$-$Al_2O_3$ with surface areas as high as 400 $m^2$ $g^{-1}$[40]. As the transition aluminas are ultimately transformed into $\alpha$-$Al_2O_3$, the surface area decreases[34]. High surface area $\alpha$-$Al_2O_3$ has been obtained, but no one exceeding 50 $m^2$ $g^{-1}$.

The crystal structure of transition aluminas such as $\gamma$- and $\chi$-$Al_2O_3$ display highly distorted and poorly crystalline structures[41]. This can be seen by the broad and diffuse reflections in the XRD diffractograms of these transition aluminas. Characterisation of these transition aluminas are therefore extremely difficult. This characterisation is made more difficult by the similarity of the XRD diffractograms, resulting from $\chi$- and $\gamma$-$Al_2O_3$. Because of this, the crystal structure of $\chi$-alumina is still unknown[37]. Both hexagonal and cubic structures have been suggested. The crystal structure of $\gamma$-$Al_2O_3$ is also somewhat uncertain, but it has generally been accepted that it has an defective non-stoichiometric spinel structure[34].

As these transition aluminas are transformed into higher temperature transition aluminas, the ordering of the structures increase. This results in sharper reflections in the XRD diffractograms of these high temperature transition aluminas.

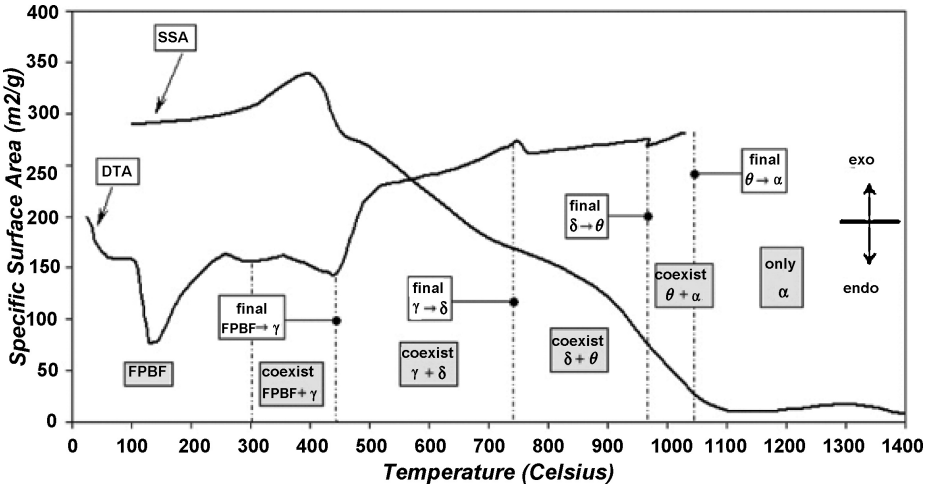


**Figure 2.2:** Evolution of surface area during thermal treatment of pseudoboehmite. The transition aluminas produced at the different temperatures are indicated. Obtained from [42].

## 2.3 Carbochlorination

### 2.3.1 The Thermodynamics of Carbochlorination of Bauxite

Carbochlorination of bauxite is a complex process involving the carbochlorinaiton of several different species at once[12]. Table 2.1 indicate the reactions taking place during the carbochlorination of the major constituents of bauxite[21, 26, 43]. The Gibbs energies and enthalpies of the reactions are also included[44]. As seen by the negative Gibbs energies, all the reactions are thermodynamically favoured to occur at 700 °C. All the metal chlorides formed by Reactions 2.1-2.5 are gaseous at 700 °C.

**Table 2.1:** Carbochlorination reactions of the major constituents of bauxite[21, 26, 43]. $\Delta G^{700}$ is the Gibbs energy of the reaction at 700 °C and $\Delta H^{700}$ is the enthalpy of the reaction at 700 °C. The values are obtained from [44].

| Number | Reaction | $\Delta G^{700}$ [kJ mol$^{-1}$] | $\Delta H^{700}$ [kJ mol$^{-1}$] |
|---|---|---|---|
| (2.1) | $Al_2O_3 + 3\,Cl_2 + 3\,CO \rightleftharpoons 2\,AlCl_3 + 3\,CO_2$ | -196 | -366 |
| (2.2) | $SiO_2 + 2\,Cl_2 + 2\,CO \rightleftharpoons SiCl_4 + 2\,CO_2$ | -196 | -320 |
| (2.3) | $TiO_2 + 2\,Cl_2 + 2\,CO \rightleftharpoons TiCl_4 + 2\,CO_2$ | -274 | -388 |
| (2.4) | $Fe_2O_3 + 3\,Cl_2 + 3\,CO \rightleftharpoons 2\,FeCl_3 + 3\,CO_2$ | -494 | -332 |
| (2.5) | $Fe_2O_3 + 2\,Cl_2 + 3\,CO \rightleftharpoons 2\,FeCl_2 + 3\,CO_2$ | -468 | -578 |

As the carbochlorination proceeds, it is possible for the produced metal chlorides to undergo an exchange reaction with unreacted metal oxides[45]. For instance the reaction between $AlCl_3$ and $Fe_2O_3$ according to

$$Fe_2O_3 + 2\,AlCl_3 \rightleftharpoons 2\,FeCl_3 + Al_2O_3 \tag{2.6}$$

and the reaction between $Al_2O_3$ and $SiCl_4$

$$2\,Al_2O_3 + 3\,SiCl_4 \rightleftharpoons 4\,AlCl_3 + 3\,SiO_2 \text{[21, 31].} \tag{2.7}$$

Thus, the metal oxides in bauxite can either be carbochlorinated by CO and $Cl_2$ introduced to the system or by produced metal chlorides.

### 2.3.2 Reducing Agents

As seen in Reactions 2.1-2.5, the different constituents of bauxite react with $Cl_2$ and some kind of carbon reducing agent to produce their respective metal chlorides[46]. The chlorination of several of the bauxite constituents is not thermodynamically possible without this carbon reducing agent[9]. Which reducing agent is used affects the carbochlorination[19]. When carbochlorinating $Al_2O_3$ and Al bearing minerals, three different carbon reducing agents have typically been utilised; solid carbon, such as coke and graphite, gaseous CO and gaseous phosgene ($COCl_2$)[43, 46].

When solid carbon is used as the reduction agent, the carbon is usually either admixed with the metal oxide or coated on the metal oxide surface[46]. It has been found that the distance between the metal oxides and carbon strongly affects the carbochlorination rate. During carbochlorination of $TiO_2$, high carbochlorination rates can be obtained if the distance between the metal oxide and carbon is $< 30$ µm. Analogous studies for this effect in the carbochlorination of $Al_2O_3$ has not been performed to the best of the authors' knowledge, however the effect has been observed qualitatively[19, 45]. This poses a problem in the carbochlorination of bauxite, as it produces gaseous products[12]. The carbochlorination may proceed at a high rate until enough metal oxide has been removed, so that the distance between the metal oxide and the carbon becomes more than 30 µm[46]. Alcoa used solid carbon in their ASP[11].

By using gaseous CO as a reduction agent instead of solid carbon, the problems with the carbon-metal oxide distance can be eliminated[46]. Landsberg (1975) found that admixed samples of $\gamma$-$Al_2O_3$ and carbon carbochlorinate at much higher rates when $O_2$ is introduced, facilitating the production of CO[15]. A study by Milne and and Wibberley (1978) obtained similar results, finding that $\gamma$-$Al_2O_3$ carbochlorinated at a higher rate when CO was used as the reducing agent[47].

The use of $COCl_2$ holds a kinetic advantage as it holds both the reducing and chlorinating agent in the same molecule[15]. This allows for reduction and chlorination to occur in one step. Toth et al. (1981, 1982) compared the use of CO and $Cl_2$ to that of $COCl_2$ during carbochlorination of $\gamma$-$Al_2O_3$ in two different studies[48, 49]. They found that the use of $COCl_2$ resulted in higher carbochlorination rates up to about 920 K. At higher temperatures the carbochlorinations had the same rate. The decomposition of $COCl_2$ into CO and $Cl_2$

at higher temperatures was suggested as the reason for this. From an economic point of view however, the use of $COCl_2$ as a reduction agent has its downsides as it is the most expensive reduction agent to obtain. In addition, it is very toxic[46].

### 2.3.3 Carbochlorination of $Al_2O_3$

Most carbochlorination studies on $Al_2O_3$ has revolved around the carbochlorination of $\gamma$-$Al_2O_3$ and to some extent $\alpha$-$Al_2O_3$[15, 19, 47–52]. It is generally accepted that $\gamma$-$Al_2O_3$ carbochlorinates at a much higher rate than $\alpha$-$Al_2O_3$, which is relatively nonreactive. When carbochlorinating $\gamma$-$Al_2O_3$ with CO and $Cl_2$ at 500 °C, Landsberg (1975) obtained near full conversion[15]. XRD measurements revealed that the residue only contained nonreactive $\alpha$-$Al_2O_3$. Smith et al. (1982) attempted the carbochlorination of $\alpha$-$Al_2O_3$, however, it did not carbochlorinate to a significant extent[19]. The reason for the higher reactivity of $\gamma$- over $\alpha$-$Al_2O_3$, has by several authors been suggested to be a result of the much higher surface area of $\gamma$-$Al_2O_3$[7, 21].

A reaction mechanism for the carbochlorination of $Al_2O_3$ has been proposed by Szabó et al. (1991), as follows[53]:

1. The diffusion of $Cl_2$ and CO through a thin boundary layer surrounding the $Al_2O_3$ particle.
2. The chemisorption of $Cl_2$ to the $Al_2O_3$ surface.
3. CO binding to the chemisorbed $Cl_2$ resulting in the formation of a monolayer of activated $COCl_2$-type complexes. If $COCl_2$ is in the vicinity of the $Al_2O_3$ surface, step 2. and 3. occurs as one. The formation of this $COCl_2$-type monolayer was first suggested by Milne (1976)[54].
4. The formation of $CO_2$ and $AlCl_3$.
5. Desorption of $CO_2$ and $AlCl_3$.

### 2.3.4 Direct Carbochlorination

Landsberg (1975) investigated the carbochlorination kinetics of direct carbochlorination of bauxite. The bauxite investigated had a composition of 65% $Al_2O_3$, 21% $SiO_2$, 2.7% $TiO_2$, 8.7% $Fe_2O_3$ after calcination at 1000 °C and 1200 °C, to transform the Al component in bauxite into $\gamma$- and $\alpha$-$Al_2O_3$, respectively. Figure 2.3 displays the typical weight loss curves obtained during carbochlorination of bauxite with CO and $Cl_2$. The weight loss curve for the carbochlorination of $\gamma$-$Al_2O_3$ is also included. A general increase in carbochlorination rate was found as the reaction temperature increased, except for the case between 600 and 800 °C. The carbochlorination was found to proceed at an initial rapid rate before slowing down, despite considerable amounts of bauxite was unreacted. Landsberg argued that this decrease in carbochlorination rate was a result of a decrease in surface area and the residual bauxite containing nonreactive $SiO_2$ and $\alpha$-$Al_2O_3$. Figure 2.4 displays the element remaining during the carbochlorination of bauxite. These curves were representative for carbochlorination at temperatures between 300-600 °C and with either carbon or CO as the

reducing agent. $TiO_2$ and $Fe_2O_3$ were found to be preferentially removed over $SiO_2$ and $Al_2O_3$.

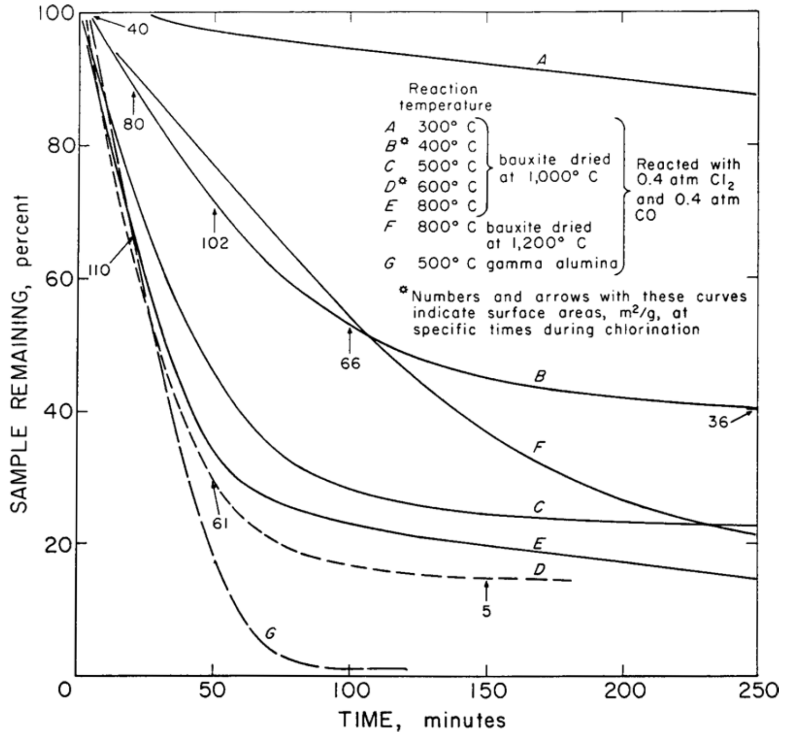


**Figure 2.3:** Weight loss curves during carbochlorination of bauxite and $\gamma$-$Al_2O_3$. Obtained from [15].

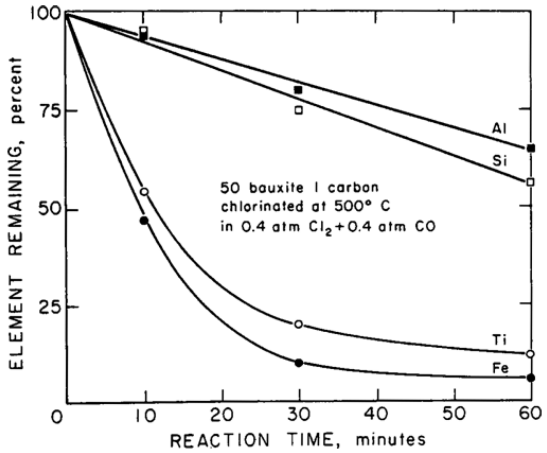


**Figure 2.4:** Typical weight loss curves for the elements in bauxite during carbochlorination at 300-600 °C. Obtained from [15].

Namboothiri and Mallick (2017) investigated the direct carbochlorination of bauxite in a fluidised bed reactor[7]. The bauxite investigated had a composition of 64% $Al_2O_3$, 3% $SiO_2$, 2.2% $TiO_2$, 8.5% $Fe_2O_3$ and a loss on ignition (LOI) of 25% and was calcined at 750 °C before carbochlorination to form $\gamma$-$Al_2O_3$ in the bauxite. Petroleum coke was

used as the reduction agent. A two-condenser reactor setup was used, to allow for simple distillation of the gaseous carbochlorination products. Carbochlorination at 800-850 °C resulted in conversions as high as 94% and with $AlCl_3$ purities of more than 90%.

### 2.3.5 Sequential Carbochlorination

As the Ti and Fe compounds are typically found to be carbochlorinated first in the carbochloriation of bauxite, the possibility of a two-stage sequential carbochlorination of bauxite has been investigated[7, 33]. The idea is to perform a preliminary carbochlorination at a lower temperature, selectively removing the Ti and Fe species in the bauxite. Afterwards, a second carbochlorination would be performed at a higher temperature, carbochlorinating the $Al_2O_3$ component in bauxite.

Raval and Dixit (1979) investigated the sequential carbochlorination of bauxite at different temperatures and with different amounts of coke added[33]. Coke acted as a reducing agent in these experiments. The bauxite investigated had a composition of 63.4% $Al_2O_3$, 2.14% $TiO_2$, 3.01% $Fe_2O_3$ and a loss on ignition (LOI) of 30.9% and was calcined at 1273 K before carbochlorination. They found that by carbochlorinating the bauxite at 773 K with three times the stoichiometric amount of coke was needed to carbochlorinate more than 90% of all the Ti and Fe species. The $Al_2O_3$ loss was of the order of 2.5%. More Ti and Fe could be removed at higher coke contents or higher temperatures, however, this also resulted in the increased removal of $Al_2O_3$. Carbochlorination of the Ti- and Fe-free bauxite was successfully performed afterwards at elevated temperatures.

Similar investigations were performed by Namboothiri and Mallick (2017). The characteristics of the bauxite investigated is described in Section 2.3.4[7]. As for Raval and Dixit, Namboothiri and Mallick found that the Ti and Fe constituents of bauxite could be removed by carbochlorination at lower temperatures. However, the extent of the Ti and Fe removal was not as severe as that obtained by Raval and Dixit. Despite using a higher temperature of 650 °C, only 50-60% and 60-80% of the Ti and Fe impurities, respectively, could be removed. The carbochlorination of the purified bauxite resulted in similar conversion and $AlCl_3$ purities as obtained by the direct carbochlorination of the bauxite.

### 2.3.6 Effect of $SiCl_4$ Addition

Milne (1975) studied the effect of $SiCl_4$ addition during carbochlorination of bauxite with CO and $Cl_2$[31]. The bauxite was previously calcined at 750 °C to form reactive $\gamma$-$Al_2O_3$. He found that the injection of $SiCl_4$ during carbochlorination decreases the rate of $SiO_2$ carbochlorination, however it also decreased the rate of $Al_2O_3$ carbochlorination as well. It was suggested that the decrease in the $Al_2O_3$ carbochlorination rate was either a result of $SiO_2$ deposition on the $Al_2O_3$ surface as a result of the chlorination of $Al_2O_3$ by $SiCl_4$ or that the $SiCl_4$ chemisorbed on the $Al_2O_3$ surface hindering the access of CO and $Cl_2$.

Landsberg (1977) studied the effect of $SiCl_4$ addition during the carbochlorination of calcined kaolinitic clay with CO and $Cl_2$[16]. When kaolinitic clay is calcined, it typically forms metakaolinite ($Al_2Si_2O_7$)[55]. The clay consisted of 40-45% $Al_2O_3$, 49-52% $SiO_2$, 1-2% $TiO_2$ and 0.5-3% $Fe_2O_3$[16]. He found that exposure to $SiCl_4$ resulted in a significant

decrease in the carbochlorination rate of the clay. When the clay was exposed to $SiCl_4$ in an inert gas stream at elevated temperature, a weight gain of 0.2-1 % and evolution of $FeCl_3$ was observed. Subsequent XRD analysis of the clay revealed the formation of mullite ($3\,Al_2O_3 \cdot 2\,SiO_2$) during the $SiCl_4$ exposure. Mullite has proved to be relatively persistent to carbochlorination[56]. The effect of prior contact to $TiCl_4$ and $FeCl_3$ was also investigated, but they were not found to have a significant effect the carbochlorination[16]. Prior exposure to $AlCl_3$ was found to slightly enhance the carbochlorination rate.

### 2.3.7 Formation of Molten Metal Chlorides

Bauxite may contain traces of alkali and earth alkali compounds[57]. Thermodynamics indicate that these carbochlorination of these alkali and earth alkali species are preferred over the carbochlorination of the main bauxite constituents[29]. Above 800 °C the respective metal chlorides of these compounds are liquid and a temperature of more than 1400 °C is needed to vaporise them. Because of these high melting and boiling points, the produced alkali and earth alkali chlorides will remain in the carbochlorination reactor as molten metal chlorides. Mehrotra et al. (1982) argued that these molten metal chlorides deposited on top of the reactive oxide surfaces and flooded the particle pores during carbochlorination of fly ash, resulting in a reduction of the carbochlorination rate. This theory has later been challenged by Dobbins (1986) as it ignored other published work which argued that the presence of alkali metal oxides catalysed the reaction, due to the formation of complexes such as $NaAlCl_4$[16, 45].

## 2.4 Separation of Metal Chlorides

The production of metallic Al from the electrolysis of $AlCl_3$, requires pure $AlCl_3$ feed[7]. The direct carbochlorination of bauxite has not yet been found to directly produce $AlCl_3$ of sufficient purity[7, 15, 33]. The other metal chlorides resulting from the carbochlorination of bauxite are $SiCl_4$, $TiCl_4$ and $FeCl_3$[7]. $AlCl_3$ must therefore be separated from these metal chlorides before the electrolysis can take place.

Distillation has been suggested as a possible separation technique, taking advantage of the difference in boiling points between the metal chlorides. The melting and boiling points of the metal chlorides are given in Table 2.2. $SiCl_4$ and $TiCl_4$ can easily be separated by this technique[17]. Despite the large difference in volatilises between $FeCl_3$ and $AlCl_3$, $FeCl_3$ cannot be fully separated from $AlCl_3$, because of the formation of the chloride complex $FeAlCl_6$. Another separation technique is therefore required for the separation of these two metal chlorides.

Reductive distillation serves as a possible alternative for the separation of $FeCl_3$ from $AlCl_3$[17]. Namboothiri and Mallick (2017) investigated the use of this separation technique on metal chlorides produced during carbochlorination of bauxite[7]. The metal chlorides had previously been distilled to remove $SiCl_4$ and $TiCl_4$. It is unspecified whether they attempted to separate some of the produced $FeCl_3$ from $AlCl_3$ through this distillation as well. They added the impure metal chlorides from the carbochlorination in a molten salt bath of NaCl-$AlCl_3$ with a metallic reducing agent, which in their experiments was Al metal

**Table 2.2:** Melting and boiling points of relevant metal chlorides. Adapted from [12].

| Metal chlorides | Melting point [°C] | Boiling point [°C] |
|---|---|---|
| $AlCl_3$ | 193 | 180 (sublimating) |
| $SiCl_4$ | -68 | 58 |
| $TiCl_4$ | -24 | 136 |
| $FeCl_2$ | 677 | 1023 |
| $FeCl_3$ | 308 | 316 |

powder[7]. Al metal powder is preferred as the metallic reducing agent, as it would not add a new species to the system[17]. The reactions taking place during the reductive distillation are

$$3\,FeCl_3 + Al \rightleftharpoons 3\,FeCl_2 + AlCl_3 \tag{2.8}$$

$$3\,FeCl_2 + 2\,Al \rightleftharpoons 3\,Fe + 2\,AlCl_3 \tag{2.9}$$

$$2\,FeCl_3 + Fe \rightleftharpoons 3\,FeCl_2 \tag{2.10}$$

$$3\,FeAlCl_6 + Al \rightleftharpoons 3\,FeCl_2 + 4\,AlCl_3 \tag{2.11}$$

$$3\,TiCl_4 + Al \rightleftharpoons 3\,TiCl_3 + AlCl_3\text{[7].} \tag{2.12}$$

As seen in the reactions, both Fe and Ti chlorides can be removed by this technique. The reduced metal chlorides have high boiling points, as seen in Table 2.2. $AlCl_3$ can therefore be separated from these chlorides by distillation. Namboothiri and Mallick (2017) produced $AlCl_3$ with a purity of $> 99.8\%$ by this method. An average $FeCl_3$ content of $\sim$1000 ppm was found in the distilled $AlCl_3$. Rapid reaction occurred at temperatures between 200-250 °C, however the reaction rate was drastically reduced when the impurity level in the crude $AlCl_3$ exceeded 5 wt%, indicating the importance of a tuned carbochlorination process producing $AlCl_3$ of sufficient quality.

## 2.5 Recovery of $Cl_2$ from the Chlorination of Impurities

In order to obtain a circular process, as described in Figure 1.1, the loss of $Cl_2$ has be reduced to a minimum. As given in Reaction 1.3, $Cl_2$ is recovered during the electrolysis of $AlCl_3$ and can therefore be recycled back to the carbochlorination reactor[12]. However, any $Cl_2$ used to chlorinate other species than $Al_2O_3$ would not be recovered by this process, thus a $Cl_2$ recovery technique is therefore needed. Two possible routes for the recovery of $Cl_2$ are

- the back-reaction to a metal oxides and $Cl_2$, and
- to sell the produced metal chlorides and produce new $Cl_2$[43].

These are two extremes of possible recovery techniques, and a number of alternatives may exist as a combination of these two.

The back-reaction to a metal oxide could be achieved either by reaction with $O_2$, hereafter called oxolysis, or by reaction with $H_2O$, also known as hydrolysis[43]. Oxolysis can be assumed to proceed according to

$$MCl_2(g) + \frac{1}{2}O_2(g) \rightleftharpoons MO(s) + Cl_2(g) \tag{2.13}$$

whereas hydrolysis can be assumed to proceed according to

$$MCl_2(g) + H_2O(g) \rightleftharpoons MO(s) + 2\,HCl(g). \tag{2.14}$$

As seen in Reaction 2.14, $Cl_2$ is not directly produced by the hydrolysis of the metal chlorides. An extra step is therefore required before $Cl_2$ is fully recovered and can be transferred back to the carbochlorination reactor. Processes for the recovery of $Cl_2$ from HCl have been developed, such as catalytic oxidation or ion exchange electrolysis[58].

If the impurity metal chlorides could be sufficiently separated and purified, the commercial application of the metal chlorides is also an option[43]. As seen in Reactions 2.2-2.5, the most common metal chlorides produced by carbochlorination of bauxite, other than $AlCl_3$, are $SiCl_4$, $TiCl_4$, $FeCl_3$ and $FeCl_2$. Table 2.3 summarises some of the applications of these metal chlorides. New $Cl_2$ for the carbochlorination can be produced by the chlor-alkali process[8].

**Table 2.3:** Application of impurity metal chlorides. Adapted from [43].

| Metal chloride | Application |
|---|---|
| $SiCl_4$ | - Intermediate compound in the high purity Si production, for the semiconductor industry and production of photovoltaic cells[59]<br>- Optical fiber manufacture[59] |
| $TiCl_4$ | - Production of metallic Ti through the Kroll process[60]<br>- Production of $TiO_2$ in the pigment industry[61] |
| $FeCl_3$ | Several applications can be found, common uses include[62]<br>- Treatment of sewage and water purification<br>- Catalyst for in Friedel-crafts reactions<br>- Pigments<br>- Oxidising agent |
| $FeCl_2$ | Few industrial applications can be found, but it has some application as a species to control the sulphide content in waste waters[63] |

Of the processes mentioned above, the oxolysis of the metal chlorides are the preferred alternative. As mentioned, the hydrolysis of the metal chlorides requires the production of $Cl_2$ from HCl, in addition to the hydrolysis reaction. When it comes to the commercial application of the metal chlorides, this would add several steps to the overall process. First the impurity metal chlorides would have to be separated and purified to meet the purity

demands for their respective applications. Furthermore, the production of new $Cl_2$ adds another step to the process. Because of this, the oxolysis of the metal chlorides is the only recovery route considered in this work.

Figure 2.5 displays the Gibbs energy of the oxolysis of the main impurity chlorides produced during carbochlorination of bauxite. As seen in the figure, oxolysis of the impurity chlorides are thermodynamically favoured at all temperatures between 0-1000 °C. The trend is that the Gibbs energy increases as the temperature is increased. This is the case for all the impurity chlorides except for $FeCl_3$ and $TiCl_4$, where the Gibbs energy is decreases as the temperature is decreased to ~300 °C. As the temperature is increased from 300 °C the Gibbs energy of these species increases.

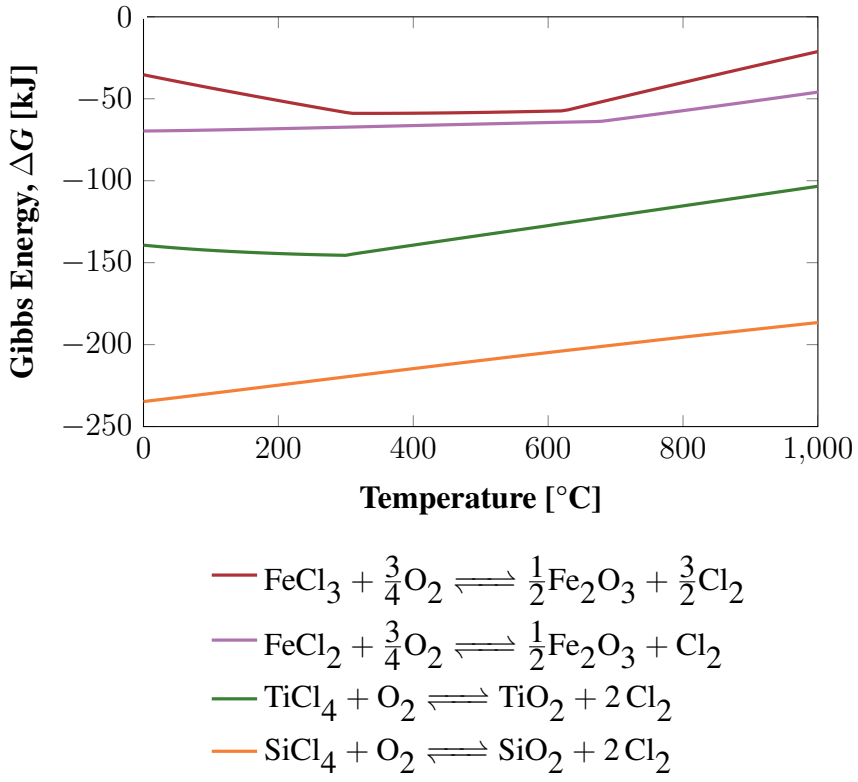


**Figure 2.5:** Gibbs Energy of the oxolysis of the impurity metal chlorides produced.

## 2.6 The Shrinking Core Model

Gas-solid reactions involve the reaction between gases and solids[64]. Several different models exist to estimate the kinetics of gas solid reactions[65]. One of these, the shrinking core model (SCM), is of particular interest in the carbochlorination of $Al_2O_3$, as it has been suggested as a suitable model for the carbochlorination of alumious fly ash[66]. Moreover, a SCM has been developed by Hydro for the carbochlorination of $Al_2O_3$ in a similar reactor setup utilised in this work[67].

The SCM describes the reactions where solid particles are being consumed as a result of the reaction, and therefore the particles "shrink"[68]. It was first proposed by Yagi and

Kunii in 1955 to describe the kinetics of carbon removal by fouling and has since then been applied to numerous systems[68, 69]. The model assumes that the particles are non-porous homogeneous spheres, reacting uniformly[65]. Furthermore, it separates between two possible rate determining steps: the surface reaction and mass transfer. The following general expressions describe the SCM according to the two different rate determining steps respectively,

$$kt = 1 - (1 - X)^{1/3} \tag{2.15}$$

and

$$kt = 1 - (1 - X)^{2/3} \tag{2.16}$$

where $k$ is a constant, $t$ is the reaction time and $X$ is conversion[66]. Some common forms of the SCM is described in Figure 2.6[70]. The upper route describes the situation where the consumption results in the production of completely gaseous species or species dissolvable in the fluid surrounding it. The lower route describes the situation where the product is a solid, depositing on the particle surface, resulting in an unchanged particle size.

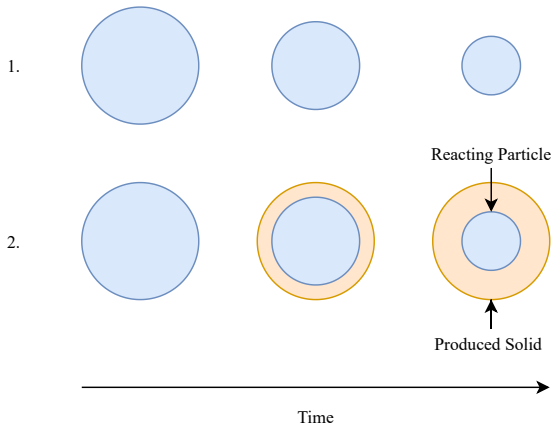


**Figure 2.6:** Different forms of the SCM. Adapted from [70].

## 2.7 Gibbs Energy Minimisation

The GEM model was developed by White et al. in 1958 for the calculation of equilibrium compositions of different complex mixtures[71]. Applicable to any equilibrium reaction, the equilibrium compositions are determined by the minimisation of free energy or total potential.

The Gibbs energy of a mixture containing $n$ chemical species, can be expressed as

$$G(X) = \sum_{i=1}^{n} g_i \tag{2.17}$$

where

$$X = (x_1, x_2, ..., x_n), \tag{2.18}$$

$$g_i = x_i \left[ c_i + \ln\left( \frac{x_i}{\bar{x}} \right) \right], \tag{2.19}$$

$$c_i = \left(\frac{G^0}{RT}\right)_i + \ln P, \tag{2.20}$$

$$\overline{x} = \sum_{i=1}^{n} x_i. \tag{2.21}$$

$x_i$ is the number of moles of the $i$th species, $R$ is the gas constant, $T$ is the temperature and $P$ is the total atmospheric pressure. The equilibrium composition can then be found by finding the set of non-negative $x_i$ values which

1. minimises the Gibbs energy of the mixture given in Equation 2.17 and
2. satisfies the following mass balance

$$\sum_{i=1}^{n} a_{ij} x_i = b_j \tag{2.22}$$

where $j = 1, 2, ..., m$, $m$ is the number different atoms, $a_{ij}$ is the number of atoms $j$ in a molecular unit of species $i$ and $b_j$ is the at% of $j$ in the original mixture.

This can be solved numerically, either by the method of steepest decent or by linear programming.

# Chapter 3

# Experimental

Bauxite supplied by Hydro from their quarries in Paragominas, Brazil was investigated in this work. Prior to delivery, the bauxite had been beneficiated to obtain a higher content of Al containing phases. Initial carbochlorination experiments and thermal analysis of a similar bauxite sample were performed in a specialisation project conducted by the author during autumn 2020. Its carbochlorination properties are further investigated in this work. The main results from the thermal analysis performed in the previous work are summarised in Appendix A, as these results are of importance in this work.

Figure 3.1 displays an overview of the experimental work performed. The blue rectangles describe what was done to the bauxite experimentally and the orange circles describes how the bauxite and product species were characterised at each stage. Bauxite was milled and sieved to a desired particle size, before it was calcined to remove all free and bound moisture. Carbochlorination of the calcined bauxite was performed afterwards in a three-stage PBR made especially for the experiments in this work. Iodometry was performed to measure the $Cl_2$ slip during carbochlorination, so that the conversion could be calculated

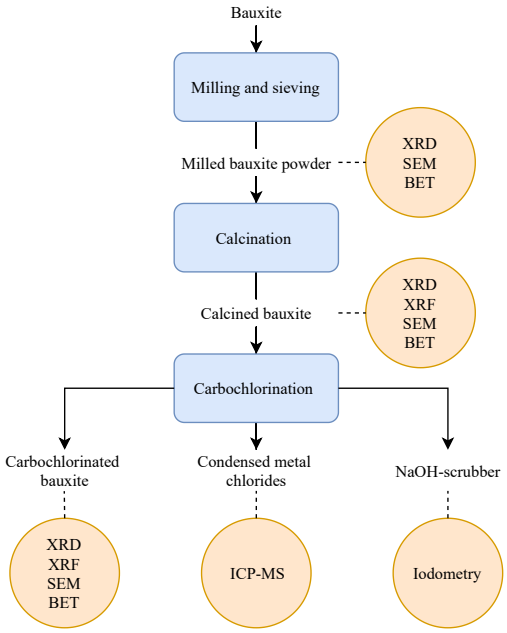


**Figure 3.1:** Overview of the experimental work performed. The blue rectangles describes what was done to the bauxite experimentally and the orange circles describes how the bauxite and product species were characterised.

## 3.1 Bauxite Preparation

The lumpy bauxite ore was ground in Retsch vibratory disk mill RS 200 with tungsten carbide (WC) as the grinding material. A grinding speed of 750-800 rpm and grinding time of 10-60 s was utilised. The bauxite was milled so that all the bauxite could pass through a 300 µm sieve. To avoid unnecessary grinding of particles already in the wanted size range, milling and sieving was performed simultaneously. Figure 3.2 display the schematics of this process.

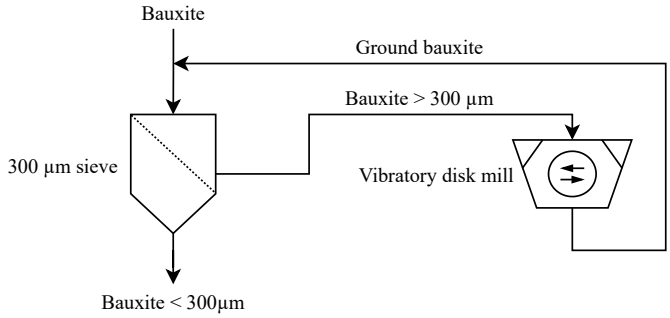


**Figure 3.2:** The milling and sieving procedure performed to obtain a particle size < 300 µm.

To remove all free and bound moisture and other volatile species, the milled bauxite powder was calcined at 750 °C in ambient air in a Nabertherm muffle furnace with a B 180 controller. The heating rate was set to 200 °C $h^{-1}$. It was determined by thermal analyses in the specialisation project that a calcination temperature of 750 °C is appropriate for this type of bauxite, as described in Appendix A. A K-type thermocouple was placed in the centre of the bauxite powder during calcination to record the temperature of the bauxite powder core. The calcination was ended after the core had reached a stable temperature between 700-750 °C for 2 h. The temperature profile of the bauxite powder core is displayed in Appendix B.

## 3.2 Carbochlorination of Bauxite

Carbochlorination experiments were performed with the assistance of Bjørnar Gjesdal at Hydro's research centre Porsgrunn. Due to local outbreaks of COVID-19, only three carbochlorination experiments were performed.

### 3.2.1 Reactor Setup

The bauxite powder was to be carbochlorinated in a PBR, where the reacting gas would enter the top of the reactor, pass through a single long powder bed and exit the reactor below this bed. To investigate how the formation of different metal chlorides produced during carbochlorination of the upper part of the powder bed affected the carbochlorination in the lower part of the powder bed, a new reactor setup was designed. In the new, modified setup, the long powder bed was separated into three smaller powder beds, placed on top of each other. The three powder beds would have to be separable during assembling and

dismantling of the reactor, so that the bauxite powders from the different beds could be collected separately. The new reactor setup compared to the old setup is displayed in Figure 3.3.

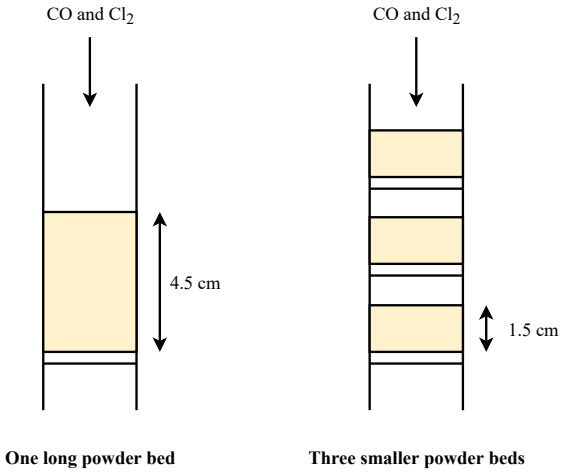


**Figure 3.3:** The old reactor setup of one long powder bed compared to the new reactor setup of three smaller powder beds. The beige sections indicate the bauxite powder.

Each of the three powder beds were designed to be its own separate reactor bed. Figure 3.4 displays the final reactor bed. The design was created in collaboration with Christian Rosenkilde, Bjørnar Gjesdal and Espen Tjønneland Wefring at Hydro and Anita Salvesen at NTNU. The reactor was constructed by Salvesen.

### 3.2.2 Experimental Procedure

The experimental PBR setup is displayed in Figure 3.5. About 1.5 g of calcined bauxite was introduced to each of the three reactor beds. The reactor was then heated to about 700 °C and purged with $N_2$. Carbochlorination was conducted at 700 °C with a flow rate of 30 NmL $min^{-1}$ $Cl_2$ and 32 NmL $min^{-1}$ CO. A slight excess of CO was utilised in an attempt to promote full conversion of $Cl_2$. The carbochlorination time was set to 15, 45 and 75 min in order to react out all Fe, reach ∼50% bauxite conversion and reach about 80-90% bauxite conversion, respectively. The measured pressure development, initial and final masses of bauxite, changes in powder bed height and temperature of the reactor during carbochlorination are given in Appendix C.

It should be noted that the PBR was made of quartz, which can carbochlorinate according to Reaction 2.2. However, based on tests performed by Bjørnar Gjesdal, it was found that the PBR did not react to a measurable extent after a number of carbochlorination cycles.

A temperature difference of 40 °C was observed between the top and bottom bed during the 45 min experiment, due to stronger heating of the top bed. An attempt to resolve this issue was made in the 15 and 75 min experiments, by introducing an empty bed below the bottom bed, however the temperature gradient persisted. The temperature was therefore increased

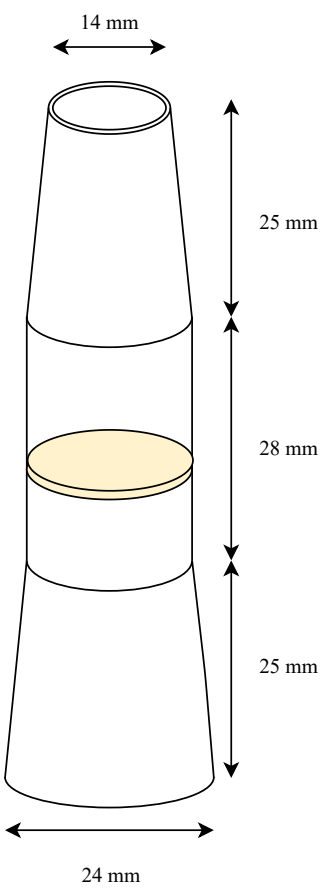


**(a)** Sketch of the reactor bed.

**(b)** The finished reactor.

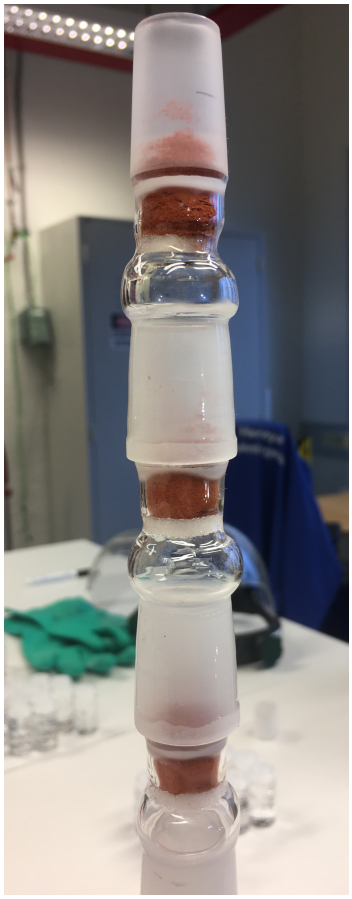

**(c)** The three reactor beds filled with bauxite, stacked on top of each other.

**Figure 3.4:** The constructed reactor bed.

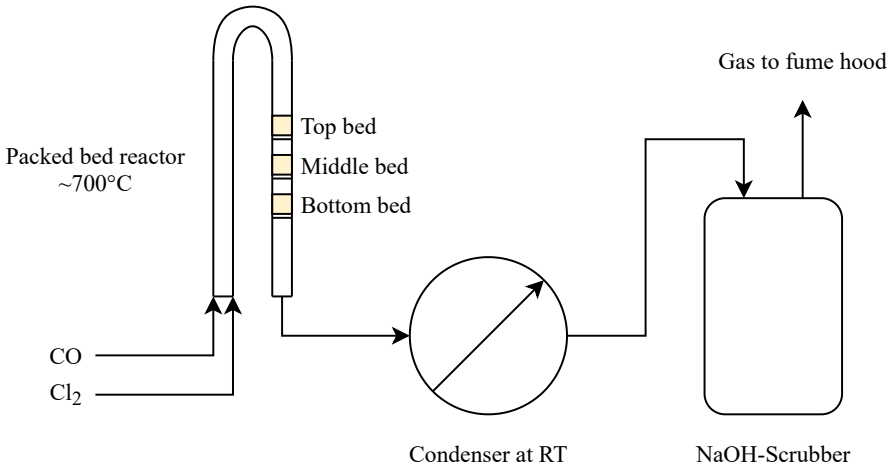


**Figure 3.5:** Simplified PBR setup for carbochlorination of bauxite. The beige areas indicate the bauxite powder.

to 710 °C for these experiments, in order to bring the temperature of the bottom bed closer to 700 °C.

Any produced gaseous metal chlorides and unreacted CO and $Cl_2$ exited the reactor and was introduced to a condenser. The reactor exit had a temperature of about 215 °C, while the condenser was kept at RT. Any non-condensable gases passed through a NaOH-scrubber. The metal chloride products in the condenser were collected and analysed by ICP-MS, conducted by Laurentius Tijhuis (NTNU).

After the carbochlorination experiment, the reactor was purged with $N_2$ to remove any residue CO and $Cl_2$ from the system. Afterwards, the reactor was cooled to RT. Any remaining bauxite in the three beds were collected separately. Hereafter these bauxite samples are called carbochlorinated bauxite. During the 75 min experiment, a hole had formed in the bottom bed, resulting in some bauxite escaping to the empty bed below. After the experiment, the carbochlorinated bauxite in the bottom bed was mixed with the escaped bauxite in the bed below, and they were analysed together as one sample.

### 3.2.3 Analysis of the NaOH-Scrubber

The NaOH-scrubber was analysed to check for $Cl_2$ slip. For the 45 and 75 min experiment, a 10 mL sample from the NaOH-scrubber was extracted every 5 min. The $Cl_2$ content of these samples was measured by iodometry, performed as follows: the 10 mL sample was diluted to 100 mL with distilled water. A 10 mL sample was obtained from the diluted solution and mixed with 25 mL of acidified 17 g $L^{-1}$ potassium iodide (KI). This sample was titrated with 0.01108 mol $L^{-1}$ sodium thiosulfate ($Na_2S_2O_3$). The reactions taking place during iodometry are explained in more detail in Appendix D.

During the 15 min experiment a 20 mL sample was extracted from the NaOH-scrubber every 2.5 min. Due to the low concentration of $Cl_2$ during this short experiment, the previously described iodometry was not be performed, as the $Cl_2$ concentration was below the resolution limit. Attempts were made to analyse these samples by ion chromatography (IC), however due to the high alkalinity of the samples, IC could not be performed. The $Cl_2$-slip of this carbochlorination experiment could therefore not be accurately measured, and is because of this not included in this work.

Before all the experiments, the NaOH-scrubber was sampled in order to calibrate its $Cl_2$ content. This calibration was conducted by extracting a 10 mL sample from the NaOH-scrubber before the experiments. The 10 mL sample was analysed by iodometry as described above.

## 3.3 Material Characterisation

### 3.3.1 Chemical Composition

The chemical composition of calcined bauxite and all samples of carbochlorinated bauxite were investigated by XRF using Hitachi X-Supreme8000 benchtop XRF elemental analyser.

The analyses were performed at Hydro's research centre in Porsgrunn with the assistance of Bjørnar Gjesdal.

### 3.3.2 Phase Identification

The phase present in the milled bauxite powder, calcined bauxite and all samples of carbochlorinated bauxite were investigated using powder XRD by Bruker D8 A25 DaVinci X-ray Diffractometer with LynxEye SuperSpeed Detector. $CuK_{\alpha}$ (1.5406 Å) radiation and fixed divergence slits with an opening of 0.2 mm were utilised. The different samples were introduced into backloading sample holders and analysed in the $2\theta$ range 10-75°, with a scan time of 2 h and step size of 0.045 ° $step^{-1}$. Due to a small offset in the goniometer, the diffractometer measures a slight offset in the peak positions. Bruker DIFFRAC.EVA was used to perform phase identification of the produced diffraction patterns for all of the analysed samples[72].

The produced metal chlorides in the condenser were also supposed to be characterised by XRD, to quantitatively determine their phase composition. To maintain the anhydrous state of the metal chlorides, they were to be analysed in capillaries prepared in a glove box. Due to difficulties during sample preparation and time constrains, these analyses were not performed.

### 3.3.3 BET Surface Area

The BET surface area of the milled bauxite powder, calcined bauxite and all samples of carbochlorinated bauxite were analysed by measuring the 5-point BET surface area by using Micromeritics 3Flex Adsorption Analyzer. Prior to the BET analyses the samples were degassed using Micromeritics SmartPrep 065. The temperature program for the degassing of the different samples are given in Table 3.1. All the samples were prepared according to the temperature program displayed in Table 3.1a, except for the milled bauxite powder. To avoid any calcination effects during the degassing of this sample, the temperature program displayed in Table 3.1b was used instead. A heating rate of 10 °C $min^{-1}$ was utilised in both temperature programs.

**Table 3.1:** Temperature programs used during degassing of the respective samples.

**(a)** Calcined bauxite and all samples of carbochlorinated bauxite.

| Step | Temperature [°C] | Time [min] |
|---|---|---|
| 1 | 30 | 10 |
| 2 | 90 | 60 |
| 3 | 220 | 780 |
| 4 | 30 | 60 |

**(b)** Milled bauxite powder.

| Step | Temperature [°C] | Time [min] |
|---|---|---|
| 1 | 30 | 10 |
| 2 | 90 | 60 |
| 3 | 110 | 1080 |
| 4 | 30 | 60 |

### 3.3.4 Characterisation in SEM

The morphology of the milled bauxite powder, calcined bauxite and all samples of carbochlorinated bauxite were investigated by SEM using Zeiss Field Emission SEM Supra 55VP in secondary electron imaging mode. Energy-dispersive X-ray spectroscopy (EDS) of certain areas of the carbochlorinated bauxite samples were also performed to obtain knowledge of their elemental composition. Sample preparation was conducted by mounting the different powder samples on a thin carbon film. The experimental conditions used during secondary electron imaging and EDS measurements are given in Table 3.2.

**Table 3.2:** Experimental conditions utilised during secondary electron imaging and EDS measurements.

| | **Secondary Electron Imaging** | **EDS** |
|---|---|---|
| **Accelerating voltage [keV]** | 5.00 | 5.00 |
| **Working distance [mm]** | ∼10 | ∼10 |
| **Aperature diameter [µm]** | 30 | 120 |
| **High Current Mode** | No | Yes |

## 3.4 Thermodynamic Calculations

Thermodynamic calculations were performed to give a theoretical estimate of how carbochlorination of bauxite would proceed. All thermodynamic calculations were performed by the use of HSC Chemistry[44].

### 3.4.1 Modelling of the Carbochlorination of Bauxite

A calculation of how the carbochlorination of the bauxite investigated in this work would proceed thermodynamically, was conducted. The equilibrium composition of the gas, solid and liquid phase during carbochlorination was estimated, by GEM. To estimate the carbochlorination in the different beds, three separate calculations were performed. The reaction was assumed to be isothermal at 700 °C and isobar at 1 bar. Figure 3.6 gives an overview of how the equilibrium composition of the carbochlorination of bauxite was calculated. Based on the equilibrium composition estimates, the equilibrium conversion of each element into a chloride was calculated.

The equilibrium composition calculations of all three beds were started by introducing 1.5 g of bauxite in the solid phase. The bauxite was assumed to have a composition equal to that of the calcined bauxite investigated in this work. For simplicity, only the major elements present in bauxite were included. This meant all phases containing Al, Si, Ti and/or Fe. The equilibrium composition of the solid phase at 700 °C was then calculated as step 1. This was to estimate the phases present after heating to 700 °C, before carbochlorination has started.

Step 2 to *n* of the equilibrium composition calculations included the introduction of CO and $Cl_2$ in the gas phase of the top bed. To introduce a time axis to the calculations, the

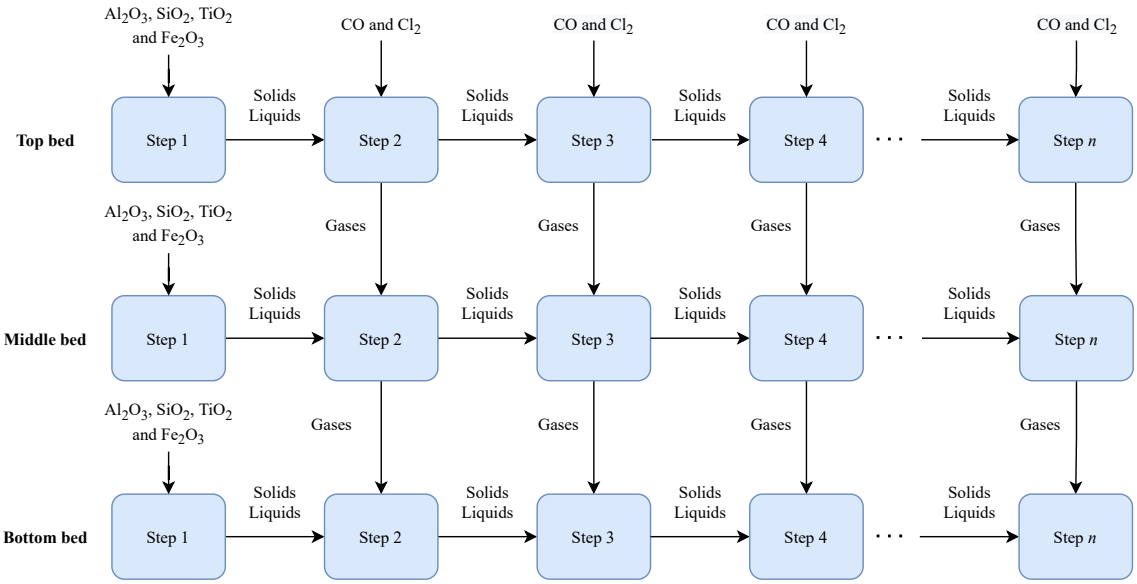


**Figure 3.6:** Overview of the thermochemical calculations, estimating the equilibrium compositions during carbochlorination of bauxite in the three reactor beds.

equivalent amount of CO and $Cl_2$ which would enter the real reactor in 30 s, was introduced in the gas phase in the calculations at every step. At each step, corresponding to 30 s of carbochlorination, the equilibrium composition was calculated. The resulting equilibrium gas phase was completely removed at each stage, before the introduction of new CO and $Cl_2$ in the next step. For the middle and bottom bed, the gas phase produced in the same step in the bed above was used as input. This was done to replicate the downstream flow of the gas phase in the real reactor.

As $Al_2O_3$ typically exist as a metastable transition alumina after calcination at 750 °C, only the $\gamma$-form of $Al_2O_3$ was assumed, and the thermodynamically stable $\alpha$-$Al_2O_3$, was deliberately excluded from the calculations, as this would typically not be formed below 1000 °C. A calculation was anyway performed including $\alpha$-$Al_2O_3$, without much change to the thermodynamically estimated equilibrium compositions.

### 3.4.2 Equilibrium Conversion During Oxolysis

The equilibrium conversion of the produced metal chlorides during oxolysis was calculated to investigate the thermodynamical feasibility of oxolysis as a process to recover $Cl_2$ from the carbochlorination of the other species than $Al_2O_3$ in bauxite. To calculate the equilibrium conversion, the equilibrium composition of the species included in the oxolysis was calculated at different temperatures. One mole of the metal chloride was entered into the system at the different temperatures, with the stoichiometric amount of $O_2$ to oxolyse the metal chloride. The conversion was calculated based on the amount of produced metal oxides.

# Chapter 4

# Results

## 4.1 Chemical Composition of Calcined Bauxite

The chemical composition of calcined bauxite, measured by XRF is given in Table 4.1. It contained traces of Mg, P-, S-, Cl-, K-, Ca-, Cr-, Mn and Sr-compounds. The calculated loss on ignition (LOI) was calculated as 27.8 wt%.

**Table 4.1:** Chemical composition of bauxite after calcination, measured by XRF.

| Chemical composition [wt%] | | | | |
|---|---|---|---|---|
| $Al_2O_3$ | $SiO_2$ | $TiO_2$ | $Fe_2O_3$ | Other |
| 62.7 | 14.0 | 2.44 | 20.3 | 1.79 |

## 4.2 Conversion

The different conversions were calculated as described in Appendix D. All the thermodynamical calculations were performed as described in Section 3.4.1 using HSC Chemistry[44].

### 4.2.1 Overall Bauxite Conversion

Figure 4.1 displays the total conversion of bauxite in all three reactor beds, measured by mass loss and by $Cl_2$ absorbed in the NaOH-scrubber. The thermodynamically calculated bauxite conversion is also displayed for the sake of comparison. Both measurements of bauxite conversion give approximately the same conversion line. An exception lies in the measurement at 15 min, where the bauxite conversion based on mass loss is higher than both the conversion based on $Cl_2$ absorption and the thermodynamically estimated conversion. As the carbochlorination proceeds, both the measured bauxite conversions deviate increasingly more from the thermodynamically estimated conversion.

### 4.2.2 Bauxite Conversion in the Three Reactor Beds

Figure 4.2 displays the measured conversion of bauxite in each reactor bed during carbochlorination, with the thermodynamically calculated conversions. Thermodynamically, it is predicted that the top bed will be fully removed, before the complete removal of the middle and then the bottom bed. The stagnant conversion of the middle and bottom bed at 10-60 min is a result of the chlorination agent at these stages being the metal chlorides

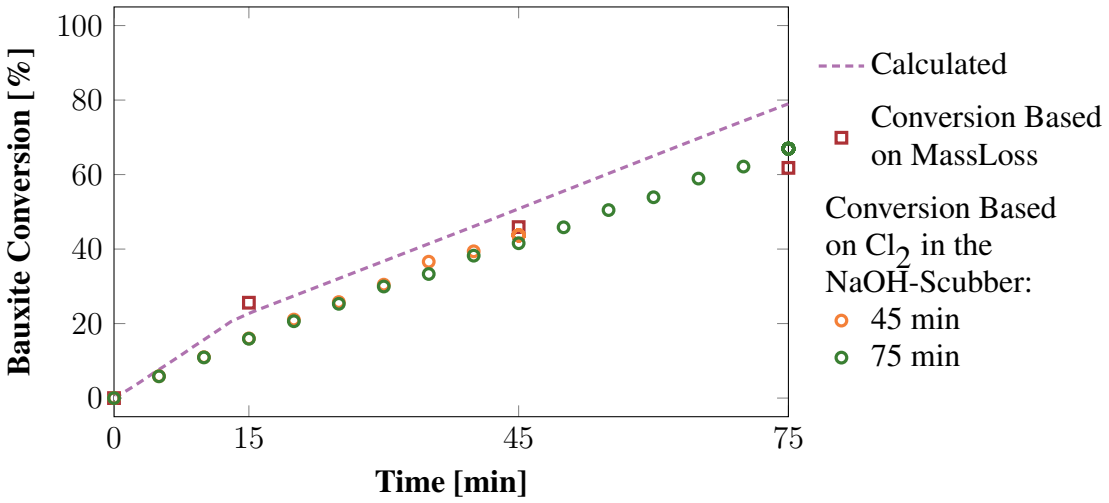


**Figure 4.1:** Measured and thermodynamically calculated bauxite conversion during carbochlorination.

produced in the beds above, which is elaborated further in Section 4.4. As these metal chlorides chlorinate the bauxite in the bed below, they are themselves deposited as a solid material in the bed, "equalising" the mass loss.

The measured conversion of bauxite was calculated based on the mass loss of each of the reactor beds. At 15 min the measured and calculated conversions agree. However, as time proceeds, the measured conversion does not follow the sequential removal of each bed as predicted thermodynamically. At 45 and 75 min, the middle and bottom beds experience conversion to some extent, without the top bed being fully converted. Nonetheless, the thermodynamically calculated conversion still agrees somewhat with the measured conversion. At 45 min, the calculated and measured conversion in the middle bed is similar. The same is the case at 75 min for the bottom bed.

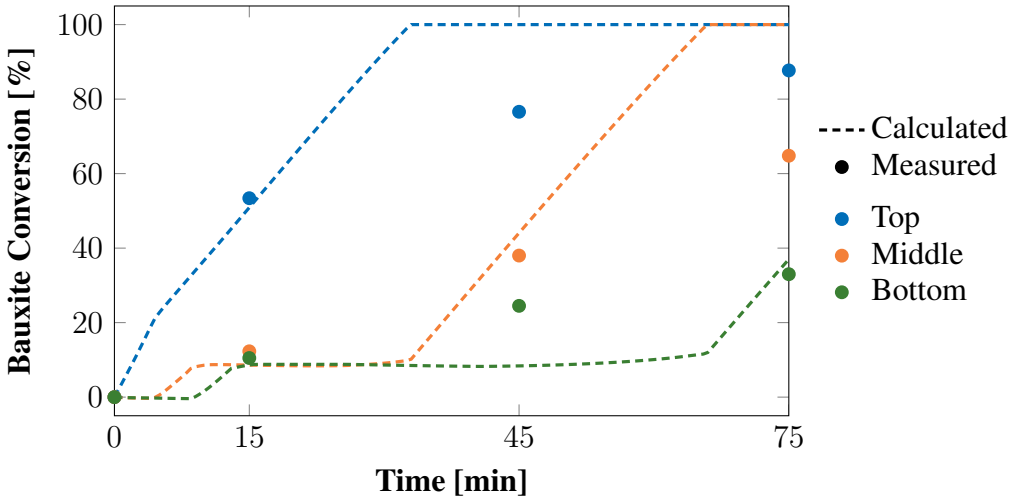


**Figure 4.2:** Measured and thermodynamically calculated conversion of bauxite in each of the reactor beds. The measured conversion was based on the mass loss.

### 4.2.3 $Cl_2$ Conversion

Figure 4.3 displays the measured conversion of $Cl_2$ during carbochlorination, based on the amount of $Cl_2$ absorbed in the NaOH-scrubber. As the carbochlorination proceeds, the $Cl_2$ conversion decreases, even though there is more bauxite left to be reacted in all three reactor beds.

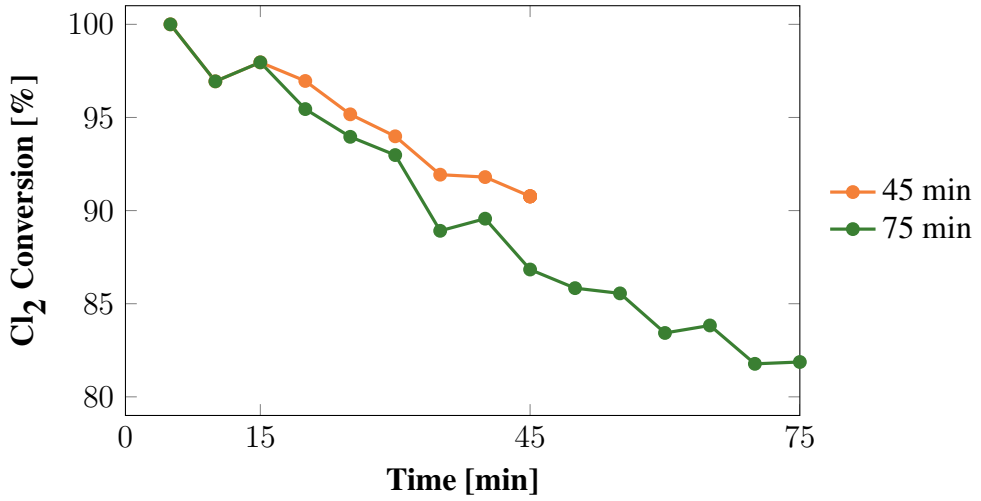


**Figure 4.3:** Measured $Cl_2$ conversion during carbochlorination. The conversion is calculated based on the amount of $Cl_2$ absorbed in the NaOH-scrubber.

## 4.3 Changes in Powder Bed Height

Figure 4.4 displays the measured reduction in powder bed height in the three reactor beds as a function of bauxite conversion. Appendix E describes how the bed height reduction was calculated. The reactor beds typically had a powder bed height of 12-13 mm each before the carbochlorination was started. A rapid reduction in bed height can be seen for the first 15% of bauxite conversion. After this, the bed height reduction stabilises around a reduction of 50%.

## 4.4 Element Removed

The elemental removal of the carbochlorinated bauxites was measured to investigate how the different constituents of bauxite reacted compared to each other. Elemental removal is here defined as

$$X_A = \frac{(\text{wt\% } A_{\text{calcined bauxite}} \cdot m_{\text{bed},\,i}) - (\text{wt\% } i_{\text{carbochlorinated bauxite}} \cdot m_{\text{bed},\,f})}{\text{wt\% } A_{\text{calcined bauxite}} \cdot m_{\text{bed},\,A}} \tag{4.1}$$

where wt% $A_{\text{calcined bauxite}}$ is the wt% of element $A$ in calcined bauxite, $m_{\text{bed},\,i}$ is the initial mass of the bed, before carbochlorination, wt% $A_{\text{carbochlorinated bauxite}}$ is the wt% of $A$ in the carbochlorinated bauxite and $m_{\text{bed},\,f}$ is the final mass of the bed, after carbochlorination.

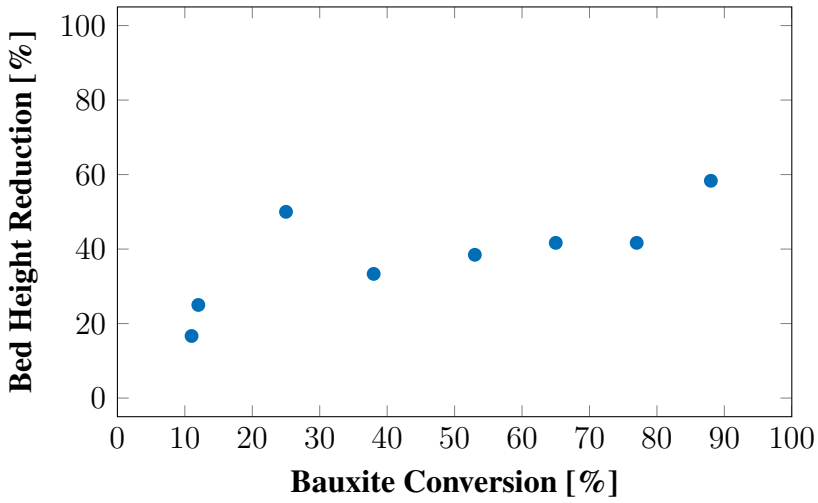


**Figure 4.4:** Powder bed height reduction as a function of the measured bauxite conversion in the three beds.

Since for instance Al can be present in different forms such as $Al_2O_3$ or $Al_2SiO_5$, the removal was calculated on element basis instead of oxide basis. The calculations were based on the XRF analyses. Figures 4.5-4.7 displays the elemental removal of the carbochlorinated bauxite in the top, middle and bottom bed. The thermodynamically estimated elemental removals, calculated as described in Section 3.4.1, are also displayed in the figures for comparison. Thermodynamically, the carbochlorination was found to produce the gaseous metal chlorides indicated in Reactions 2.1-2.5. It is important to note that thermodynamics does not take into account the kinetics of the reactions. Therefore, the thermodynamically calculated conversions only accounts for the case where equilibrium is reached instantaneously.

### 4.4.1 Top

From the thermodynamical calculations in Figure 4.5, it is evident that all the CO and $Cl_2$ entered into the reactor, reacts to produce metal chlorides. All Fe is reacted first, before all Ti is removed. Al is preferably removed before Si, however, Al is not completely removed before the Si removal starts, as for Fe and Ti. In other words, thermodynamically Fe and Ti can be completely removed without removing other species, while Al cannot be completely removed without removing some Si. Overall, the preferred reaction sequence is Fe, Ti, Al and Si.

When comparing the thermodynamic estimates to the experimentally observed values, the reaction sequence is not the same. As for the thermodynamically calculated values, Fe is preferably removed first, being almost 90% removed after carbochlorination for 15 min. The removal of Fe is relatively unchanged after this. Si and Ti seems to be the next species to be removed. Almost equal amounts of Si and Ti are removed after 15 min. However, after 45 min the Ti removal reaches a value of almost 90%, while the Si removal is below 80%. The Ti removal is stable after 45 min, whereas the Si removal increases to more than 90%. Al is experimentally observed to be the last element to be removed. However, it reaches

almost the same removal as the other species of ∼90% after 75 min of carbochlorination.

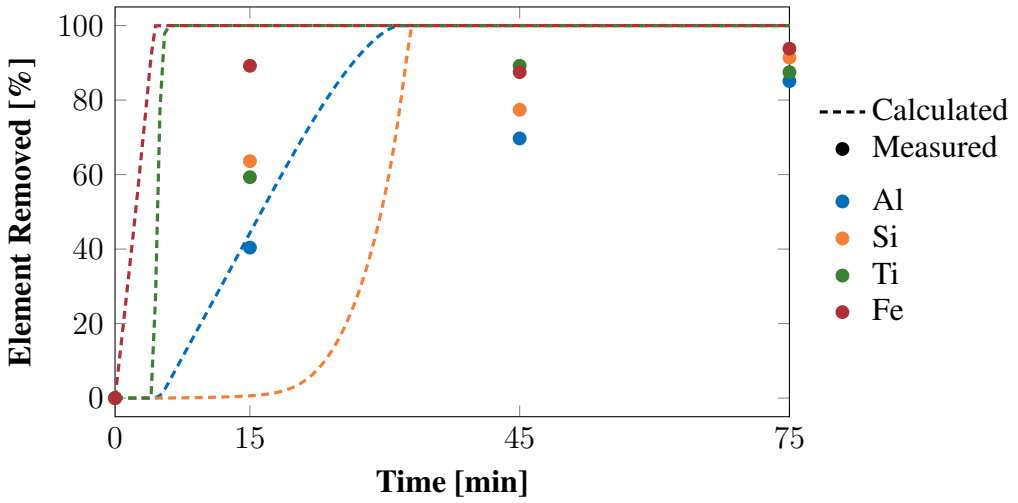


**Figure 4.5:** Thermodynamically calculated and measured elemental removal in of the major constituent of bauxite during carbochlorination of the top bed. The measured elemental removals were calculated based on XRF analyses.

### 4.4.2 Middle

The thermodynamically calculated elemental removal in the middle bed in Figure 4.6, is affected by the gas phase produced at each step in the top bed. As $Cl_2$ is completely reacted in the top bed and Fe is the first element to be removed in the this bed, $FeCl_3$ and $FeCl_2$ are the gases present in the first steps. $FeCl_3$ and $FeCl_2$ cannot chlorinate any of the solid material in the middle bed, thus nothing is removed at these stages. As Ti is reacted in the top bed, $TiCl_4$ enters the middle bed and chlorinates Fe. All the $TiCl_4$ produced in the top bed is used to chlorinate Fe, resulting in an elemental removal of -100% for Ti. A negative elemental removal means that the element is being deposited in the bed. Ti in the middle bed is first reacted as $AlCl_3$ enters the bed, resulting in a negative elemental conversion of Al. As $SiCl_4$ from the top bed enters the middle bed, Al in the middle bed is removed. Lastly, Si is removed as excess CO and $Cl_2$ from the top bed enters the middle bed.

The experimentally measured elemental removals in the middle bed follows somewhat the same trends as in the top bed. Fe is preferentially removed first, followed by Si, Ti and Al. In contrast to the top bed where the carbochlorination of Ti is slightly preferred over Si, the carbochlorination of Si is slightly preferred over Ti in the middle bed. Al has a negative removal after 15 min, similar to that which is thermodynamically estimated.

### 4.4.3 Bottom

The thermodynamically calculated elemental removals in the bottom bed in Figure 4.7 follow the same general patterns as observer for the middle bed. Fe is chlorinated by $TiCl_4$, Ti is chlorinated by $AlCl_3$, Al is chlorinated by $SiCl_4$ and Si is carbochlorinated by excess CO and $Cl_2$ from the top and middle bed. As produced $TiCl_4$ from the top and middle bed

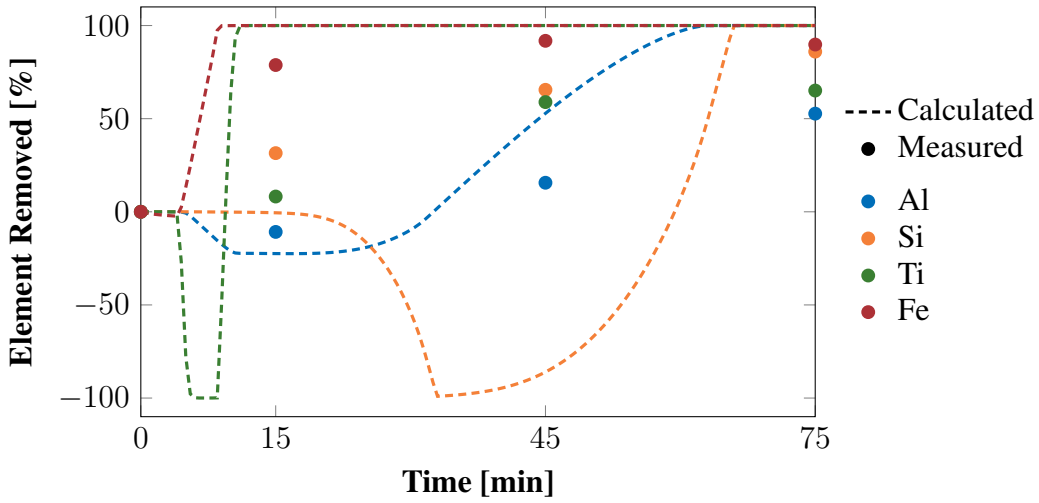


**Figure 4.6:** Thermodynamically calculated and measured elemental removal in of the major constituent of bauxite during carbochlorination of the middle bed. The measured elemental removals were calculated based on XRF analyses.

is used to carbochlorinate Fe, an elemental removal of -200% is reached for Ti. The same is the case for Si.

The measured elemental removals in the bottom bed follow the same general reaction sequence as seen in the middle bed. However, at 15 min, Fe is the only element to be removed, being 75% removed, while the elemental removal of Al, Si and Ti is slightly negative. At 45 and 75 min Si and Ti are being removed, with the removal of Si being preferred over the removal of Ti. Al is observed to not be removed by carbochlorination in the bottom bed, as it reaches a maximum removal of only 2.5% after 45 min.

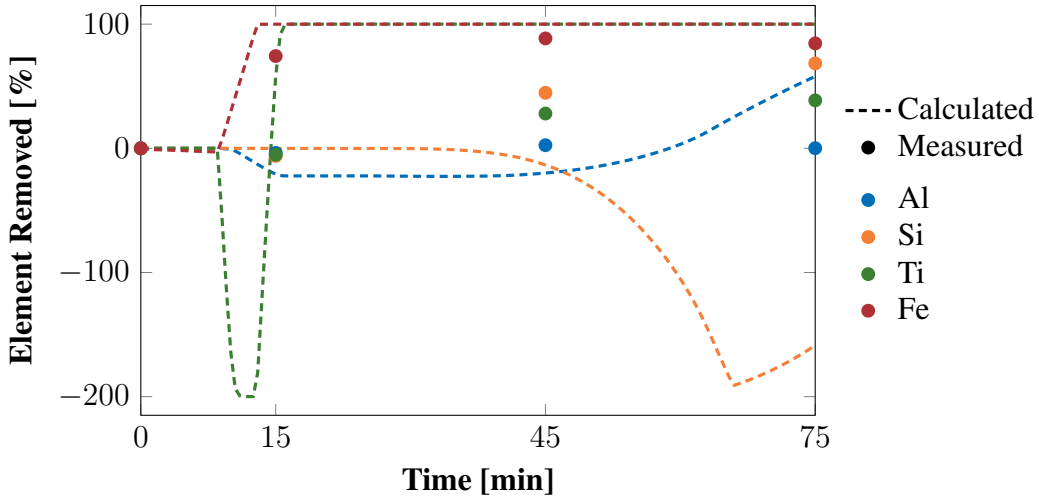


**Figure 4.7:** Thermodynamically calculated and measured elemental removal in of the major constituent of bauxite during carbochlorination of the bottom bed. The measured elemental removals were calculated based on XRF analyses.

## 4.5 Chemical Composition

The chemical composition of calcined bauxite and all samples of carbochlorinated bauxite were measured by XRF to investigate how the chemical composition changed when calcined bauxite were subjected to carbochlorination. Figures 4.8-4.10 display the composition changes in the top, middle and bottom bed, respectively, as a function of carbochlorination time. The time $t = 0$, corresponds to the composition of the calcined bauxite. As only the major constituents of bauxite, $Al_2O_3$, $SiO_2$, $TiO_2$ and $Fe_2O_3$, are included, the composition does not fully add up to 100%. The full results from the XRF analyses can be found in Appendix F.

It is important to note that the different carbochlorinated bauxite samples do not have the same mass. Thus, when the wt% of one oxide increases over the course of the carbochlorination, it does not mean that the physical amount of this oxide increases. For instance, the carbochlorinated bauxite in the top bed contains 4.68 wt% $Fe_2O_3$ after 15 min, and 10.2 wt% $Fe_2O_3$ after 75 min. As the masses of the two samples were 0.739 g and 0.180 g, respectively, the amount of $Fe_2O_3$ in the top bed is 34.6 mg after 15 min and 18.3 mg after 75 min. This means that the amount of $Fe_2O_3$ in the top bed decreased from 15 to 75 min, even though the wt% increased over the same range.

The XRF measures the amount of each element assuming that it is an oxide. As $Cl_2$ is introduced in the carbochlorination, any produced metal chlorides which do not leave the reactor will be measured in the XRF assuming it is an oxide. This results in small errors in the measured chemical compositions. Since the metal chlorides produced by carbochlorination of $Al_2O_3$, $SiO_2$, $TiO_2$ and $Fe_2O_3$ typically form gaseous metal chlorides, as seen in Table 2.2, it is assumed that these species exist as oxides in all the bauxite samples.

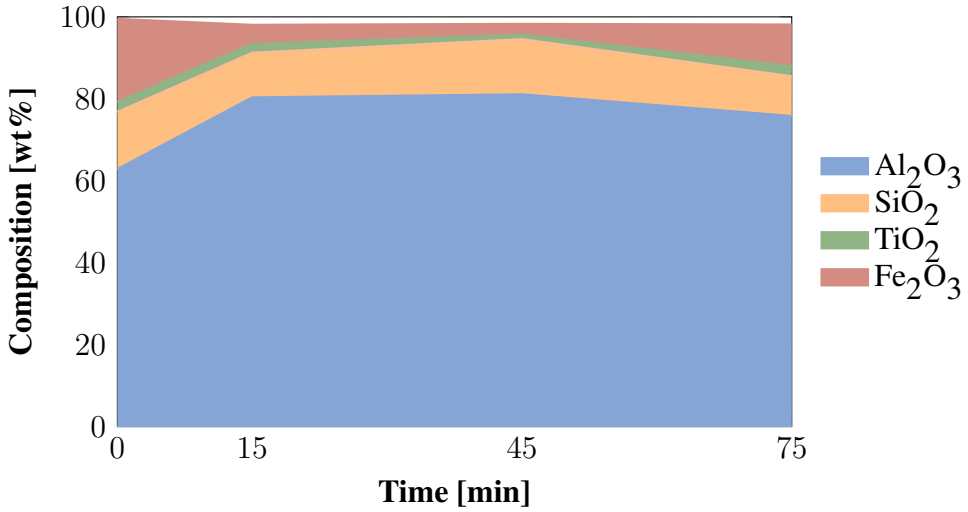


**Figure 4.8:** Composition changes in the top bed, measured by XRF.

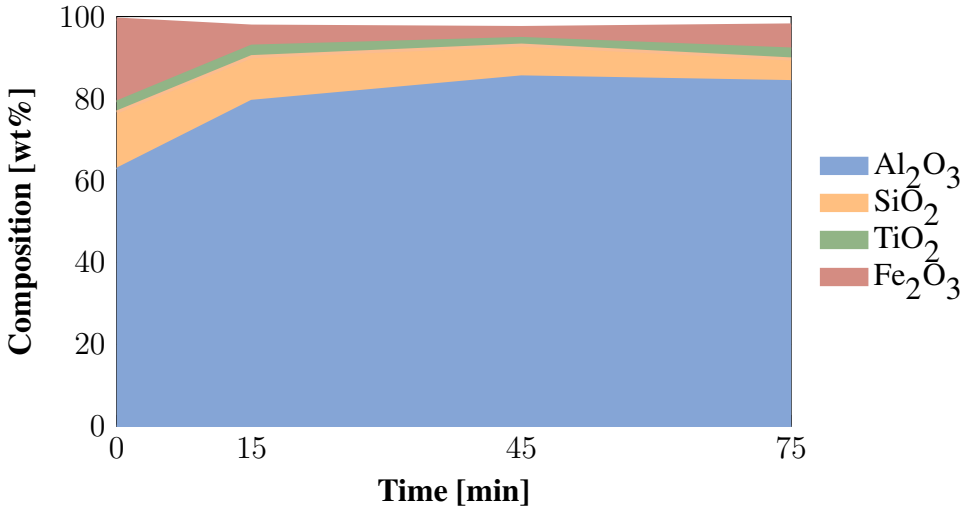


**Figure 4.9:** Composition changes in the middle bed, measured by XRF.

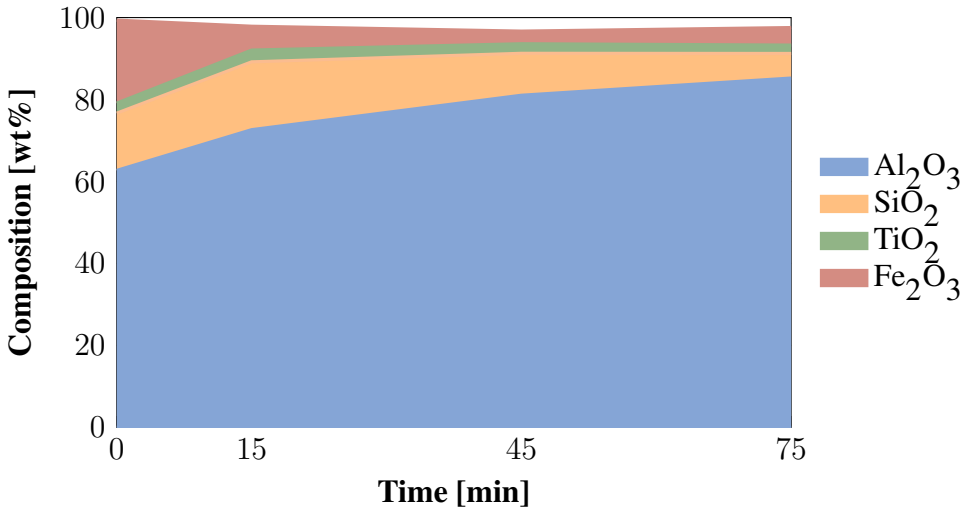


**Figure 4.10:** Composition changes in the bottom bed, measured by XRF.

The wt% development of $Al_2O_3$ and $SiO_2$ is different for the top bed, compared to the middle and bottom bed. In the top bed the wt% of $Al_2O_3$ increases from 0 to 15 min. Little change can be observed from 15 to 45 min. From 45 min to 75 min the wt% of $Al_2O_3$ decreases. For the middle and bottom bed however, the wt% of $Al_2O_3$ increases throughout the course of the carbochlorination. The wt% of $SiO_2$ in the top bed is fairly constant from 0 to 15 min. It increases from 15 to 45 min, and decreases again from 45 to 75 min. For the middle and the bottom bed however, the wt% of $SiO_2$ decreases throughout the course of the carbochlorination.

The calcined bauxite contains ~20 wt% $Fe_2O_3$. This wt% rapidly decreases in all the reactor beds during the first 15 min of carbochlorination. For the top bed, the wt% of $Fe_2O_3$ increases again from 45 to 75 min. The same can be observed in the middle and bottom bed,

however, the increases are smaller. The wt% of $TiO_2$ stays fairly constant throughout the carbochlorination in all three reactor beds.

Figure 4.11 displays the total composition changes, if all the beds was regarded as one bed. $Al_2O_3$ is the only compound which increases in wt% throughout the entire carbochlorination. The wt% of $SiO_2$ stays fairly constant the first 15 min of carbochlorination, before it decreases during the remainder of the carbochlorination. As explained for the top, middle and bottom bed, the wt% of $Fe_2O_3$ rapidly decreases during the first 15 min of carbochlorination. From 45 to 75 min, the wt% of $Fe_2O_3$ increases.

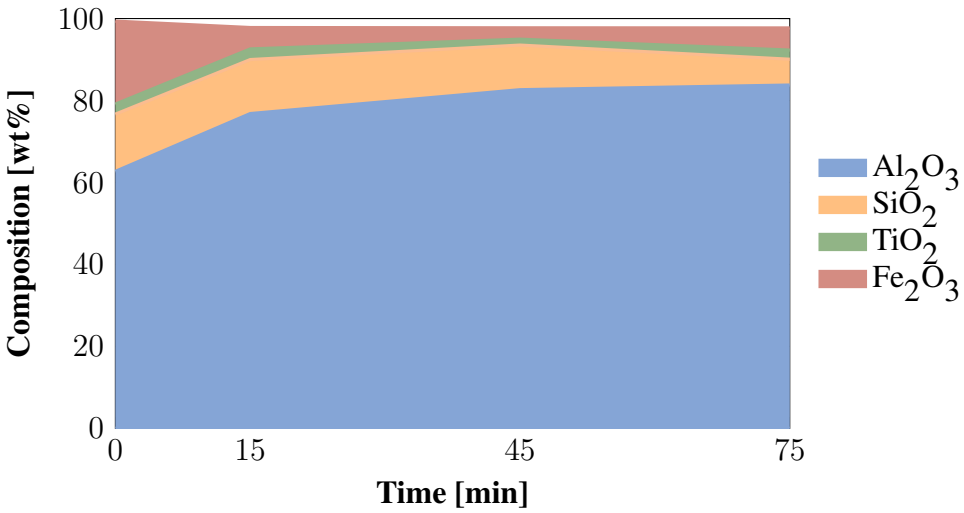


**Figure 4.11:** Composition changes in all the beds, measured by XRF.

## 4.6 Phase Identification

XRD measurements were performed on the milled bauxite powder, calcined bauxite and all samples of carbochlorinated bauxite, to investigate their respective phases. Of special interest was how the phase composition of calcined bauxite was affected by carbochlorination. As the transition aluminas present in heat-treated bauxite are heavily dependent on their hydrate precursor, an XRD diffractogram of the milled bauxite powder was also obtained. Phase identification was performed with Bruker DIFFRAC.EVA[72]. Due to a small offset in the goniometer, the diffractometer measures a slight offset in the peak positions.

### 4.6.1 Milled Bauxite Powder

Figure 4.12 displays the diffractogram of the milled bauxite powder. The phases identified were gibbsite, nacrite ($Al_2Si_2O_5(OH)_4$), anatase ($TiO_2$) and hematite ($Fe_2O_3$)[73–76]. Nacrite is a polymorph of the more known clay mineral kaolinite[74].

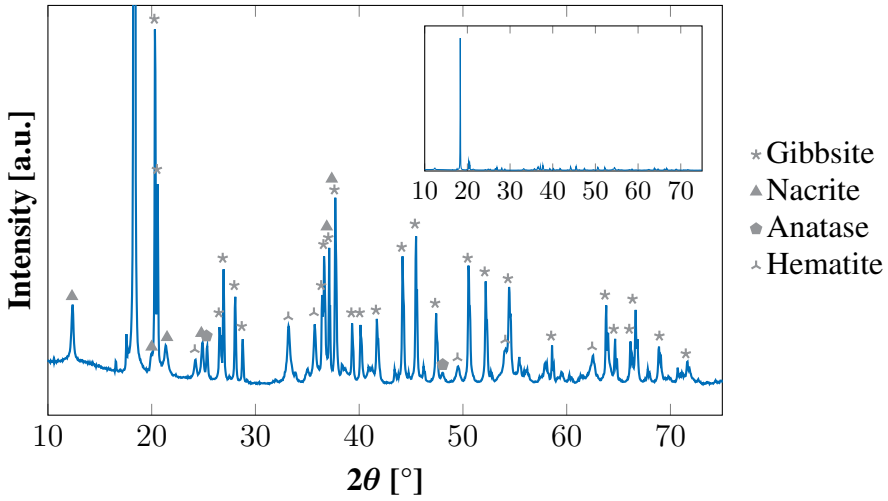


**Figure 4.12:** XRD diffractogram of milled bauxite powder with indexed peaks[73–76]. For simplicity, only the indices of the major peaks are displayed. The top right figure is added to display the intensity of the gibbsite peak at 18° relative to the other peaks.

### 4.6.2 Calcined Bauxite

Figure 4.12 displays the diffractogram of the calcined bauxite. The phases identified were $\gamma$-$Al_2O_3$, $\gamma$-$Al_{2.67}O_4$, $\chi$-$Al_2O_3$, quartz ($SiO_2$), anatase, rutile and hematite. All of the $Al_2O_3$ peaks are broadened, due to the distorted structure of these transition aluminas. $\alpha$-$Al_2O_3$ could neither be confirmed nor disproved as a constituent of the calcined bauxite, as the peaks associated with $\alpha$-$Al_2O_3$ coincide with the peaks of the other transition aluminas and hematite[77]. Only small peaks of quartz and rutile could be observed.

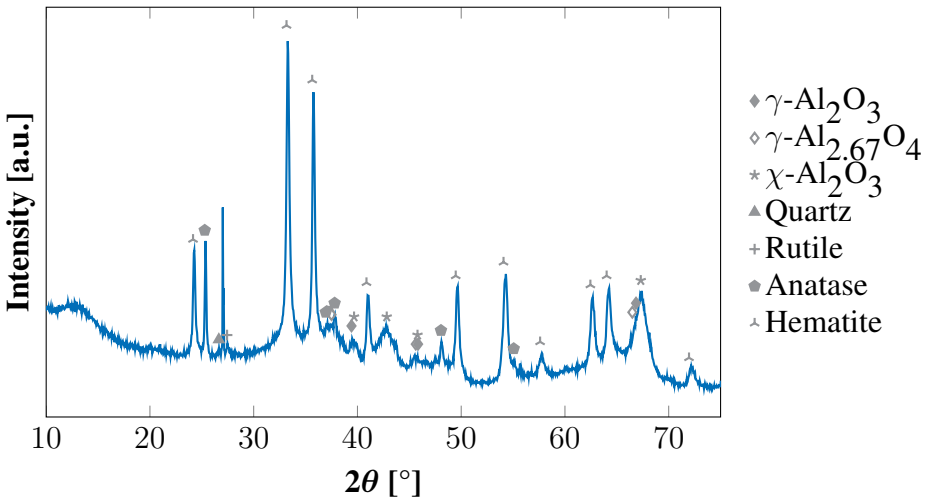


**Figure 4.13:** XRD diffractogram of calcined bauxite with indexed peaks[75, 76, 78–82]. For simplicity, only the indices of the major peaks are displayed.

The phase resulting in the peak at 27° could not be identified. Several different phases were found which could have resulted in the observed peak. However, a positive identification of

any one of these phases could not be made, as the other peaks associated with these phases could fit below the several broadened peaks in the diffractogram. For instance, pretulite ($ScPO_4$) could have resulted in the 27° peak, as the rest of the peaks associated with this phase would hide behind the hematite and $Al_2O_3$ peaks[83]. However, it is not known to be present in significant amounts in the bauxite investigated in this work, as it was not identified by XRF.

### 4.6.3 Carbochlorinated Bauxite

Figures 4.14-4.16 display the diffractograms of the carbochlorinated bauxite samples. The intensity scaling in the diffractograms in all the figures are equal for comparison purposes.

#### Top

Figure 4.14 displays the diffractogram of the carbochlorinated bauxites form the top bed. $\alpha$-$Al_2O_3$, $\gamma$-$Al_2O_3$, $\gamma$-$Al_{2.67}O_4$, quarz and hematite can be observed at all three carbochlorination lengths. $\chi$-$Al_2O_3$ can be detected in the 15 min diffractogram. It is possible that this phase is present in the 45 and 75 min diffractogram also, as several of its peaks coincide with the $\gamma$-$Al_2O_3$ and $\gamma$-$Al_{2.67}O_4$ peaks. Mullite ($3\,Al_2O_3 \cdot 2\,SiO_2$) is observed in the 15 and 45 min diffractograms. These peaks display an increased intensity from 15 to 45 min. The $\alpha$-$Al_2O_3$ and hematite peak also display a change in intensity during the course of the carbochlorination as an increase in the intensities of the peaks of these phases can be observed from 45 min to 75 min.

The quartz peak at 21° in the 75 min experiment has an abnormally high intensity, compared to the other peaks associated with this phase. This peak is therefore likely caused by another phase, however no positive identification of this phase could be made.

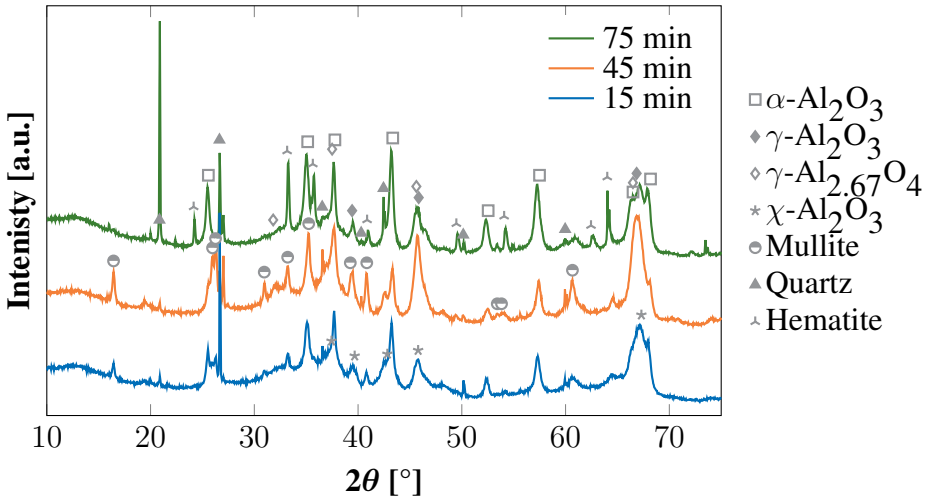


**Figure 4.14:** XRD diffractograms of carbochlorinated bauxite from the top bed, with indexed peaks[76–81, 84, 85]. For simplicity, only the indices of the major peaks are displayed.

### Middle

Figure 4.15 displays the diffractograms of the carbochlorinated bauxites from the middle bed. $\alpha$-$Al_2O_3$, $\gamma$-$Al_2O_3$, $\gamma$-$Al_{2.67}O_4$, $\chi$-$Al_2O_3$, hematite and quartz can be observed at all carbochlorination lengths. Mullite is observed only in the 45 min diffractogram, and minor peaks of $FeCl_2 \cdot 2\,H_2O$ can be observed in the 75 min diffractogram. The intensities of the hematite peaks are smaller in the 15 and 45 min diffractograms, compared to the 75 min diffractogram.

It is visible that there is a decrease in crystallinity from the top to the middle bed, due to the decrease in sharp peaks between these diffractograms. The intensities of the crystalline phases $\alpha$-$Al_2O_3$ and hematite, which yielded sharp peaks in the top bed, is decreased in the middle bed. Only quartz yield sharp peaks in the middle bed. The broad peaks of the $\gamma$-$Al_2O_3$, $\gamma$-$Al_{2.67}O_4$ and $\chi$-$Al_2O_3$ dominate more in the middle bed, compared to the top bed.

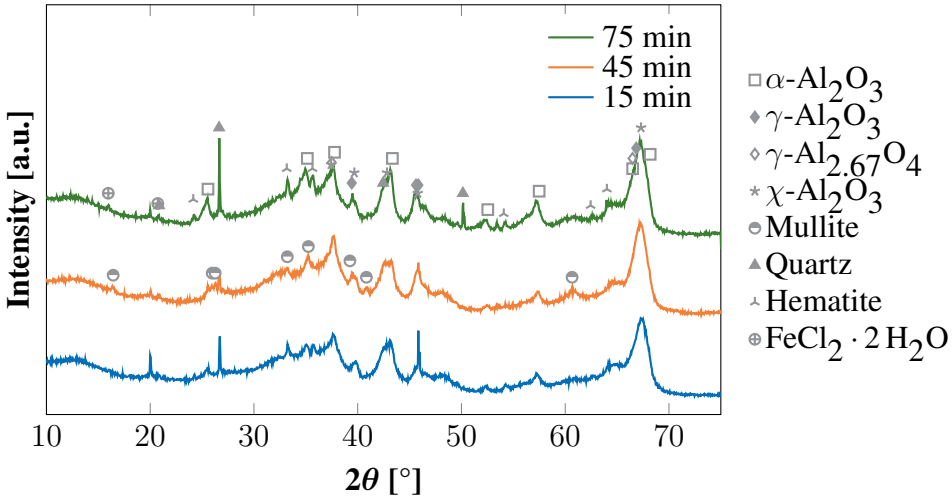


**Figure 4.15:** XRD diffractograms of carbochlorinated bauxite from the middle bed, with indexed peaks[76–81, 84–86]. For simplicity, only the indices of the major peaks are displayed.

### Bottom

Figure 4.16 displays the XRD diffractograms of the carbochlorinated bauxites from the bottom bed. As for the middle bed, a significant decrease in crystallinity can be observed, compared to the top bed. This can be seen by the several broad peaks and lack of sharp peaks in the diffractograms. The decrease in crystallinity from the top to the bottom bed is more severe compared to the decrease from the top to the middle bed. Because of the low crystallinity of the bottom bed, it is difficult to properly characterise the phases present in these samples. For instance, the major peaks of $\alpha$-$Al_2O_3$ and hematite almost disappear in the broad peak at 30-40°. These two phases appear in all three diffractograms, along with $\gamma$-$Al_2O_3$, $\gamma$-$Al_{2.67}O_4$, $\chi$-$Al_2O_3$ and quartz. Minor peaks of $FeCl_2 \cdot 2\,H_2O$ can also be observed in the 75 min diffractogram. The sharp peaks at 27° and 55° in the 15 min diffractogram could not be identified.

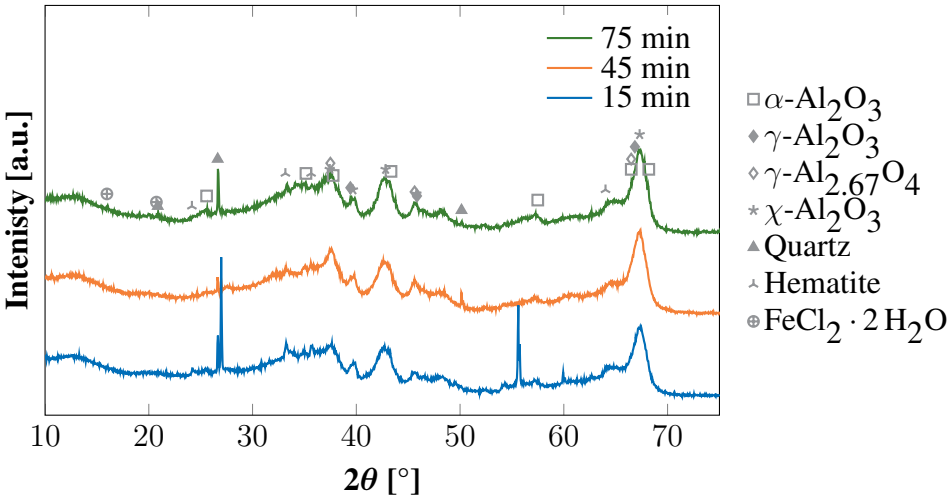


**Figure 4.17:** XRD diffractograms of carbochlorinated bauxite from the bottom bed, with indexed peaks[76–81, 86]. For simplicity, only the indices of the major peaks are displayed.

## 4.7 BET Surface Area

The BET surface areas of the milled bauxite powder, calcined bauxite and all samples of carbochlorinated bauxite were measured to investigate how the surface area of bauxite developed as the carbochlorination proceeded. Table 4.2 displays the measured surface area of the milled bauxite powder before and after calcination. Table 4.3 displays the surface areas of all the carbochlorinated bauxite samples.

From Table 4.2, it can be observed that the calcination of bauxite increases the surface area of bauxite by a factor of 20. When this high-surface area, calcined bauxite is subjected to carbochlorination, its surface area decreases, as displayed in Table 4.3. The decrease is most severe in the top bed, decreasing in severity going down the reactor beds. As the carbochlorination proceeds, the development of the surface area is ambiguous. For the top bed, the surface area decreases as the carbochlorination proceeds. In contrast, the surface area of both the middle and bottom bed increases from 15 to 45 min, before decreasing from 45 to 75 min.

**Table 4.2:** Measured BET surface area of the milled bauxite powder before and after calcination at 750 °C, obtained by 5-point BET analysis.

| | **BET Surface Area [$m^2g^{-1}$]** |
|---|---|
| **Milled Bauxite Powder** | $5.29 \pm 0.02$ |
| **Calcined Bauxite** | $106.0 \pm 0.5$ |

Figure 4.18 displays the BET surface area as a function of conversion. An initial rapid decrease in surface area can be seen as the conversion reaches 10%. From 10 to 25% conversion, the surface area increases, before a relatively stable decrease can be observed for conversions higher than 25%.

**Table 4.3:** Measured BET surface area of carbochlorinated bauxite, obtained by 5-point BET analysis.

| Time [min] | Bed Height | BET Surface Area [$m^2g^{-1}$] |
|---|---|---|
| 15 | Top | $53 \pm 1$ |
| | Middle | $69.0 \pm 0.2$ |
| | Bottom | $71.2 \pm 0.2$ |
| 45 | Top | $36 \pm 1$ |
| | Middle | $73.5 \pm 0.3$ |
| | Bottom | $86.9 \pm 0.6$ |
| 75 | Top | $35.5 \pm 0.2$ |
| | Middle | $54.6 \pm 0.6$ |
| | Bottom | $77.8 \pm 0.3$ |

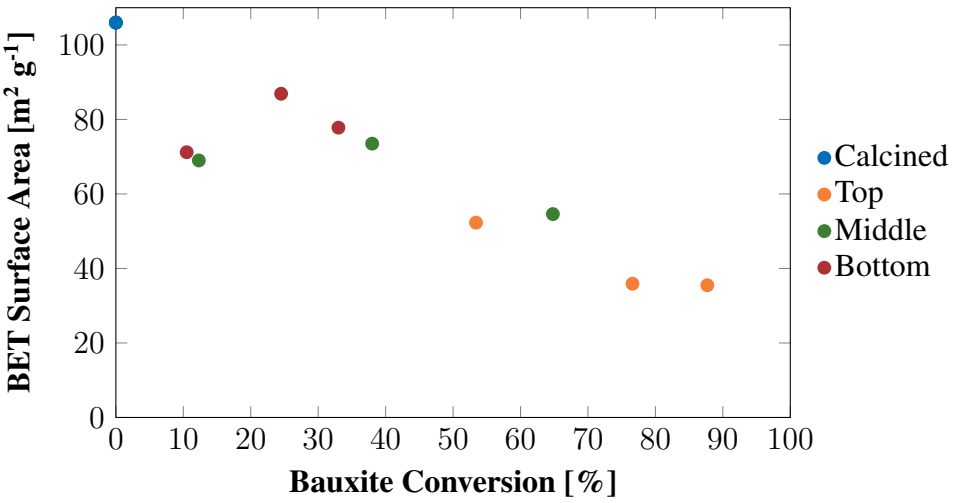


**Figure 4.18:** Measured BET surface area of carbochlorinated bauxite as a function of bauxite conversion. The BET surface area of calcined bauxite is

## 4.8 Characterisation in SEM

Investigations in SEM was performed on the milled bauxite powder, calcined bauxite and all samples of carbochlorinated bauxite to investigate how the morphology of the bauxite particles changed as they were subjected to carbochlorination. As the morphology of $Al_2O_3$ is highly dependent on its precursor, the milled bauxite powder was also investigated. Micrographs were collected by secondary electron imaging. Three different magnifications were used to investigate the sample morphology: low at 200 X, medium at 5k X and high at 15k X magnification.

### 4.8.1 Milled Bauxite Powder

Figure 4.19 displays the micrographs of the milled bauxite powder at three different magnifications. The low magnification micrograph in Figure 4.19a displays the wide particle size range and general morphology of the milled bauxite powder. It consists of larger particles around 100 µm in diameter, and several much smaller particles with a diameter of less than 1 µm. The smaller particles surround the larger particles almost like dust. In the medium and high magnification micrograph in Figures 4.19b and 4.19c, respectively, the surface of what is believed to be a gibbsite particle is displayed. The layered structure is clearly visible, and the sides of the particle are covered by dust particles.

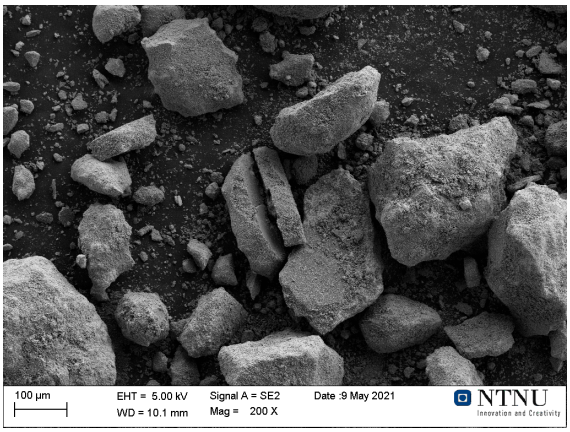


**(a)** 200 X magnification.

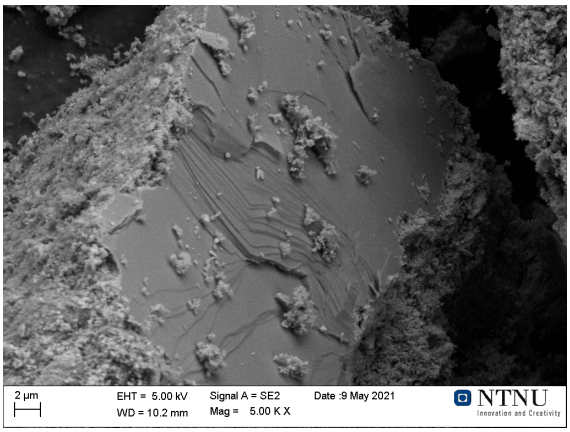


**(b)** 5k X magnification.

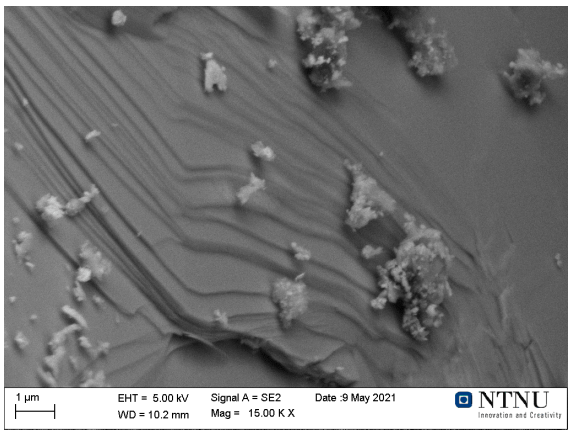


**(c)** 15k X magnification.

**Figure 4.19:** Secondary SEM micrographs of milled bauxite powder.

### 4.8.2 Calcined Bauxite

Figure 4.20 displays the micrographs of the calcined bauxite at three different magnifications. The low magnification micrograph in Figure 4.20a displays the particle size range and general morphology of the calcined bauxite particles. Compared to the milled bauxite powder, the calcined bauxite consists of a higher concentration of smaller dust particles. The larger particles also appear to be smaller than the large particles in the milled bauxite

powder. The medium magnification micrograph in Figure 4.20b displays the surface of what is believed to be an $Al_2O_3$ particle. The surface consists of several cracks, better displayed in the high magnification micrograph in Figure 4.20c. In addition to these cracks, the surface is dissimilar from the gibbsite surface in that it has an apparent higher surface coverage of dust particles on the flat surface. A circular area of a different, almost lamellar, structure can also be observed in the high magnification micrograph.

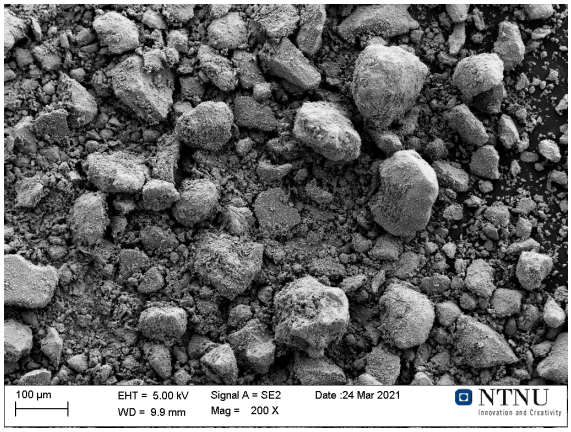


**(a)** 500 X magnification.

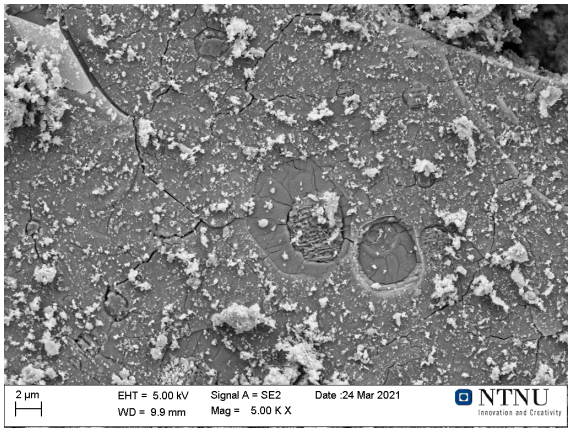


**(b)** 5k X magnification.

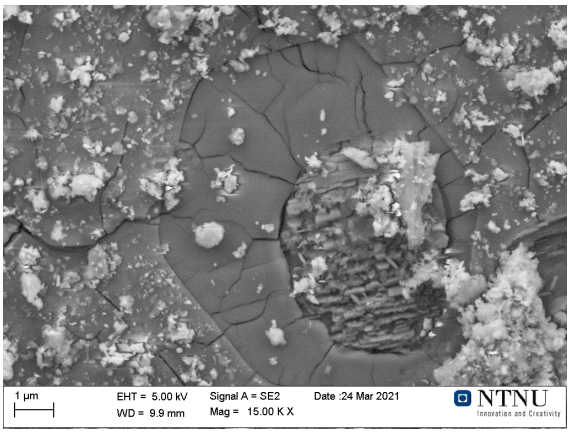


**(c)** 15k X magnification.

**Figure 4.20:** Secondary SEM micrographs of calcined bauxite.

### 4.8.3 Carbochlorinated Bauxite

The most important micrographs of the carbochlorinated bauxites are displayed in Figures 4.21-4.24. Several of the carbochlorinated bauxites displayed the same particle morphology as seen in the calcined bauxite. Therefore, the micrographs of these carbochlorinated baxuites are displayed in Appendix G.

#### Top

Figure 4.21 displays the micrographs of bauxite from the top bed after 15 min of carbochlorination at three different magnifications. The low magnification micrograph in

Figure 4.21a displays the particle size range and general morphology of the particles in this carbochlorinated bauxite sample. No major differences can be observed, compared to the calcined bauxite. The medium and high magnification in Figure 4.21b and 4.21c, respectively, displays the surface of what is believed to be an $Al_2O_3$ particle. As seen the high magnification micrograph, the $Al_2O_3$ surface contains several pores, concentrated at specific areas of the $Al_2O_3$ particle. Such areas can for instance be seen on the left and right side of the particle. In between the areas, the typical cracked surface from the calcined bauxite can be observed.

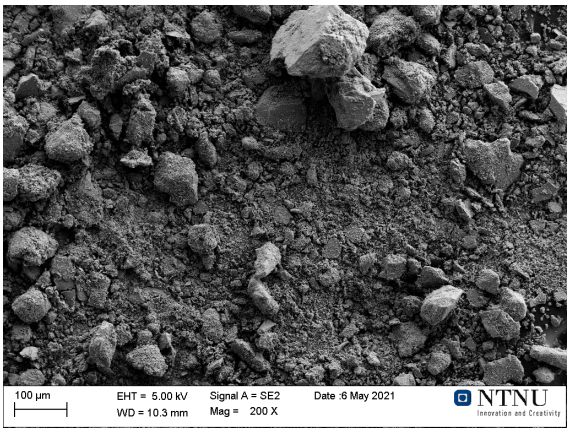


**(a)** 500 X magnification.

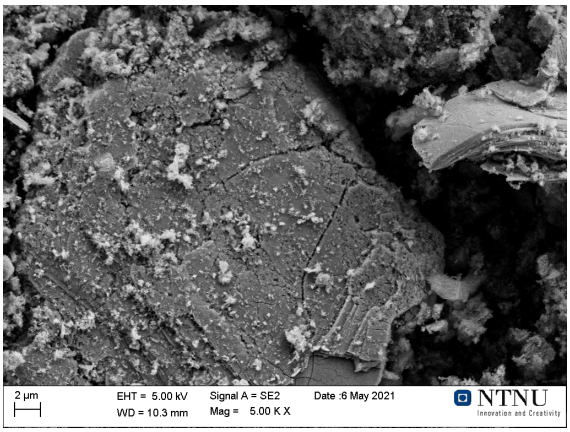


**(b)** 5k X magnification.

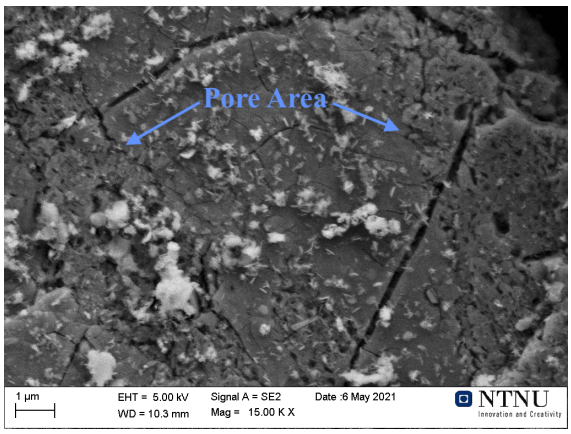


**(c)** 15k X magnification.

**Figure 4.21:** Secondary SEM micrographs of bauxite from the top bed after carbochlorination for 15 min.

Figure 4.22 displays the micrographs of bauxite from the top bed after 45 min of carbochlorination at four different magnifications. The low magnification micrograph in Figure 4.22a displays the particle size range and general morphology of the particles in this carbochlorinated bauxite sample. No major differences can be observed, compared to the calcined bauxite and the 15 min carbochlorinated bauxite from the top bed. The medium and high magnification in Figures 4.22b and 4.22c, respectively, displays the surface of the small particles in the middle of the low magnification micrograph, where a cluster of small porous particles could be found, dissimilar to the particle morphologies found in all the other

samples. The particles are relatively equal in size, with a diameter of ∼4 µm. All of the particles also have similar shapes with clearly faceted faces, similar to a hexagonal structure. A very high magnification micrograph was obtained for this structure, to get a better view of the pore structure of the particles. This micrograph is presented in Figure 4.22d.

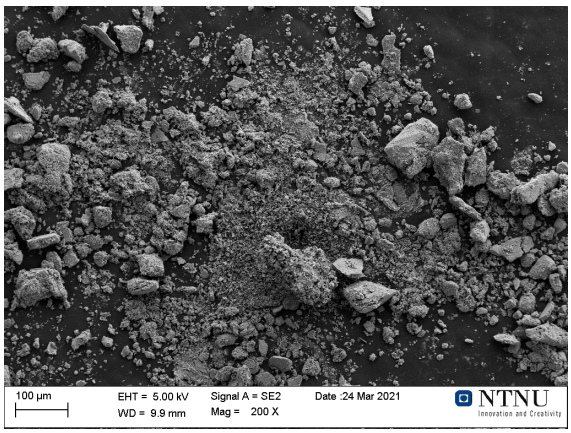


**(a)** 500 X magnification.

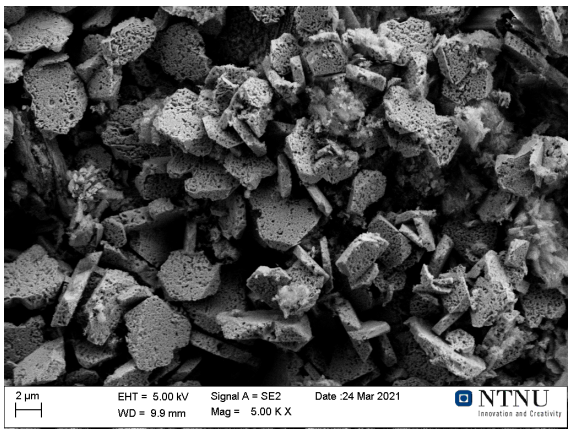


**(b)** 5k X magnification.

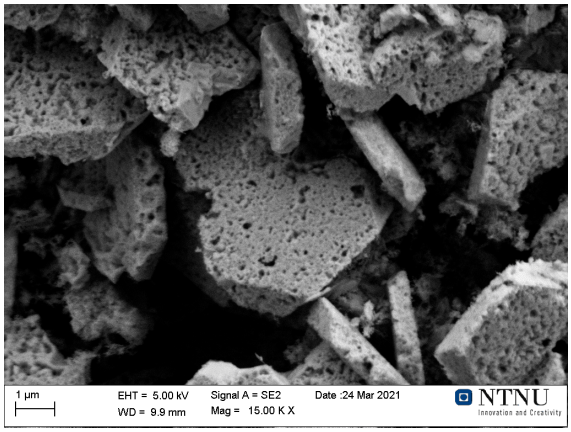


**(c)** 15k X magnification.

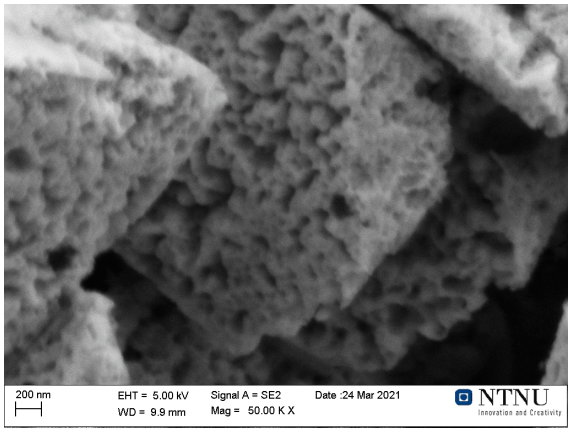


**(d)** 50k X magnification.

**Figure 4.22:** Secondary SEM micrographs of bauxite from the top bed after carbochlorination for 45 min.

Figure 4.23 displays the micrographs of bauxite from the top bed after 75 min of carbochlorination at three different magnifications. The low magnification micrograph in Figure 4.23a displays the particle size range and general morphology of the particles in this carbochlorinated bauxite sample. Compared to the calcined bauxite and other carbochlorinated bauxite samples, this sample consists almost only of small dust particles. No larger particles can be seen in the micrograph. The medium and high magnification in Figure 4.23b and 4.23c, respectively, displays the surface of what is believed to be an $Al_2O_3$ particle. This particle has a similar hexagonal shape as the particles found in the top bed after 45 min of carbochlorination, however, they do not display a porous structure. In fact, the surface of the particle is more similar to the non-porous areas of the surface of the $Al_2O_3$ particle found in the top bed after 15 min of carbochlorination.

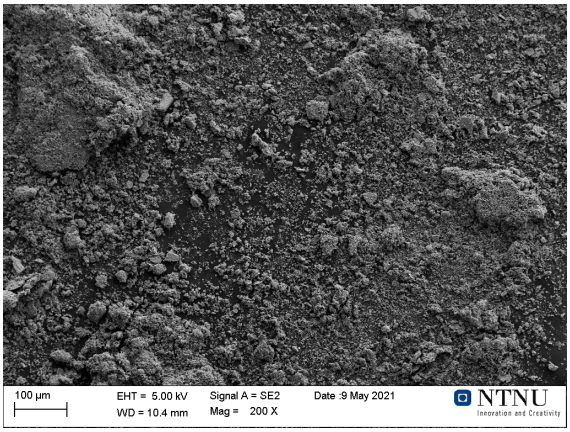


**(a)** 500 X magnification.

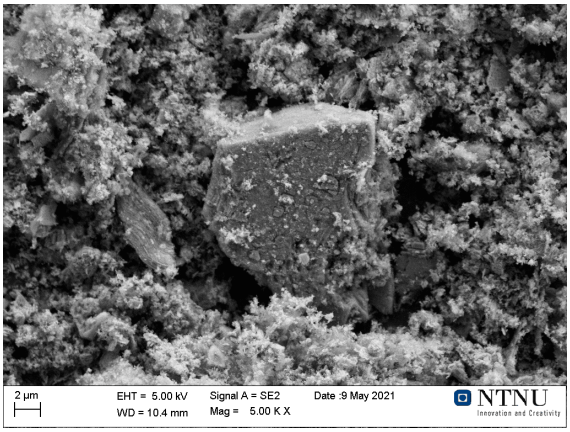


**(b)** 5k X magnification.

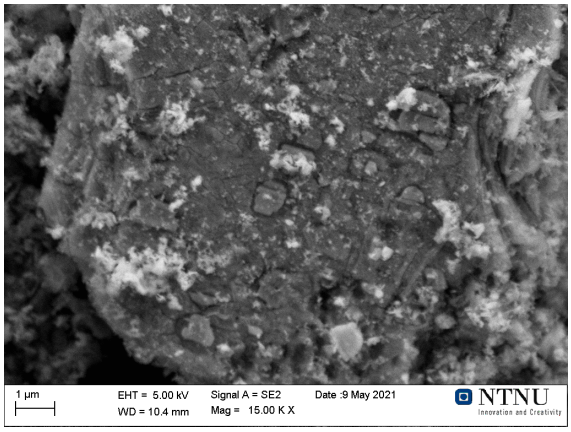


**(c)** 15k X magnification.

**Figure 4.23:** Secondary SEM micrographs of bauxite from the top bed after carbochlorination for 75 min.

### Bottom

Figure 4.24 displays the micrographs of bauxite from the bottom bed after 75 min of carbochlorination at three different magnifications. The low magnification micrograph in Figure 4.24a displays the particle size range and general morphology of the particles in this carbochlorinated bauxite sample. No major differences can be observed, compared to the calcined bauxite and the 15 and 45 min carbochlorinated bauxite from the top bed. The medium and high magnification in Figure 4.24b and 4.24c, respectively, displays the surface of what is believed to be an $Al_2O_3$ particle. A similar phenomenon to that seen in the 15 min carbochlorinated bauxite top bed can be observed in the micrographs. The particle surface is clearly divided into areas of porous and non-porous structures. Compared to the porous areas in the 15 min top bed, the pores seem more densely packed in this sample. The non-porous structure is similar to the cracked surface observed in the calcined material.

The elemental composition of the porous and non-porous structures in the micrograph in Figure 4.24b were investigated by EDS. Due to time constrains, this was the only particle analysed. Five areas of each structure were analysed, and the average elemental

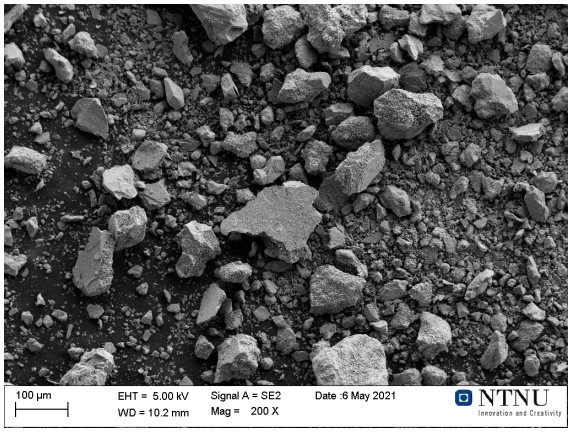


**(a)** 500 X magnification.

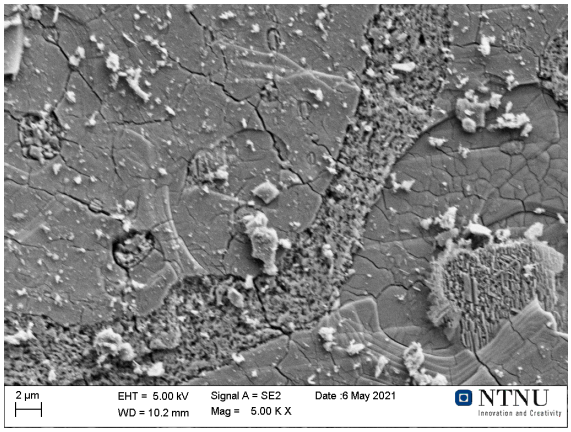


**(b)** 5k X magnification.

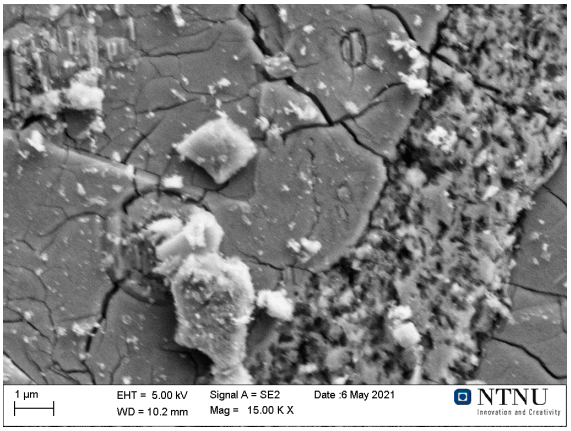


**(c)** 15k X magnification.

**Figure 4.24:** Secondary SEM micrographs of bauxite from the bottom bed after carbochlorination for 75 min.

compositions were calculated. Table 4.4 displays the elemental composition of the porous and non-porous structure. For reference, the ideal elemental composition of $Al_2O_3$ is 60 at% O and 40 at% Al. Both the porous and non-porous structure display elemental composition similar to $Al_2O_3$, thus identifying this as an $Al_2O_3$ particle. The difference between the elemental composition of the porous and non-porous structure is that the porous structure contains traces of Si and that traces of Cl can be found in the non-porous structure.

**Table 4.4:** Elemental composition of the porous and non-porous structures, measured by EDS.

| | **Elemental composition [at%]** | | | |
|---|---|---|---|---|
| | **O** | **Al** | **Si** | **Cl** |
| **Porous** | $61.0 \pm 0.5$ | $38.4 \pm 0.5$ | $0.53 \pm 0.08$ | – |
| **Non-Porous** | $61.8 \pm 0.2$ | $38.1 \pm 0.4$ | – | $0.1 \pm 0.3$ |

## 4.9 Analysis of Produced Metal Chlorides

A sample was taken out of the condenser after each of the carbochlorination experiment. The composition of Al, Si, Ti and Fe in these samples were measured by ICP-MS. The results are given in Table 4.5. The ICP-MS gave the amount of each element present in the condenser in ppm. Assuming the elements to be present as $AlCl_3$, $SiCl_4$, $TiCl_4$ and $FeCl_3$ the wt% was calculated. $AlCl_3$ and $FeCl_3$ are the only elements found in reasonable amounts in the condenser. It should be noted that high uncertainties are associated with the measured values, as the metal chlorides condensed heterogeneously in the condenser. The first metal chlorides produced were condensed on the condenser walls, and they were not easily removed after the experiment was completed. No liquids could be observed in the condenser, only a solid phase.

**Table 4.5:** Composition of the produced metal chlorides, measured by ICP-MS.

| Time [min] | Chemical composition [wt%] | | | |
|---|---|---|---|---|
| | $AlCl_3$ | $SiCl_4$ | $TiCl_4$ | $FeCl_3$ |
| 15 | 43.6 | 0.0596 | 0.142 | 56.2 |
| 45 | 31.7 | 0.0191 | 0.0523 | 68.2 |
| 75 | 56.2 | 0.0670 | 0.131 | 32.6 |

## 4.10 Thermodynamics of Oxolysis

As oxolysis of the impurity metal chlorides is thermodynamically favoured at temperatures between 0-1000 °C, the equilibrium conversion of each metal chloride was calculated by GEM. Stochiometric amounts of the metal chloride and $O_2$ was used as input species. Figure 4.25 displays the results of these calculations. The equilibrium conversion of $FeCl_3$ and $FeCl_2$ decreases significantly as the temperature is increased above 500 °C. A decrease in the equilibrium conversion of $TiCl_4$ can also be observed, but it is not as severe and it occurs at a higher temperature. The conversion of $SiCl_4$ is independent of the temperature of the oxolysis, in the temperature range investigated.

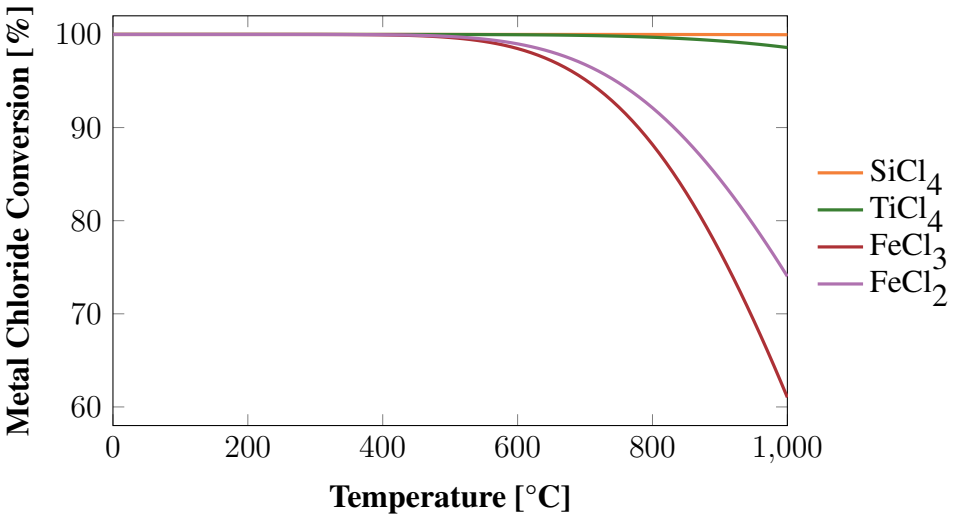


**Figure 4.25:** Equilibrium conversion of metal chlorides through oxolysis, calculated by GEM.

# Chapter 5

# Discussion

## 5.1 Characteristics of the Calcined Bauxite

As $\gamma$-$Al_2O_3$ has found to be more reactive than $\alpha$-$Al_2O_3$, it is desirable to promote the formation of $\gamma$-$Al_2O_3$ during the preparation of bauxite for carbochlorination[15, 21]. The XRD diffractogram of the milled bauxite powder in Figure 4.12 revealed that the major $Al_2O_3$ precursor in the bauxite investigated in this work is gibbsite. According to the thermal treatment scheme in Figure 2.2 gibbsite can either form $\chi$- or $\gamma$-$Al_2O_3$ during thermal treatment to 750 °C. Which route the gibbsite proceeds through during thermal treatment is dependent on the particle size and heating rate utilised[35]. The milled bauxite powder had a particle size of less than 300 µm, meaning that both the reaction pathways are preferred. However, the high calcination heating rate of 200 °C $h^{-1}$ promotes the formation of $\gamma$- over $\chi$-$Al_2O_3$. The appearance of two endothermic peaks with associated mass losses at 250 and 500 °C, respectively, during thermogravimetric analysis (TGA) and differential thermal analysis (DTA) of similar bauxite samples during the specialisation project indicate that the route forming $\gamma$-$Al_2O_3$ is dominating[57]. The TGA and DTA curves can be found in Appendix A. It should be noted that the TGA and DTA was performed with a higher heating rate than the calcination, further facilitating the formation of $\gamma$-$Al_2O_3$.

The XRD diffractogram of the calcined bauxite in Figure 4.13 revealed that the calcined bauxite contained both $\gamma$- and $\chi$-$Al_2O_3$. It is to the best of the authors' knowledge unknown how $\chi$-$Al_2O_3$ reacts during carbochlorination. However, the possible high surface areas seen for this transition alumina leads to the assumption that it reacts similarly to $\gamma$-$Al_2O_3$[34]. The presence of $\alpha$-$Al_2O_3$ could neither be confirmed nor disregarded, resulting in the conclusion that if it is present, it is present in small amounts. BET measurements of the milled bauxite powder and the calcined bauxite in Table 4.2 displayed a significant increase in surface area as a result of calcination.

The chemical composition of the calcined bauxite in Table 4.1 revealed that it contained considerable amounts of $SiO_2$ and $Fe_2O_3$, in addition to smaller amounts of $TiO_2$. Since the bauxite only contains minor amounts of alkali and earth alkali metal-compounds, the effect of any molten metal chlorides during carbochlorination is expected to be minor. As seen in the diffractogram of the calcined bauxite, $Fe_2O_3$ is present in the form of hematite and $TiO_2$ is present in the form both rutile and anatase. Despite the considerable amount of $SiO_2$ present, only minor peaks of quartz could be observed in the diffraction pattern. No other Si containing phases could be identified, meaning that the physical state of the Si component in calcined bauxite is to some degree unknown. It is possible that it is present as metakaolin, from the calcination of nacrite or as amorphous $SiO_2$, both of which would

display broad "waves" in the diffraction pattern[55, 87]. Such a broad wave can be seen in the diffraction pattern between 10-20°, however this is in all probability not caused by the aforementioned phases as the broad waves from these phases would lie around 20-30°[88, 89].

As the bauxite is calcined, the amount of smaller dust-like particles increases significantly. This can be seen in the SEM micrographs of the milled bauxite powder and calcined bauxite in Figure 4.19a and 4.20a, respectively. A possible explanation for this increase in smaller particles is that they are released when any free and bound moisture is removed from the structure. During the structural rearrangements associated with these reactions, it is possible that smaller sections of the outer part of the particles are released. Furthermore, the calcined $Al_2O_3$ particles displayed a cracked surfaces, compared to the flat, lamellar structure of gibbsite in Figures 4.20c and 4.19c, respectively. These cracks are most likely formed by strains induced by the structural disorder in the produced $\gamma$- and $\chi$-$Al_2O_3$ or by high internal water pressures[34].

## 5.2 Conversion

### 5.2.1 Overall Conversion

The conversion of bauxite during carbochlorination is found to increase steadily as the carbochlorination time is increased, as seen in Figure 4.1. Both the conversion based on mass loss and the conversion based on the amount of $Cl_2$ in the NaOH-scrubber seems to follow somewhat the same general pattern, except for the measurement at 15 min. At this stage, the conversion based on mass loss is larger than both the conversion based on the $Cl_2$ in the NaOH-scrubber and the thermodynamically estimated conversion. The reason for this may be that some unreacted bauxite travelled through the reactor and into the condenser, without being carbochlorinated, as the pore size of the bed filters was 100-160 µm.

The measured conversion is smaller than what is predicted thermodynamically. This is expected, as the thermodynamical calculations assume that the reaction reaches equilibrium instantaneously and do not take into account reaction kinetics. The increasing difference between the measured and estimated bauxite conversion is reflected in the decreasing $Cl_2$ conversion as carbochlorination proceeds, displayed in Figure 4.3. Despite the difference for the thermodynamically estimated conversion, it is clear that the carbochlorination of bauxite results in relatively high conversions. During the first 15 min of carbochlorination, $Cl_2$ conversions of more than 95% are observed, indicating a rapid reaction.

The decreasing $Cl_2$ conversion can be attributed to the increasing porosity of the powder beds in the reactor. As seen in Figure 4.4, the bed height reduction is not significantly increased after a bauxite conversion of $\sim$25% is reached. Even as a bauxite conversion of almost 90% is reached, the bed height reduction is only at 60%. This indicates that a porous network is developed in between the particles in the beds, as the carbochlorination proceeds. This porous network allows for CO and $Cl_2$ for find quicker paths through the powder, eventually leading to channels. This channel development is described in Figure 5.1. As CO and $Cl_2$ find quicker paths through the bauxite powder, the powder will have less time

to react with the passing CO and $Cl_2$, resulting in a reduced conversion. To mitigate this problem, higher powder beds could be utilised.

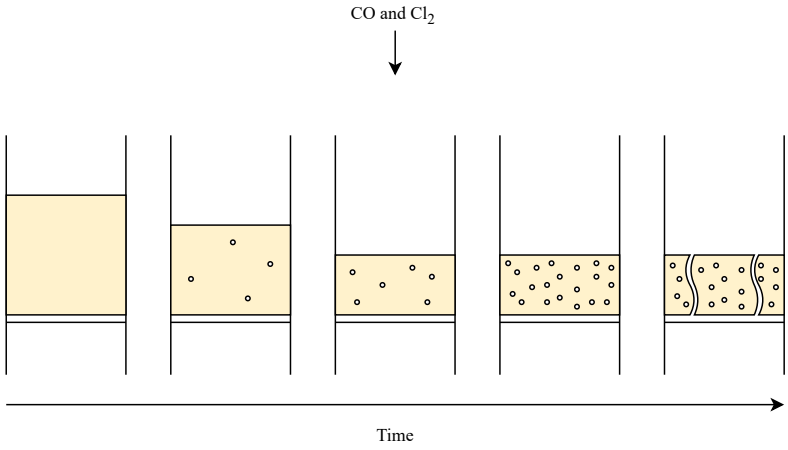


**Figure 5.1:** Development of a porous network in the powder bed as the carbochlorination proceeds.

### 5.2.2 Bauxite Conversion in the Three Reactor Beds

The thermodynamic estimations of the bauxite conversion in the three beds indicated that a stagnant conversion in the lower beds, as beds above were carbochlorinated, due to the back-reaction of the produced metal chlorides. In the measured conversion for the three beds, the back-reaction of the metal chlorides are not significant enough to give a stagnant conversion in the two lower beds. This can for instance be observed by the measured conversion in the bottom bed, which is increasing from 15 to 45 min, despite thermodynamics estimating it to be stagnant. However, it is clear that the bauxite conversion is heavily dependent on bed height as the top bed reaches a near 90% conversion of bauxite after 75 min of carbochlorination, while the bottom bed has only reached a bauxite conversion of just over 30%. The measured conversion in the top bed at 15 min is in agreement with the thermodynamically estimated conversion, indicating the high carbochlorination rate at this stage. As the carbochlorination proceeds for 45 and 75 min, there is less agreement between the measured and thermodynamically estimated conversions, somewhat because of the channelling development described above, and because all three reactor beds react at the same time.

## 5.3 Element Removed

The measured elemental removal in the top bed in Figure 4.5 indicated that the elements in bauxite carbochlorinated in the following sequence, Fe, Si/Ti and lastly Al. This is in contrast to the thermodynamically estimated elemental removal, which indicated that Al species should be preferentially carbochlorinated over Si. It is likely that this difference is related to the kinetics of the carbochlorination reactions. Landsberg (1975) found that Al compounds were preferentially removed over Si compounds, as predicted thermodynamically[15]. In his

study, the bauxite was calcined at 1000 °C, a significantly higher temperature compared to the 750 °C utilised in this work. It is possible that this difference in calcination temperature can explain the difference in Al and Si reactivity. However, as the calcination temperature is increased, $Al_2O_3$ in bauxite should transform into lower surface area transition aluminas, rendering the Al component in bauxite less reactive. It would therefore be expected that the Al component in Landsbergs investigations would be less reactive than the Al component in the bauxite investigated in this work, yet the opposite is observed. It becomes clear in the middle and bottom beds, displayed in Figures 4.6 and 4.7, respectively, that Si is preferentially carbochlorinated over Ti, again differing from what is thermodynamically predicted. This is also contradicting the findings of Landsberg (1975), who found that Ti would be preferentially carbochlorinated over Si.

The thermodynamical calculations predict that the produced metal chlorides entering the middle and bottom bed, would affect the carbochlorination significantly, as they were thermodynamically found to chlorinate certain of the species in these beds. Which metal chlorides that would be used for this chlorination is determined by the preferred reaction sequence. For instance, as Fe will thermodynamically be carbochlorinated first, any $FeCl_3$ entering the middle and bottom bed would not chlorinate any unreacted species in these beds, however all other metal chlorides entering the middle and bottom bed would chlorinate Fe. As Ti is the second element to be removed, any $TiCl_4$ entering the middle and bottom bed would chlorinate any Fe species in these beds, while leaving all Si and Al unreacted. Ti itself, would be chlorinated by any $AlCl_3$ or $SiCl_4$, but not by $FeCl_3$, and so on. As the metal chlorides chlorinates other species, they are themselves deposited in the reactor bed.

Comparing the Fe removal in the top, middle and bottom bed indicates that the carbochlorination of Fe containing species are relatively unaffected by the presence of gaseous metal chlorides. The comparison of the elemental removal of Fe in the different beds is displayed in Figure 5.2. A slight reduction of maximum Fe removal can be seen in the bottom bed compared to the top bed. This is most likely due to the lower CO and $Cl_2$ partial pressures in the bottom bed. Fe is not fully removed in either of the beds. Comparing the Fe containing phases of the XRD diffractograms of calcined bauxite and carbochlorinated bauxite from the different reactor beds, revealed that Fe is present as hematite in both the calcined and carbochlorinated bauxite. Therefore, the residual Fe is not reacted into a phase resistant to carbochlorination. The incomplete removal of Fe is therefore probably due to the statistically lower chance for $Cl_2$ and CO to find unreacted Fe containing particles, as the amount of Fe decreases.

Comparing the Si and Ti removal in the top, middle and bottom bed indicates that the carbochlorination of Si and Ti containing species are affected by the presence of gaseous metal chlorides. A comparison of the elemental removal of Si and Ti in the different beds are displayed in Figures 5.3 and 5.4, respectively. The negative elemental removal at 15 min of both Si and Ti in the bottom bed indicates that the produced $SiCl_4$ and $TiCl_4$ will carbochlorinate unreacted bauxite. As Fe is the only element removed after 15 min in the bottom bed, the gaseous $SiCl_4$ and $TiCl_4$ are probably used chlorinate $Fe_2O_3$ according to

$$3\,SiCl_4 + 2\,Fe_2O_3 \rightleftharpoons 3\,SiO_2 + 4\,FeCl_3 \tag{5.1}$$

$$3\,TiCl_4 + 2\,Fe_2O_3 \rightleftharpoons 3\,TiO_2 + 4\,FeCl_3. \tag{5.2}$$

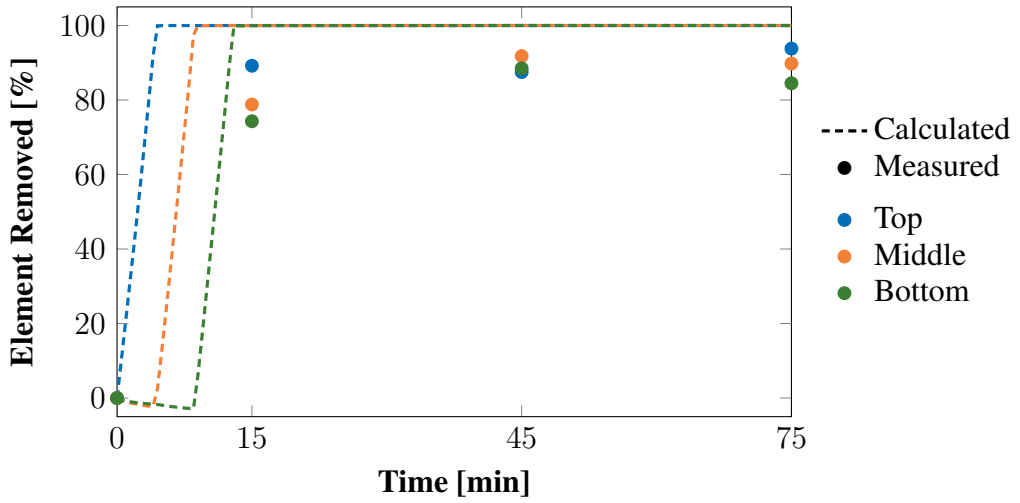


**Figure 5.2:** Elemental removal of Fe in the top, middle and bottom bed during carbochlorination.

Previous investigation has indicated that the carbochlorination rate of $SiO_2$ is significantly decreased by the presence of $SiCl_4$ in the gas stream[16, 31]. However in Figure 5.3, the elemental removal of Si in the middle and bottom bed at 45 and 75 min are comparable to that of the top bed, indicating that $SiO_2$ can carbochlorinate at a appreciable rate, despite the presence of $SiCl_4$. In fact, the larger differences between the elemental removal of Ti in the middle and bottom bed, compared to the top bed, indicates that the carbochlorination rate of $TiO_2$ is more affected by the presence of metal chlorides in the gas phase, than the carbochlorination rate of $SiO_2$.

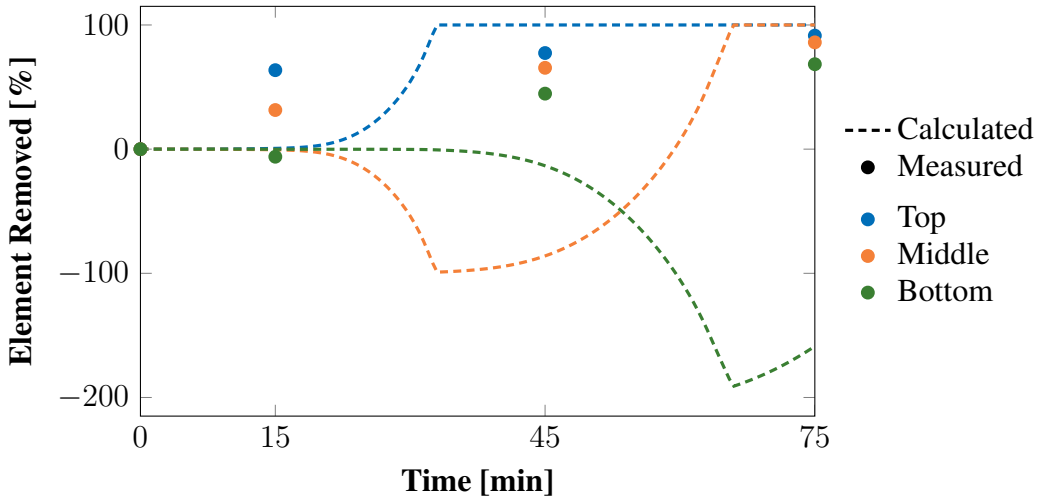


**Figure 5.3:** Elemental removal of Si in the top, middle and bottom bed during carbochlorination.

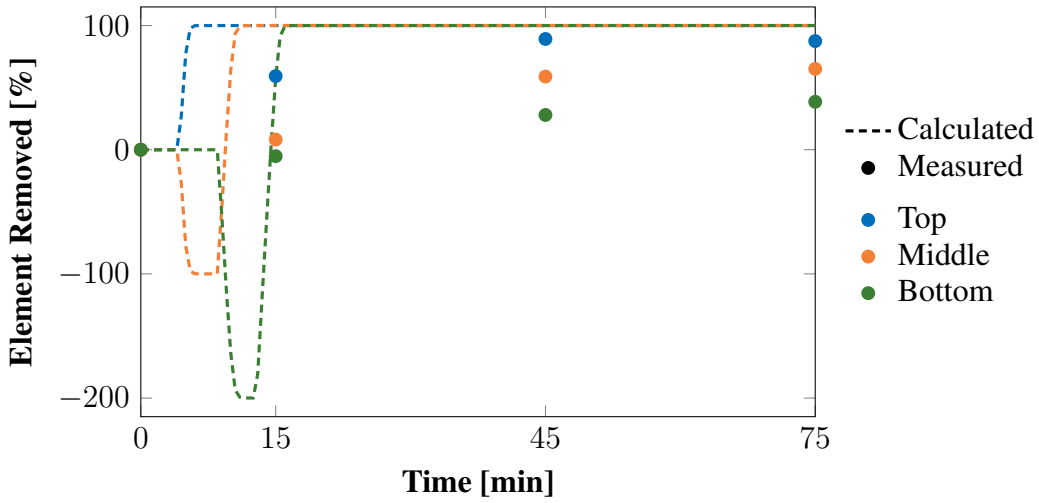


**Figure 5.4:** Elemental removal of Ti in the top, middle and bottom bed during carbochlorination.

Comparing the Al removal in the top, middle and bottom bed indicates that the carbochlorination of Al containing species are severely affected by the presence of gaseous metal chlorides. The comparison of the elemental removal of Al in the different beds is displayed in Figure 5.5. The negative elemental removal in the middle bed at 15 min indicates that produced $AlCl_3$ from the above beds chlorinate species in the unreacted bauxite, resulting in the deposition of $Al_2O_3$. This effect is the most severe in the bottom bed as a net-zero elemental removal of Al can be observed at all stages of carbochlorination. As $AlCl_3$ only can thermodynamically chlorinate $Fe_2O_3$ and $TiO_2$, the chlorination by $AlCl_3$ can be assumed to proceed according to

$$2\,AlCl_3 + Fe_2O_3 \rightleftharpoons Al_2O_3 + 2\,FeCl_3 \tag{5.3}$$

$$4\,AlCl_3 + 3\,TiCl_4 \rightleftharpoons 2\,Al_2O_3 + 3\,TiO_2. \tag{5.4}$$

The diffraction patterns of the bottom bed revealed that $Al_2O_3$ is mainly present in the $\chi$- and $\gamma$-form. This indicates that the deposition of $Al_2O_3$ in the lower beds produce these forms of $Al_2O_3$, and not the nonreactive $\alpha$-$Al_2O_3$, which would be detrimental to the carbochlorination of $Al_2O_3$ in the bottom bed. The net-zero elemental removal of Al in the bottom bed indicates either that $Al_2O_3$ does not react at all in the bottom bed or that the chlorination by $AlCl_3$ and the carbochlorination of $Al_2O_3$ occurs at comparable rates and to the same extent. The lower CO and $Cl_2$ partial pressures in the lower bed and the reduction of carbochlorination rate of $Al_2O_3$ due to the presence of $SiCl_4$ as found by Milne (1975), may also be important factors when explaining the net-zero elemental removal[31].

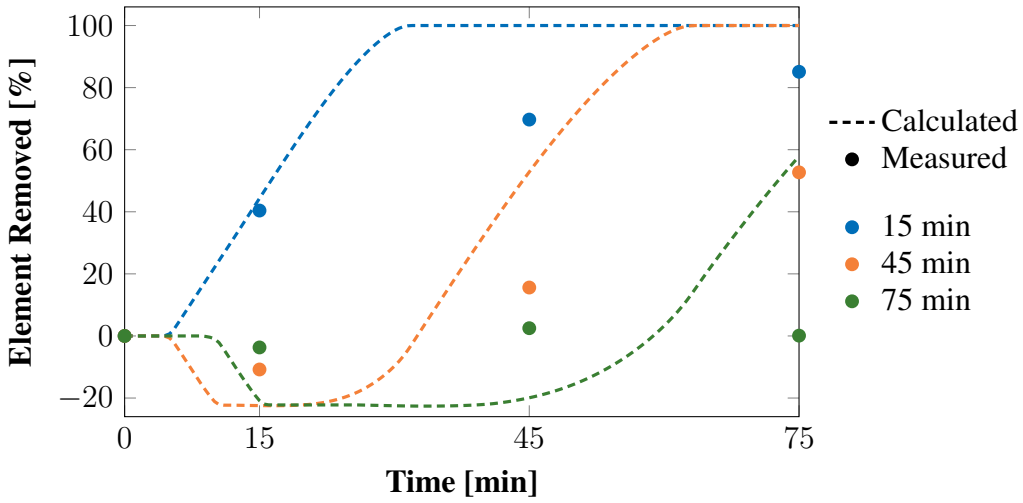


**Figure 5.5:** Elemental removal of Al in the top, middle and bottom bed during carbochlorination.

## 5.4 Changes in Phases Present

Mullite and $FeCl_2 \cdot 2\,H_2O$ could not be observed in the calcined bauxite, however, they were observed in the XRD diffractograms of the carbochlorinated bauxites. No identification of $\alpha$-$Al_2O_3$ in the calcined bauxite could be made, however it is clearly identified in the carbochlorinated bauxites. As these phases was not present prior to the carbochlorination, they must have been produced as a result of carbochlorination. $FeCl_2 \cdot 2\,H_2O$ can mostly be observed in the latter stages of carbochlorination, while $\alpha$-$Al_2O_3$ can be observed at all stages of carbochlorination. Mullite is the only of these phases that cannot be observed in the 75 min diffraction patterns, the latest stage of carbochlorination measured in this work. Therefore, mullite must not only be produced by the carbochlorination, but it must also be removed by the same process.

$FeCl_2 \cdot 2\,H_2O$ is produced by the chlorination of hematite, according to Reaction 2.5. The carbochlorination produces anhydrous $FeCl_2$, however as the sample has been exposed to moisture in air, it has absorbed water. As seen in Table 2.2, $FeCl_2$ has a melting point at 677 °C, right below the temperature of the reactor during carbochlorination. This means that some of the produced $FeCl_2$ may not have left the reactor during carbochlorination. As suggested by Mehrotra et al. (1982), this formation of liquid and possibly solid metal chlorides during carbochlorination, may result in the reduction of the carbochlorination rate, due to the metal chloride depositing on top of unreacted particles[29]. However, due to the small intensities of the $FeCl_2 \cdot 2\,H_2O$ peaks in the diffractogram, this effect can be assumed to be minor in the bauxite investigated in this work. This is substantiated by the fact that no major reductions in the conversion of bauxite can be observed in Figure 4.1.

As mentioned, the identification of mullite in the diffraction patterns of the carbochlorinated bauxite and not in the calcined bauxite, indicates that it is produced as a result of the carbochlorination. Landsberg (1977) found that mullite formed as a result of $SiCl_4$ chlorinating $Fe_2O_3$ in kaolinitic clay[16]. If this is the case, it would be expected that the

amount of mullite produced would increase down the bed heights, being the highest in the bottom bed, as this bed would be exposed to the highest amount of $SiCl_4$. However, the opposite is observed in the diffraction patterns, as the formation of mullite is especially prominent in the top bed after 45 min of carbochlorination, indicated by the high intensity of the mullite peaks in this pattern. Another possibility is that mullite is produced by a high temperature transformation of $Al_2O_3$ and $SiO_2$. As seen by the enthalpies of the carbochlorination reactions in Table 2.1, all the carbochlorinations are exothermic. The heat released by the carbochlorination reactions may locally heat the any surrounding $Al_2O_3$ and $SiO_2$ enough that these phases transform into mullite. The lack of mullite in the lower beds may then be explained by the lower temperatures in these beds, and the fact that less heat has been released as the carbochlorination has not proceeded to the same extent as for the top bed. Mullite is reported to be relatively non-reactive during carbochlorination, but the fact that mullite is completely removed from 45 to 75 min of carbochlorination, indicates that mullite actually do react during carbochlorination[56].

As for mullite, the formation of $\alpha$-$Al_2O_3$ during carbochlorination may be a result of the local heating of $\gamma$-$Al_2O_3$, due to heat being released by the different reactions taking place in vicinity of the particle. Similarly, as for mullite, this is substantiated by the fact that the intensity of the $\alpha$-peaks decreases from the top to the middle bed, corresponding to the decrease in reactor temperature, and less heat released as the carbochlorination has not proceeded to the same extent. Furthermore, the fact that the $\alpha$-$Al_2O_3$ peaks in the diffraction patterns for the carbochlorinated bauxites from the top bed increases from 45 to 75, despite the residue bauxite containing the same wt% of $Al_2O_3$, indicates that the amount of $\alpha$-$Al_2O_3$ increases as a function of carbochlorination time. Landsberg (1975) argued that the presence of other species in bauxite affected the $\gamma$- to $\alpha$-transition as due to the local heat produced during carbochlorination[15], without experimentally investigating it. The observation in phases present during carbochlorination substantiates this theory.

## 5.5 Changes in BET Surface Area

The obtained BET surface area as a function of conversion in Figure 4.18 display an initial drop in surface area at $\sim$10% conversion. As seen in Table 4.3, this corresponds to the 15 min carbochlorination of the middle and bottom bed. The decrease can be a result of a number of reasons, for instance

- the removal of high surface area $Fe_2O_3$, as Fe is the only element removed at this stage in the bottom bed in Figure 4.7,
- transformation of $\gamma$-$Al_2O_3$, adjacent to carbochlorinating $Fe_2O_3$, to low surface area $\alpha$-$Al_2O_3$ due to the local heat produced by the carbochlorination

After the initial decrease, the surface area increases at $\sim$25% conversion, before a final decrease in surface area at conversions higher than 25%. This is similar to what Landsberg (1975) found during carbochlorination of bauxite[15]. He gave no explanation for the observed surface area changes, other than that the low surface areas obtained at high conversions was a result of $\alpha$-$Al_2O_3$ and non-reactive $SiO_2$ being the only remaining phases. This might be applicable for the bauxite investigated in the present work, as the

intensity of the $\alpha$-peaks in the XRD diffractograms for the carbochlorinated bauxite from the top bed in Figure 4.14 increases as the length of the carbochlorination increases, which corresponds with the reduction in surface area. Furthermore, the $\alpha$-peaks has a significantly lower intensity in the diffraction patterns for the carbochlorinated bauxite from the bottom bed in Figure 4.16, which corresponds with the higher surface area bauxite samples.

## 5.6 Changes in Particle Morphology

The investigation in the scanning electron microscope revealed the formation of a porous structure in the $Al_2O_3$ particles during carbochlorination. This was especially visible in the top bed after 15 and 45 min of carbochlorination, displayed in Figures 4.21 and 4.22, which corresponds to an elemental removal of Al of 40 and 70%, respectively. The development of this porous structure indicates that the $Al_2O_3$ particles do not react uniformly during carbochlorination. However, it seems as if the reaction is initiated at different spots on the particle, creating a microscopic pore. When the reaction has occurred at these spots, it appears that the pore has a higher carbochlorinating reactivity than the unreacted parts of the particle, causing the formation of growing, visible pores in the micrograph. The fact that the pores in the micrograph in Figure 4.21c, are localised in different areas of the particle, may indicate that the particle surface adjacent the created pore, also displays a higher reactivity. As no such porous particles are present in the top bed after 75 min, suggest that the pore structure continuously develops, eventually consuming the reactive part of the particle and leaving behind a smaller, possible non-reactive $\alpha$-$Al_2O_3$ particle. Such a development of a smaller particle is further substantiated by the major decrease in particle size compared to the calcined material, as displayed in Figure 5.6.

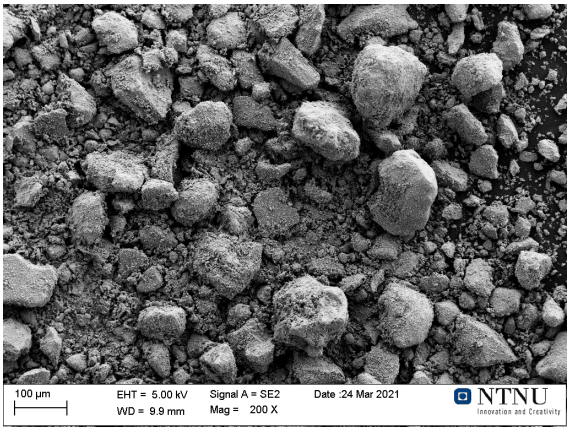


**(a)** Calcined bauxite.

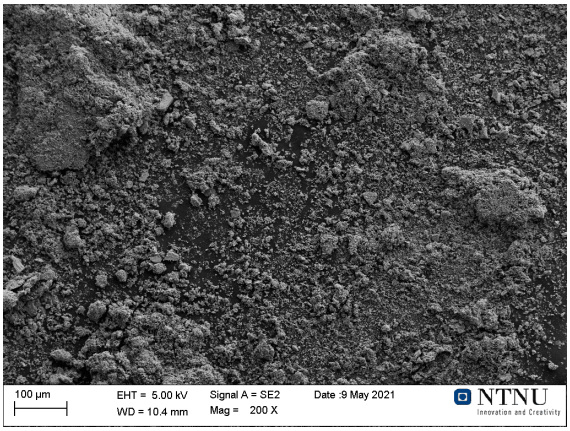


**(b)** Bauxite from the top bed carbochlorinated for 75 min.

**Figure 5.6:** Changes in particle size during carbochlorination of bauxite.

The development of a pore structure could also be observed in the bottom bed after 75 min of carbochlorination, despite $Al_2O_3$ displaying a 0.1% elemental removal in this bed. As mentioned in Section 5.3, the thermodynamical calculations predicts that $AlCl_3$ produced from the top and middle bed, will react with $Fe_2O_3$ and $TiO_2$ in the middle bed, until no more of these phases are left, resulting in a negative elemental removal. If $Al_2O_3$

carbochlorinates concurrently with this back-reaction and at the same rate, the net-elemental removal would be equal to zero. This net-zero conversion is experimentally observed for the bottom bed in Figure 4.7. Based on the assumption that the porous structure is a result of the carbochlorination of $Al_2O_3$, it seems plausible that the $Al_2O_3$ carbochlorinates to a certain extent in the bottom bed, however, its conversion is equalised by the back-reaction occurring at the same extent.

The particles found in the top bed after 45 min of carbochlorination in Figure 4.22, were unique, and could not be found in any of the other samples of carbochlorinated bauxite. It is clear that these particles are not the dominating particle type in this sample, as seen in the low magnification micrograph in Figure 4.22a. Instead they appear as a cluster. The small particle size of $\sim$4 µm and the hexagonal structure leads to the assumption that these are $\chi$-$Al_2O_3$ pseudomorphs of gibbsite[34, 35]. Based on the significant evolution of pores within the particles, it appears that that these $\chi$-particles are highly reactive during carbochlorination.

## 5.7 Purity of Produced Metal Chlorides

The purity of the produced metal chlorides in the condenser were investigated by ICP-MS. Because some of the metal chlorides condensed on the walls of the condenser, the extraction of representative samples of the metal chlorides from the condenser was difficult and the results are only indicative. Only a simple condensation scheme with one condenser at RT was utilised. Based on the melting and boiling points in Table 2.2, only $AlCl_3$, $FeCl_3$ and $FeCl_2$ would condense as solids in the condenser. $SiCl_4$ and $TiCl_4$ should condense as liquids. However, only solid phases could be observed in the condenser, indicating that $SiCl_4$ and $TiCl_4$ was carried over to the NaOH-scrubber.

As expected from the melting points of the chlorides, the only metal chlorides found in significant amounts in the condenser are $AlCl_3$ and $FeCl_3$. From 15 to 45 min of carbochlorination the amount of $FeCl_3$ in the condenser increases, despite the fact that only a small increase of Fe removal can be observed in the reactor at these stages in Figures 4.5-4.7. It is possible that this increase lies within the error associated with the heterogeneous nature of the samples investigated. Another possibility is that the iron chloride present in the condenser after 15 min is mainly $FeCl_2$. As unreacted $Cl_2$ is passed through the condenser from 15 to 45 min, this $FeCl_2$ can be transformed into $FeCl_3$ increasing the weight of the iron chloride without more iron chloride actually being deposited in the condenser. From 45 to 75 min the amount of $AlCl_3$ in the condenser increases, as expected from the elemental removal curves, where the amount of $Al_2O_3$ carbochlorinated is found to increase while no more Fe compounds are reacted.

Reductive distillation has been suggested as a method for separating $AlCl_3$ from $FeCl_3$[7, 17]. To achieve an appreciable reaction rate during distillation, an upper limit of 5% non-$AlCl_3$ species had to be maintained. Given the high amounts of $FeCl_3$ in the condenser after 75 min of carbochlorination it is clear that other separation techniques must be utilised prior to the reductive distillation. Carbochlorination for a longer period of time might reduce the impurity amounts of $FeCl_3$. Regardless, the amount of $FeCl_3$ in the condenser is unlikely

to fall below the necessary 5% because of the high amounts of Fe species in the calcined bauxite, as seen Table 4.1. Utilising two condensers at different temperatures, such as Namboothiri and Mallick (2017) did during their investigations, a preliminary distillation of $FeCl_3$ from $AlCl_3$ can be performed[7]. The temperature of the condensers was not specified in their work. They reported $AlCl_3$ purities up to 94% by this method. It should be noted that the $Fe_2O_3$ content of the bauxite investigated in their work was almost half of the $Fe_2O_3$ content in the bauxite investigated in this work. Therefore, purities as high as 94% is not to be expected.

As seen by the low amounts of $SiCl_4$ in the condenser, it is evident that this is carried with the gas phase into the NaOH-scrubber. This indicates that $SiCl_4$ can be effectively removed from $AlCl_3$ by simple distillation, as suggested by several authors[7, 17]. The amount of $TiCl_4$ in the metal chlorides from the condenser is also particularly low. However, as seen in the chemical composition of the calcined bauxite in Table 4.1, only small amounts of $TiO_2$ is present in the bauxite. Therefore, it is likely that the measured amount of $TiCl_4$ in the produced metal chlorides in the condenser lies within the error associated with obtaining the samples. As the amount of $TiCl_4$ in the produced metal chlorides would be quite low regardless, due to the low amount in the calcined bauxite, any remaining $TiCl_4$ could probably be removed by either simple or reductive distillation.

## 5.8 Applicability of the Shrinking Core Model

A kinetic model was not applied to the measured conversions from the carbochlorination of bauxite, due to the small amount of data collected. Three essentially equal carbochlorination experiments were performed, as the temperature and flow rates of CO and $Cl_2$ was not changed between the three experiments. Because of this, assumptions such as whether the carbochlorination is reaction or mass transfer controlled, cannot be made. However, based on results in the present work, the applicability of the SCM, as suggested for the carbochlorination of $Al_2O_3$ in the same reaction environment, can be discussed[67].

Whether the particles in bauxite actually react as shrinking cores, is somewhat ambiguous. As described in Section 5.6, it appears as if a porous structure is developed on the $Al_2O_3$ particles during carbochlorination, without the particles actually shrinking. However, a significant decrease in particle size can also be observed as a result of the carboclorination. If this particle size reduction is a result of the particles shrinking during carbochloination, the porous structure developing through the particle, eating it from the inside out or a combination of the two remains unclear. However, as the SCM has been found to be applicable during the carbochlorination of $Al_2O_3$ at the same temperature and in a similar reactor setup, the assumption of the reacting as shrinking cores appear as applicable nonetheless[67].

The geometry assumption in the SCM, that all the particles are spherical, not not seem fully applicable to the irregular shaped particles in the calcined bauxite displayed in Figure 4.20. However, the use of other general shapes such as cubes, flat plates or cylinders does not appear more descriptive. Therefore, the assumption of spherical particles appears as a first approximation in the model.

As seen by the elemental removal diagrams in Figures 4.5-4.7 and changes in chemical composition during carbochlorination in Figures 4.8-4.10, it is clear that bauxite does not react as a homogeneous material, as assumed by the SCM. The carbochlorination takes place through several different reactions, with each their separate reaction rate. Whether the rate determining step is the surface reaction or mass transfer does not need to be the same for all the reactions. This complicates the application of the SCM to the carbochlorination of bauxite as a whole.

A further complication of the application of the SCM to the carbochlorinaiton of bauxite, is whether the particles react according to the first or second SCM route described in Figure 2.6. As the different constituents in bauxite are carbochloinated by CO and $Cl_2$ according to Reactions 2.1-2.5, all the products are gaseous, meaning that the first SCM route would be applicable. However, as mentioned, it is also likely that the carbochlorination proceeds by the produced metal chlorides chlorinating other metal oxides, especially in the two lower beds. This would result in the formation of a solid product, which probably would deposit on the surface of the particle it is chlorinating, meaning that the reaction also can follow the second SCM route.

Because the bauxite does not carbochlorinate as a homogeneous material, a possible application of the SCM model to bauxite is by the application of the SCM to the carbochlorination of each of the major constituents of bauxite separately before combining the separate models into one. By this procedure, the composition of bauxite could be accounted for. This is advantageous as the composition of bauxite varies depending on where it is recovered from[32]. From the elemental removals in Figure 4.5-4.7 it is clear that carbochlorination reactions occur at the same time, and that one metal oxide is not fully removed before the carbochlorination of another metal oxide starts. Because of this, the rate of the carbochlorination of each species in bauxite has to be estimated in relation to one another during the carbochlorination of bauxite, and then applied to the reaction model.

One limitation of this approach is that the different constituents of bauxite may interact during carbochlorination of bauxite. For instance, during the carbochlorination, mullite was found to be formed during carbochlorination, as seen in the XRD diffractogram of carbochlorinated bauxite in Figure 4.14. Since mullite was not found in the diffraction pattern of the calcined bauxite in Figure 4.13, it must have been formed as a result of the carbochlorination. Mullite consists of both $Al_2O_3$ and $SiO_2$. By applying the SCM to the carbochlorination of $Al_2O_3$ and $SiO_2$ separately, the formation of species such as mullite will not be included in the estimations. Furthermore, the reaction between unreacted bauxite and formed metal chlorides will not be included and must be assumed as negligible in the model.

## 5.9 Process Scale-Up

The high conversion obtained during carbochlorination at 700 °C in this work, indicates that bauxite is a suitable mineral for carbochlorination. However, as found in the elemental removals, the Al component in bauxite is the last major constituent of bauxite to be carbochlorinated. This makes the direct carbochlorination of bauxite a less suitable option

as a commercial production route for $AlCl_3$. Furthermore, the amount of $FeCl_3$ in the condenser was found to be too high for separation by reductive distillation, according to Namboothiri and Mallick (2017)[7]. The formation of non-reactive $\alpha$-$Al_2O_3$, will also lead to problems if the process is to be continuous, as residue of $\alpha$-$Al_2O_3$ will build up in the reactor over time. Therefore, the direct carbochlorination of bauxite with only one condenser as utilised in this work, may not be the optimal option for producing $AlCl_3$ for the production of metallic Al.

A sequential carbochlorination, as suggested by Raval and Dixit (1979) and Namboothiri and Mallick (2017) serves as a possible alternative to direct carbochlorination, which can solve the issues with to much $FeCl_3$ in the condenser[7, 33]. The elemental removals indicated that more than 70% of all Fe containing species in bauxite could be removed within the first 15 min of carbochlorination. For the top bed, the removal was higher than 90%. Performing a two-stage carbochlorination where bauxite is first carbochlorinated at 15 min to remove most of the Fe containing species, and afterwards carbochlorinated to produce $AlCl_3$, may serve as a possible production route. However, this route would result in some loss of Al containing species, as 40% of Al was removed along with Fe in the top bed after 15 min of carbochlorination. A shorter carbochlorination time may result in smaller Al losses, however, it may also result in a lower removal of Fe. Performing the first step of carbochlorination, where Fe is removed at a lower temperature may also be a possible solution, as Raval and Dixit found the Al loss to be lower at lower temperatures. However, this would also resulted in the decreased removal of Fe[33].

A modification of the sequential carbochlorination, utilising the effect that the gaseous metal chlorides have on the carbochlorination of $Al_2O_3$ serves as another alternative. The elemental removal of Al in the bottom bed revealed that a net-zero removal of Al is achieved when bauxite is subjected to low CO and $Cl_2$ partial pressures and metal chlorides, such as $FeCl_3$, $SiCl_4$, $TiCl_4$ and $AlCl_3$. Under these conditions, almost 90% of Fe containing species was removed from the bauxite. As observed in the SEM micrograph of the bauxite from the bottom bed in Figure 4.24b, $Al_2O_3$ is carbochlorinated to some degree in the bottom bed after 75 min. However, the net amount of $Al_2O_3$ is maintained by the chlorination of other metal oxides by entering $AlCl_3$, resulting in the deposition of $Al_2O_3$. This makes it necessary to have a certain amount of $AlCl_3$ in the gas stream, to avoid the net loss of $Al_2O_3$.

As mentioned, the amount of $FeCl_3$ in the condenser was found to be too high for separation by reductive distillation, according to Namboothiri and Mallick (2017)[7]. Utilising either of the above-mentioned sequential carbochlorination techniques should yield a smaller amount of $FeCl_3$. However, the amount may still be higher than the 5% limit given by Namboothiri and Mallick. A preliminary separation of $AlCl_3$ and $FeCl_3$ may therefore be needed. This could potentially be done by simple distillation of $AlCl_3$ from $FeCl_3$, utilising a two-stage condenser system during carbochlorination, as mentioned in Section 5.7. However, further investigations are needed to determine if the $AlCl_3$ purity is high enough for reductive distillation.

The thermodynamic evaluation of oxolysis as a $Cl_2$ recovery technique, revealed that all $Cl_2$ from the carbochlorination of other species than $Al_2O_3$ in bauxite, should be recovered

at temperatures between 0-400 °C. Higher temperatures resulted in less $Cl_2$ being recovered from $FeCl_2$ and $FeCl_3$. The fact that oxolysis can thermodynmaically proceed at low temperatures, is advantageous in regard to the application of oxolysis as a commercial process. However, the process needs to be investigated experimentally, to determine if the process also display favourable kinetics.

## 5.10 Evaluation of the Reactor Setup

A specially built three-stage carbochlorination reactor was constructed for the experiments performed in this work. The objective of this three-stage reactor was to investigate how the formation of metal chlorides affected the carbochlorination of unreacted bauxite. As follows from the above discussions, the reactor fulfilled its purpose. For instance, the reactor setup allowed for the determination of elemental removal in each of the three beds, indicating whether each element was as readily removed in one bed as in the bed above. Little to none fallout was observed between the beds, except for the 15 min experiment, where bauxite from the bottom bed escaped into the empty bed below, however this was due to a production error and not due to the reactor setup itself.

## 5.11 Further Work

The work presented in this master's thesis has provided a better understanding of how the Al component in bauxite reacts during carbochlorination, and how it is affected by the carbochlorination of the other constituents of bauxite. Over the course of this work, several interesting topics have been revealed. However, a lot of research remains to fully understand the carbochlorination of bauxite. Furthermore, it is also some work remaining, which the author did not have enough time to do.

The lack of XRD measurements of the produced metal chlorides in the condenser makes it difficult to determine which chlorides that are formed. The ICP-MS yields information about the amount of each element in the condenser, from which certain assumptions of can be made about which chlorides that are present. However, some of the elements present can produce different metal chlorides, such as Fe which can be present as both $FeCl_3$ and $FeCl_2$. This is of importance as $FeCl_2$ can be readily separated from $AlCl_3$, while $FeCl_2$ cannot[7]. Furthermore, some of the elements can produce metal chloride complexes, such as $FeAlCl_6$. Because of this, the metal chlorides should be characterised by XRD and the phases present should be identified and preferably quantified.

A high bauxite conversion was found during carbochlorination in this work. Still, carbochlorinations were only performed up to a bauxite conversion of $\sim$70%. Longer carbochlorination experiments should be performed to investigate how the conversion develops as a function of time at conversions higher than 70% and to determine if 100% of bauxite is possible. If 100% conversion of bauxite is not possible, the residue should be characterised by XRD to determine the phases present and by XRF to determine the bauxite residues chemical composition. Higher powder beds should also be used during the carbochlorinations, to mitigate the effects of the channel formation as the powder bed grows more

porous.

As shown in this work, the carbochlorination of $Al_2O_3$ is highly dependent on the presence of metal chlorides in the gas phase. Yet, a lot of research remains to fully understand how the carbochlorination of $Al_2O_3$ are affected by the presence of the different metal chlorides. If the effect of the presence of different metal chlorides can be quantified, the carbochlorination of bauxite can either be tailored to achieve as a high carbochlorination rate of $Al_2O_3$ or tailored to purify the Al component of bauxite, followed by carbochlorination of this purified bauxite. As a first step in this quantification, $Al_2O_3$ could be exposed to the different metal chlorides separately, both with and without CO and $Cl_2$ in the gas stream. The conversion of $Al_2O_3$ could be measured during the metal chloride exposure, and $Al_2O_3$ could be characterised by XRD and XRF before and after the exposure to detect any changes in phases present and chemical composition.

The measured diffraction patterns of the carbochlorinated bauxite samples indicate that $\gamma$-$Al_2O_3$ is transformed into $\alpha$-$Al_2O_3$ during carbochlorination. As it has previously been found that $\alpha$-$Al_2O_3$ is significantly less reactive during carbochlorination, compared to $\gamma$-$Al_2O_3$, this $\alpha$-$Al_2O_3$ formation may be detrimental to the carbochlorination of bauxite[15]. Therefore, it is recommended that formation of $\alpha$-$Al_2O_3$ during carbochlorination is quantified, so that the carbochlorination of bauxite can be optimised to form as little $\alpha$-$Al_2O_3$ as possible. As the transformation of $\gamma$-$Al_2O_3$ into $\alpha$-$Al_2O_3$ is likely to be related to the temperature of the carbochlorination, the temperature dependency of this $\alpha$-$Al_2O_3$ formation, should also be determined.

The application of the SCM may prove useful for modelling kinetics of carbochlorination of bauxite, but considering the rather complex mineralogy of bauxite, much more data than provided in this work is required to construct meaningful kinetic models. By investigating the carbochlorination of the major constituents of bauxite separately, a SCM for bauxite could be constructed, taking into account the different chemical compositions which bauxite might exhibit. This approach has certain limitations, for instance it does not take into account any interactions between the different constituents, or the effect the produced metal chlorides has on the carbochlorination.

Finally, the recovery of $Cl_2$ from the metal chlorides by oxolysis must be further investigated. Only a thermodynamic evaluation of oxolysis was provided in this work. To fully evaluate the applicability of oxolysis as a recovery technique during carbochlorination, it also needs to be evaluated experimentally and the kinetics of the process must be determined.

# Chapter 6

# Conclusion

The objective of this master's thesis was to examine how the Al component in bauxite reacts during carbochlorination and how it is affected by the carbochlorination of the other constituents of bauxite, especially the presence of the gaseous metal chlorides produced by these carbochlorinations. This was achieved by subjecting bauxite to carbochlorination in a specially built three-stage reactor, to represent the top, middle and bottom part of a powder bed, and characterising the bauxite before and after carbochlorination. Prior to carbochlorination, bauxite was calcined at 750 °C, resulting in a significant increase in surface area and the formation of $\gamma$- and $\chi$-$Al_2O_3$ in the bauxite. The obtained conversion of calcined bauxite was high, yielding a $Cl_2$ conversion no lower than 80%. The produced metal chlorides were found to consist of 40-60 wt% $AlCl_3$, 30-60 wt% $FeCl_2$ and less than 0.2 wt% of $SiCl_4$ and $TiCl_4$.

The major constituents in bauxite were found to carbochlorinate in the following sequence on element basis: first Fe, then Si and Ti and lastly Al. This reaction sequence deviated from the findings of Landsberg (1975) and thermodynamical estimations, where Al containing species was found to be carbochlorinated more readily than Si containing species[15]. Furthermore, the presence of produced metal chlorides in the bottom bed was found to be detrimental to the carbochlorination of $Al_2O_3$. Negative elemental removals for Si, Ti and Al in the bottom bed indicated that the gaseous metal chlorides of these species chlorinated unreacted bauxite in the bottom bed, resulting in the deposition of the respective oxides. This back-reaction from $AlCl_3$ to $Al_2O_3$ resulted in a net-zero elemental removal of Al in the bottom bed after 75 min of carbochlorination.

The measured XRD diffractograms revealed that $\alpha$-$Al_2O_3$ was formed during the carbochlorination. This was especially visible in the top bed, where the effect of the produced metal chlorides was minimal. $\alpha$-$Al_2O_3$ was most likely formed as a result of local heating of $\gamma$-$Al_2O_3$ due to the exothermic carbochlorination of intimately associated components, inducing the transformation into $\alpha$-$Al_2O_3$. The formation of $\alpha$-$Al_2O_3$ was reflected in the decreasing BET surface area of bauxite as the carbochlorination proceeded.

During carbochlorination of bauxite, a porous structure developed on the surface of the $Al_2O_3$ particles. In addition, a significant decrease in particle size could be also observed. This led to a suggested mechanism for the particle development during carbochlorination. First, carbochlorination occurs at certain spots on the particle surface, leaving a pore with high carbochlorination reactivity. Because of this high reactivity, further carbochlorination is preferred to occur inside these pores, causing the pores to grow. Eventually, the pores will have grown so much, that the entire outer reactive part of the particle is consumed, leaving behind a smaller, possible non-reactive $\alpha$-$Al_2O_3$ particle.

# Bibliography


[1] The European Commission. *Communication from the Commission to the European Parliament, the European Council, the Council, the European Economic and Social Committee and the Committee of the Regions – The European Green Deal*. COM(2019) 640 final. The European Commission, 2019.

[2] T. Wyns and G. Khandekar. *Metals for a Climate Neutral Europe: A 2050 Blueprint*. Report. Institute for European Studies, Vrije Universiteit Brussel, 2019.

[3] World Aluminium. *Primary Aluminium Production*. `http://www.world-aluminium.org/statistics/#data`. Accessed 04.04.21. 2020.

[4] M. Akbar Rhamdhani et al. "Alternative Al Production Methods: Part 1. A Review." In: *Mineral Processing and Extractive Metallurgy IMM Transactions section C* 122.2 (2013), pp. 87–104.

[5] M. Gautam, B. Pandey, and M. Agrawal. "Carbon Footprint of Aluminum Production: Emissions and Mitigation." In: *Environmental Carbon Footprints*. Butterworth-Heinemann, 2017, pp. 197–228.

[6] Sintef. *Red Mud (Bauxite Residue) – An Unnecessary Problem?* `https://blog.sintef.com/industry-en/red-mud-unnecessary-problem/`. Accessed 05.04.20. 2019.

[7] S. Namboothiri and S. Mallick. "Bauxite Processing via Chloride Route to Produce Chloride Products and Subsequent Electrolysis of Aluminium Chloride to Produce Aluminium Metal." In: *Light Metals 2017*. Springer, Cham, 2017, pp. 641–648.

[8] Keith B. Oldham, Jan C. Myland, and BondAlan M. *Electrochemical Science and Technology: Fundamentals and Applications*. John Wiley Sons, Ltd., 2012.

[9] B. Øye. *Could the Chloride Process Replace the Hall-Héroult Process in Aluminium Production?* `https://blog.sintef.com/sintefenergy/energy-efficiency/could-the-chloride-process-replace-the-hall-heroult-process-in-aluminium-production/`. Accessed 04.05.21.

[10] H. W. Cotten. *The Alcoa Smelting Process at Andersen County Texas*. 2018.

[11] A. S. Russell. "Pitfalls and Pleasures in New Aluminum Process Development." In: *Metallurgical Transactions B* 12.2 (1981), pp. 203–215.

[12] B. Øye. *Carbochlorination routes in production of Al*. Report. SINTEF Industry, 2018.

[13] A. Atasoy. "Chlorination Process in Extractive Metallurgy." In: 2002, pp. 337–346.

[14] P. K. Jena and E. A. Brocchi. "Metal Extraction Through Chlorine Metallurgy." In: *Mineral Processing and Extractive Metallurgy Review* 16.4 (1997), pp. 211–237.

[15] A. Landsberg. "Chlorination Kinetics of Aluminum Bearing Minerals." In: *Metallurgical Transactions B* 6B (1975), pp. 207–214.

[16] A. Landsberg. “Some Factors Affecting the Chlorination of Kaolinic Clay.” In: *Metallurgical Transactions B* 8.2 (1977), pp. 435–441.

[17] A. Landsberg. *Aluminum From Domestic Clay Via a Chloride Process*. Information Circular 8923. United States Department of the Interior, Bureau of Mines, 1983.

[18] A. Landsberg and R. D. Wilson. “A Study of the Mechanisms of the Salt Catalyzed Carbochlorination of Kaolin.” In: *Metallurgical Transactions B* 15.4 (1984), pp. 695–700.

[19] K. Smith, S. Riemer, and I. Iwasaki. “Carbochlorination of Aluminum from Non-Bauxite Sources.” In: *Journal of Metals* 34.9 (1982), pp. 59–62.

[20] R. D. Holliday and D. J. Milne. “Experimental Evaluation of Routes for Purification of Bauxite by Gas-Solid Reactions.” In: *Industrial & Engineering Chemistry Process Design and Development* 14.4 (1975), pp. 447–452.

[21] D. J. Milne and R. D. Holliday. “Thermodynamics of Gas-Solid Reactions for Purification of Bauxite at Moderate Temperatures.” In: *Industrial & Engineering Chemistry Process Design and Development* 14.4 (1975), pp. 442–447.

[22] G. Baudet. *A Documentary Study on Alumina Extraction Processes*. Report. Bureau de Recherches Géologiques et Miniére, 1977.

[23] N. A. Gokcen. *Rates of Chlorination of Aluminous Resources*. Information Circular 8952. United States Department of the Interior, Bureau of Mines, 1983.

[24] M. J. Murtha and G. Burnet. “Recovery of Alumina From Coal Fly Ash By High Temperature Chlorination.” In: *Proceedings of the Iowa Academy of Science* 83.4 (1976), pp. 125–129.

[25] Zs. Roder, I. Bertóti, and T. Székely. “Reaction of Metakaolinite with Phosgene and Carbon Tetrachloride.” In: *Reactivity of Solids* 3.1-2 (1987), pp. 113–125.

[26] B. Grob and W. Richarz. “Chlorination of Alumina in Kaolinitic Clay.” In: *Metallurgical Transactions B* 15.3 (1984), pp. 529–533.

[27] H. Wijatno. *Aluminum Recovery from Coal Fly Ash by High Temperature Chlorination*. Master’s thesis. Iowa State University, 1977.

[28] D. J. Adelman and G. Burnet. “Carbochlorination of Metal Oxides with Phosgene.” In: *AlChE Journal* 33.1 (1987), pp. 64–69.

[29] A. K. Mehrotra et al. “High-Temperature Chlorination of Coal Ash in a Fluidized Bed. 1. Recovery of Aluminum.” In: *Industrial & Engineering Chemistry Process Design and Development* 21.1 (1982), pp. 37–44.

[30] Giuseppe Bombara and Rocco Tanzi. “Prospects for Carbochlorination in Aluminum Recovery from Italian Leucitites.” In: *JOM* 36.1 (1984), pp. 74–78.

[31] D.J. Milne. “Chlorination of Bauxite in the Presence of Silicon Tetrachloride.” In: *Metallurgical Transactions B* 6.3 (1975), pp. 486–488.

[32] A. J. Downs. *Chemistry of Aluminium, Gallium, Indium and Thallium*. Springer Netherlands, 1993.

[33] R. Raval and S. Dixit. “Some Aspects of the Chlorination of Bauxite.” In: *Journal of Chemical Technology and Biotechnology* 29.2 (2007), pp. 107–115.

[34] R. Prins. “On the structure of $\gamma$-$Al_2O_3$.” In: *Journal of Catalysis* 392 (2020), pp. 336–346.

[35] K. Wefers and C. Misra. *Oxides and Hydroxides of Aluminium*. Alcoa Laboratories Technical Paper N19. Aluminium Company of America, 1987.

[36] B. Ollivier et al. “Crystal Structure of $\kappa$-Alumina: An X-Ray Powder Diffraction, TEM and NMR Study.” In: *Journal of Materials Chemistry* 7.6 (1997), pp. 1049–1056.

[37] C. V. Chandran et al. “Alumina: Discriminative Analysis Using 3D Correlation of Solid-State NMR Parameters.” In: *Chemical Society Reviews* Advanced Article (2019), pp. 134–156.

[38] A. Vieira-Coelho et al. “Surface Area, Crystal Morphology and Characterization of Transition Alumina Powders from a New Gibbsite Precursor.” In: *Materials Research* 10.2 (2007), pp. 183–189.

[39] A. I. Tsvigunov et al. “Detonation Synthesis of a New Modification of Aluminum Oxide from Gibbsite by Explosion.” In: *Glass and Ceramics* 55.11 (1998), pp. 379–383.

[40] S. Louaer, Y. Wang, and L. Guo. “Fast Synthesis and Size Control of Gibbsite Nanoplatelets, Their Pseudomorphic Dehydroxylation, and Efficient Dye Adsorption.” In: *ACS Applied Materials & Interfaces* 5.19 (2013), pp. 9648–9655.

[41] I. Madsen and J. Hockridge. “In Situ X-ray Diffraction of the Transformation of Gibbsite to $\alpha$-Alumina Through Calcination: Effect of Particle Size and Heating Rate.” In: *Journal of Applied Crystallography* 42.4 (2009), pp. 697–705.

[42] D. Sanfilippo. “Dehydrogenations in Fluidized Bed: Catalysis and Reactor Engineering.” In: *Catalysis Today* 178.1 (2011), pp. 142–150.

[43] A. Grønvold. *Carbochlorination of Aluminium Bearing Minerals*. Summer Project. Norwegian University of Science and Technology, 2020.

[44] Roine, A. and Kobylin, P. *HSC Chemistry®*. Version 9.9.2.3.

[45] M. S. Dobbins. “Carbochlorination of Metal Oxides Using a Fused Salt Slurry Reactor.” Doctoral dissertation. Iowa State University, 1986.

[46] D. J. Adelman. “Kinetics of Coal Fly Ash Chlorination by Phosgene.” Doctoral dissertation. Iowa State University, 1984.

[47] D. J. Milne and L. J. Wibberley. “Chlorination of Alumina and Bauxite Using Pyrolytic Carbon as Reductant.” In: *ight Metals 1978*. The Metallurgical Society of AIME, 1978, pp. 147–162.

[48] I. Bertóti et al. “Kinetics of $\gamma$-Alumina Chlorination by Phosgene.” In: *Thermochimica Acta* 44.3 (1981), pp. 325–331.

[49] A. Tóth, I. Bertóti, and T. Székely. “Kinetics of $\gamma$-Alumina Chlorination by Carbon Monoxide and Chlorine.” In: *Thermochimica Acta* 52.1-3 (1982), pp. 211–215.

[50] I. Bertóti et al. “Kinetics of $\gamma$-Alumina Chlorination by Tetrachloroethylene.” In: *Thermochimica Acta* 44.3 (1981), pp. 333–336.

[51] I. Pap, I. Bertóti, and G. Mink. “TG Study on the Reaction of $\gamma$-$Al_2O_3$ by $CCl_4$. Part I. Kinetic Model for the Chlorination Process.” In: *Thermochimica Acta* 79 (1984), pp. 69–81.

[52] H. P. Alder et al. “The Chlorination of Alumina. A Comparison of the Kinetics With Different Reduction Agents.” In: *Light Metals 1979*. The Metallurgical Society of AIME, 1979, pp. 337–352.

[53] I. Szabó et al. “Kinetics of Aluminum Oxide Chlorination. 1. The Mechanism and Mathematical Model.” In: *Industrial & Engineering Chemistry Research* 30.2 (1991), pp. 292–298.

[54] D. J. Milne. “The Chlorination of Alumina and Bauxite with Chlorine and Carbon Monoxide.” In: *Proceedings. Australasian Institute of Mining and Metallurgy)* 260 (1976), pp. 23–31.

[55] S. Astutiningsih, I. Banjarnahor, and A. Zakiyuddin. “Characterization and Fabrication of Metakaolin Using Pulau Bangka Kaolin.” In: vol. 67. 2018.

[56] A. Kustov et al. “Kyanite Ore Processing by Carbochlorination.” In: *International Journal of Mineral Processing* 126 (2014), pp. 70–75.

[57] A. Grønvold. *$CO_2$-free Aluminium Production: Production of $AlCl_3$ by Carbochlorination of Kaolinite and Bauxite*. Specialisation Project. Norwegian University of Science and Technology, 2020.

[58] N. Paidimarri, U. Virendra, and S. Vedantam. “Simultaneous Recovery of Hydrogen and Chlorine from Industrial Waste Dilute Hydrochloric Acid.” In: *International Journal of Chemical Engineering* 2016.5 (2016), pp. 1–13.

[59] N. K. Verma, S. K. Khanna, and Kapila B. *Comprehensive Chemistry XI*. Laxmi, 2017.

[60] G. Hudon and D. Filippou. “Chemical Processes for the Production of Titanium Tetrachloride as Precursor of Titanium Metal.” In: *Extractive Metallurgy of Titanium*. Elsevier, 2020, pp. 47–62.

[61] A. Westerhaus. “Titanium Dioxide.” In: *Ullmann’s Encyclopedia of Industrial Chemistry*. 2006, pp. 32–52.

[62] PubChem. *Ferric chloride*. `https://pubchem.ncbi.nlm.nih.gov/compound/Ferric-chloride`. Accessed 10.07.20.

[63] P. Jameel. “Use of Ferrous Chloride to Control Dissolved Sulfides in Interceptor Sewers.” In: *Journal Water Pollution Control Federation* 31.2 (1989), pp. 230–236.

[64] S. H Fogler. *Elements of chemical reaction engineering*. 5th ed. Prentice Hall, 2016.

[65] L. Fedunik-Hofman, A. Bayon, and S. Donne. “Kinetics of Solid-Gas Reactions and Their Application to Carbonate Looping Systems.” In: *Energies* 12.2981 (2019), pp. 1–35.

[66] L. Wang et al. “Carbochlorination of Alumina and Silica from High-Alumina Fly Ash.” In: *Minerals Engineering* 130 (2019), pp. 85–91.

[67] K. Melingen. *Kinetics of Alumina Carbochlorination*. Master's thesis. Norwegian University of Science and Technology, 2020.

[68] S. H Fogler. *The Shrinking Core Model*. `http://umich.edu/~elements/5e/14chap/expanded_ch14_A.pdf`. Accessed 08.05.21.

[69] S. Yagi and D. Kunii. "Studies on Combustion of Carbon Particles in Flames and Fluidized Beds." In: *Symposium (International) on Combustion* 5.1 (1955), pp. 231–244.

[70] V. Safari et al. "A Shrinking Particle—Shrinking Core Model for Leaching of a Zinc Ore Containing Silica." In: *International Journal of Mineral Processing* 93.1 (2009), pp. 79–83.

[71] W. B. White, S. M. Johnson, and G. B. Dantzig. "Chemical Equilibrium in Complex Mixtures." In: *The Journal of Chemical Physics* 28.5 (1958), pp. 751–755.

[72] Bruker. *DIFFRAC.EVA*. Version 5.2. 2012.

[73] H. Saalfeld and M. Wedde. "Refinement of the Crystal Structure of Gibbsite, $Al(OH)_3$." In: *Zeitschrift für Kristallographie* 139.1-2 (1974). PDF 01-080-7022, pp. 129–135.

[74] H. Zheng and S. W. Bailey. "Refinement of the Nacrite Structure." In: *Clays and Clay Minerals* 42.1 (1994). PDF 04-014-5003, pp. 46–52.

[75] M. Horn, C. F. Schwerdtfeger, and E. P. Meagher. "Refinement of the Structure of Anatase at Several Temperatures." In: *Zeitschrift für Kristallographie* 136.3-4 (1972). PDF 00-021-1272, pp. 273–281.

[76] M. Antipin et al. "Electron-Density Distribution in Hematite $\alpha$-$Fe_2O_3$, from Precision X-Ray Diffraction Data." In: *Doklady Akademii nauk SSSR* 281.4 (1985). PDF 04-003-2900, pp. 854–857.

[77] J. Lewis, D. Schwarzenbach, and H. D. Flack. "Electric Field Gradients and Charge Density in Corundum, $\alpha$-$Al_2O_3$." In: *Acta Crystallographica Section A* 38.5 (1982). PDF 04-004-2852, pp. 733–739.

[78] R. S. Zhou and R. L. Snyder. "Structures and Transformation Mechanisms of the $\eta$, $\gamma$ and $\theta$ Transition Aluminas." In: *Acta Crystallographica Section B* 47.5 (1991). PDF 00-056-0457, pp. 617–630.

[79] W. Guse and H. Saalfeld. "X-Ray Characterization and Structure Refinement of a New Cubic Alumina Phase ($\sigma$-$Al_2O_3$) with Spinel-Type Structure." In: *Neues Jahrbuch für Mineralogie* 5 (1990). PDF 04-005-4662, pp. 217–226.

[80] H. C. Stumpf et al. "Thermal Transformations of Aluminas and Alumina Hydrates - Reaction with 44% Technical Acid." In: *Industrial & Engineering Chemistry* 42.7 (1950). PDF 00-004-0880, pp. 1398–1403.

[81] H. E. Swanson, R. K. Fuyat, and G. M. Ugrinic. *Standard X-ray Diffraction Powder Patterns.* Vol. 3. National Bureau of Standards Circular 539. PDF 00-046-1045. U.S. Government Printing Office, 1954.

[82] W. H. Baur. "Über die Verfeinerung der Kristallstrukturbestimmung einiger Vertreter des Rutiltyps: $TiO_2$, $SnO_2$, $GeO_2$ und $MgF_2$." In: *Acta Crystallographica* 9.6 (1956), pp. 515–520.

[83] F. Bernhard et al. “Pretulite, $ScPO_4$, a New Scandium Mineral from the Styrian and Lower Austrian Lazulite Occurrences, Austria.” In: *American Mineralogist* 83.5-6 (1998). PDF 00-051-1454, pp. 625–630.

[84] C. Foo. Personal Communication. PDF 00-070-0189. Malaysian Nuclear Agency, Bangi, Malaysia, 2019.

[85] H. D. Lutz, M. Schneider, and C. Wickel. “Neutron Powder Diffraction on Monoclinic $Li_2CrCl_4$.” In: *Zeitschrift für Kristallographie* 211.1 (1996), pp. 8–12.

[86] R. von Hodenberg and G. von Struensee. “Rokühnite, $FeCl_2 \cdot 2H_2O$, a New Mineral.” In: *Neues Jahrbuch für Mineralogie* (1980). PDF 00-025-1040, pp. 125–130.

[87] G. Varga. “The Structure of Kaolinite and Metakaolinite.” In: *Epitoanyag - Journal of Silicate Based and Composite Materials* 59.1 (2007), pp. 6–9.

[88] S. Musić, N. Filipović-Vinceković, and L. Sekovanić. “Precipitation of Amorphous $SiO_2$ Particles and Their Properties.” In: *Brazilian Journal of Chemical Engineering* 28.1 (2011), pp. 89–94.

[89] B. Zhang, K. Mackenzie, and I. Brown. “Crystalline Phase Formation in Metakaolinite Geopolymers Activated with NaOH and Sodium Silicate.” In: *Journal of Materials Science* 44.17 (2009), pp. 4668–4676.

[90] A. G. Blackman and L. R. Gahan. *Aylward and Findlay’s SI chemical data*. 7th ed. John Wiley  Sons Australia Milton, Qld, 2014.

# Appendix A

# Thermal Behaviour of Bauxite

The thermal behaviour of bauxite was investigated by TGA and DTA in a specialisation project, conducted by the author during autumn 2020[57]. About 15 mg of milled bauxite powder with a particle size of 40-212 µm was introduced to an alumina crucible and mounted into Netzsch-Gerätebau GmbH STA 449 C Jupiter Thermomicrobalance. Bauxite was analysed in synthetic air at 30 mL $min^{-1}$. The sample was heated to 1200 °C, with a heating rate of 10 °C $min^{-1}$ and kept at this temperature for 60 min, before it was cooled down at a rate of 10 °C $min^{-1}$.

Figure A.1 displays the results from the TGA and DTA. The DTA displays two endothermic peaks at 317 and 525 °C. Both endothermic peaks are accompanied by a mass loss, the mass loss of the former being more significant than the latter. It was concluded in the specialisation project that these endothermic peaks were caused by the transformation of gibbsite to boehmite, and the transformation of boehmite to $\gamma$-$Al_2O_3$, respectively. From the TGA it can be observed that all major mass losses during the heating of bauxite occur below 800 °C. A calcination temperature of 750 °C was therefore determined as suitable for bauxite. During the cooling, a sudden increase in the DTA can be observed at about 600-650 °C. This is due to an abnormality measurement of the background.

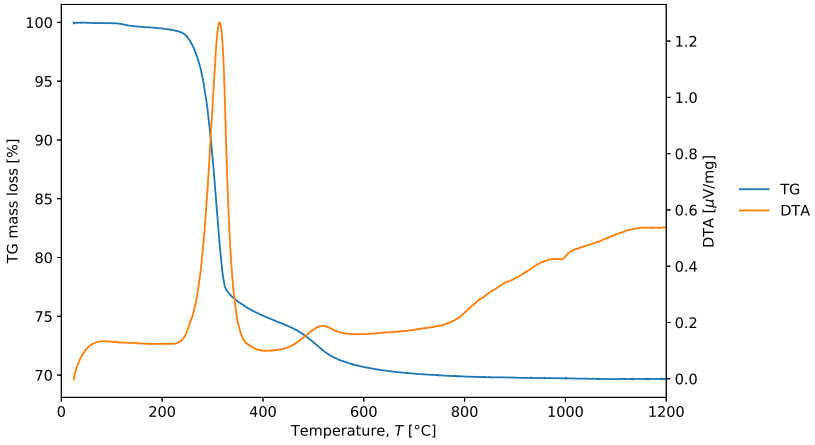


**Figure A.1:** TGA and DTA of bauxite measured synthetic air at 30 mL $min^{-1}$. A heating and cooling rate of 10 °C $min^{-1}$ was utilised.

# Appendix B

# Temperature During Calcination

Figure B.1 displays the measured temperature inside the core of the bauxite powder during calcination.

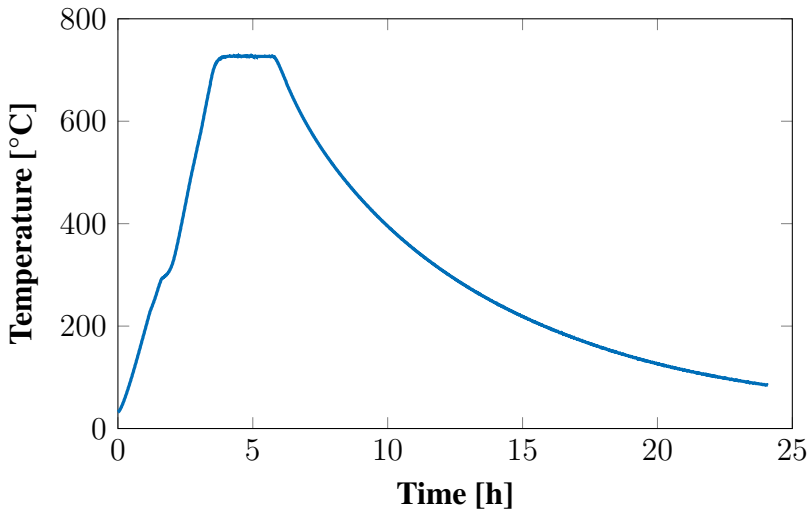


**Figure B.1:** Temperature in the bauxite powder core during calcination.

# Appendix C

# Measured Values During Carbochlorination

## C.1 Mass Loss

The measured initial and final masses of bauxite, before and after carbochlorination are given i Table C.1

**Table C.1:** Initial and final masses of bauxite, before and after carbochlorination.

| Time [min] | Reactor Height | Initial Mass [g] | Final Mass [g] |
|---|---|---|---|
| 15 | Top | 1.586 | 0.739 |
| | Middle | 1.539 | 1.349 |
| | Bottom | 1.572 | 1.407 |
| | Total | 4.697 | 3.495 |
| 45 | Top | 1.395 | 0.327 |
| | Middle | 1.465 | 0.909 |
| | Bottom | 1.459 | 1.101 |
| | Total | 4.319 | 2.337 |
| 75 | Top | 1.460 | 0.180 |
| | Middle | 1.425 | 0.502 |
| | Bottom | 1.458 | 0.977 |
| | Total | 4.343 | 1.659 |

## C.2 Changes in Bed Height

The measured initial and final powder bed heights of bauxite, before and after carbochlorination are given i Table C.2.

## C.3 Reactor Temperature

The temperature outside the reactor, at the same height as the top and bottom bed was measured during carbochlorination. Table C.3 displays the average temperatures of the top and bottom bed during carbochlorination.

**Table C.2:** Initial and final bed heights of bauxite, before and after carbochlorination.

| Time [min] | Reactor Height | Initial Height [mm] | Final Height [mm] |
|---|---|---|---|
| 15 | Top | 13 | 8 |
| | Middle | 12 | 9 |
| | Bottom | 13 | 10 |
| | Total | 38 | 27 |
| 45 | Top | 12 | 7 |
| | Middle | 12 | 8 |
| | Bottom | 12 | 6 |
| | Total | 36 | 21 |
| 75 | Top | 12 | 5 |
| | Middle | 12 | 7 |
| | Bottom | 13 | 7/2[1] |
| | Total | 37 | 21 |

**Table C.3:** Temperature of the top and bottom bed during carbochlorination.

| Time [min] | Top Bed Temperature [°C] | Bottom Bed Temperature [°C] |
|---|---|---|
| 15 | 707 | 675 |
| 45 | 700 | 666 |
| 75 | 708 | 661 |

## C.4 Pressure

The pressure developments inside the PBR during carbochlorination are displayed in Figure C.1. An initial increase in pressure is observed for all three experiment lengths. This is followed by a rapid decrease and another increase in pressure. The reason for this pressure development is most likely associated with atmosphere inside the PBR being changed from $N_2$ to a CO and $Cl_2$ mixture. The sudden pressure drops at 6, 27 and 37 min during the 75 min experiment are due to a hole being formed in the bottom bed. After 20 min carbochlorination, a steady decrease in pressure can be observed for the 45 and 75 min experiment. This steady decrease in pressure can be explained by the net decrease in gas molecules as the carbochlorination proceeds, assuming Reactions 2.1-2.5.

[1]Two values for the final powder bed height is given as a hole was formed in this bed during carbochlorination, causing the bauxite to escape to the empty bed below. The first number is the final bed height in the bottom bed, and the latter number is the final bed height of the empty bed below.

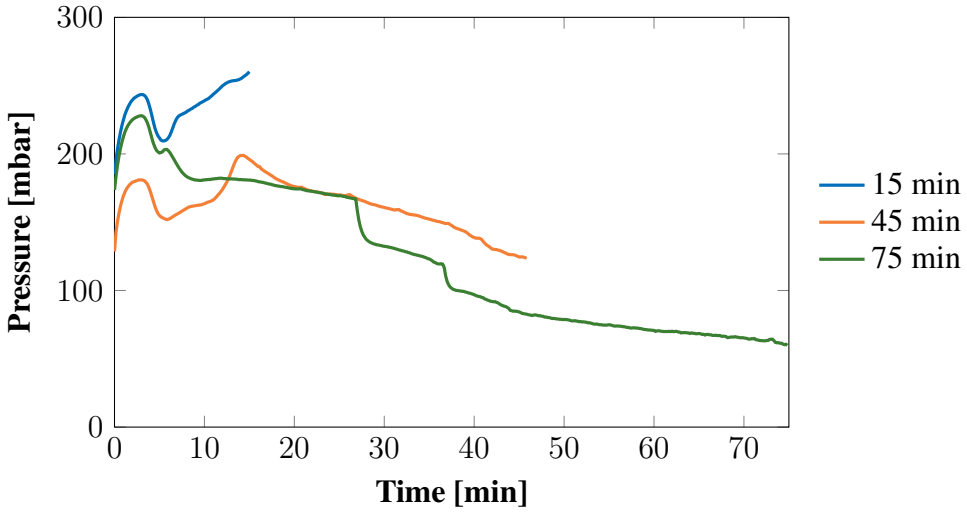


**Figure C.1:** Pressure development inside the reactor during carbochlorination of bauxite at 700 °C.

# Appendix D

# Calculation of Conversion

## D.1 Calculation of $Cl_2$ Content in the Na-OH Scrubber

During carbochlorination, any unreacted $Cl_2$ coming out of the PBR will be transported to the NaOH-scrubber, as it is a non-condensable gas at RT. In the NaOH-scrubber it will react according to

$$Cl_2 + 2\,OH^- \rightleftharpoons ClO^- + Cl^- + H_2O\,. \tag{D.1}$$

10 mL of the NaOH-scrubber was sampled during the 45 and 75 min carbochlorination experiments, and analysed by iodometry to check for any $Cl_2$ slip. These 10 mL samples (sample X) were then diluted to 100 mL (sample Y) and a new sample of 10 mL (sample Z) was made from the diluted solution. This sample was mixed with an excess of acidified KI to allow following reaction to react to completion,

$$ClO^- + 2\,I^- + 2\,H^+ \rightleftharpoons I_2 + Cl^- + H_2O\,. \tag{D.2}$$

The produced $I_2$ was then measured by iodometry with 0.01108 mol $L^{-1}$ $S_2O_3{}^{2-}$, according to

$$I_2 + 2\,S_2O_3{}^{2-} \rightleftharpoons 2\,I^- + S_4O_6{}^{2-}\,. \tag{D.3}$$

The amount of $I_2$, produced in Reaction D.2 could then be calculated

$$n_{I_2} = \frac{1}{2} \cdot n_{S_2O_3{}^{2-}} = \frac{1}{2} \cdot c_{S_2O_3{}^{2-}} \cdot V_{S_2O_3{}^{2-}} \tag{D.4}$$

where $n_{S_2O_3{}^{2-}}$ is the amount of $S_2O_3{}^{2-}$ used during the titration, $c_{S_2O_3{}^{2-}}$ is the concentration of $S_2O_3{}^{2-}$ and $V_{S_2O_3{}^{2-}}$ is the volume of $S_2O_3{}^{2-}$ used during the titration. According to Reaction D.2, the amount of $ClO^-$ in sample Z is given by

$$n^{Z}_{ClO^-} = n_{I_2}. \tag{D.5}$$

The $ClO^-$ concentraion of sample Z is given by

$$c^{Z}_{ClO^-} = \frac{n^{Z}_{ClO^-}}{V^{Z}} = \frac{n_{I_2}}{10\ \text{mL}} \tag{D.6}$$

where $V^Z$ is the volume of sample Z. As this sample is obtained by extracting 10 mL from sample Y, it follows that the concentration of sample Y is given by

$$c^{Y}_{ClO^-} = c^{Z}_{ClO^-}\,. \tag{D.7}$$

Sample Y is created by diluting sample X, and the amount of $ClO^-$ in sample X can therefore be calculated as

$$n^{X}_{ClO^-} = c^{Y}_{ClO^-} \cdot V^{Y} = c^{Y}_{ClO^-} \cdot 100\ \text{mL} \tag{D.8}$$

where $V^{Y}$ is the volume of sample Y. The concentration of sample X is given by

$$c^{X}_{ClO^-} = \frac{n^{X}_{ClO^-}}{V^{X}} = \frac{n^{X}_{ClO^-}}{10\ \text{mL}} \tag{D.9}$$

where $V^{X}$ is the volume of sample X. As sample X is extracted directly from the NaOH-scrubber, their $ClO^-$ concentrations are the same, and the amount of $ClO^-$ in the NaOH-scrubber is given by

$$n^{\text{NaOH-scrubber}}_{ClO^-} = c^{X}_{ClO^-} \cdot V^{\text{NaOH-scrubber}} \tag{D.10}$$

where $V^{\text{NaOH-scrubber}}$ is the volume of the NaOH-scrubber. According to Reaction D.1 the amount of $Cl_2$ absorbed in the NaOH-scrubber is given by

$$n^{\text{NaOH-scrubber}}_{Cl_2} = n^{\text{NaOH-scrubber}}_{ClO^-}. \tag{D.11}$$

As the carbochlorination experiments proceed, the volume of the NaOH-scrubber decreases as more samples are extracted. For each sample extracted a small amount of $ClO^-$ is also removed from the scrubber. The amount of $Cl_2$ absorbed in the NaOH-scrubber after $i$ samples can therefore be calculated as

$$n^{\text{NaOH-scrubber}}_{i,\,Cl_2} = n^{X}_{i,\,ClO^-} + \left(V^{\text{NaOH-scrubber}} - (i-1)V^{X}\right) + \sum_{i=2}^{i-1} n^{X}_{i-1,\,ClO^-}. \tag{D.12}$$

Prior to all the carbochlorination experiments, the NaOH-scrubber was sampled to calibrate the amount of $Cl_2$ absorbed. The sample corresponding to $i = 1$ in Equation D.12, is this calibration sample, which can be written as

$$n^{\text{calibration}}_{Cl_2} = n^{\text{NaOH-scrubber}}_{1,\,Cl_2}. \tag{D.13}$$

The amount of unreacted $Cl_2$ absorbed in the NaOH-scrubber after extracting $i$ samples can then be calculated as

$$n^{\text{unreacted}}_{i,\,Cl_2} = n^{\text{NaOH-scrubber}}_{i,\,Cl_2} - n^{\text{calibration}}_{Cl_2}. \tag{D.14}$$

The volumes of $S_2O_3^{2-}$ used during the titration of the NaOH-scrubber samples from the 45 and 75 min carbochlorination are given i Table D.1. A sample was also obtained after the reactor setup had been purged with $N_2$ after the carbochlorination. The volumes of $S_2O_3^{2-}$ used during the titration of the NaOH-scrubber of these samples were 0.95 and 2.9 mL for the 45 and 75 min carbochlorination, respectively.

**Table D.1:** Volume of $S_2O_3^{2-}$ used during the titration of the NaOH-scrubber samples from the 45 and 75 min carbochlorination

| Time [min] | Volume of $S_2O_3^{2-}$ [mL] | |
|---|---|---|
| | 45 min Carbochlorination | 75 min Carbochlorination |
| 0 (calibration) | 0.05 | 0.25 |
| 5 | 0.05 | 0.25 |
| 10 | 0.1 | 0.3 |
| 15 | 0.1 | 0.3 |
| 20 | 0.15 | 0.4 |
| 25 | 0.25 | 0.5 |
| 30 | 0.35 | 0.6 |
| 35 | 0.55 | 0.9 |
| 40 | 0.6 | 0.95 |
| 45 | 0.75 | 1.25 |
| 50 | | 1.45 |
| 55 | | 1.6 |
| 60 | | 1.95 |
| 65 | | 2.05 |
| 70 | | 2.45 |
| 75 | | 2.6 |

## D.2 Calculation of $Cl_2$ Conversion

During the carbochlorination experiments, a $Cl_2$ flow rate of 30 NmL $min^{-1}$, was utilised. The amount of $Cl_2$ added after time $t$, can be calculated as

$$n^{\text{in}}_{\text{Cl}_2}(t) = \frac{Qtp_{atm}}{10^6 RT} \tag{D.15}$$

where $Q$ is the flow rate of $Cl_2$, $p_{atm}$ is the atmospheric pressure equal to 101 325 Pa, $R$ is the gas constant and $T$ is the gas temperature of 0 °C.

The NaOH-scrubber was sampled at a constant rate during the carbochlorination experiments. Given that sample $i = 1$ is the calibration sample, the time and sample number $i$ can be related by

$$t = (i - 1)dt \tag{D.16}$$

where $dt$ is the time between two samples. For the 45 and 75 min experiment, $dt = 5$ min.

The conversion of $Cl_2$ can then be calculated as

$$X_{\text{Cl}_2} = \frac{n^{\text{in}}_{\text{Cl}_2} - n^{\text{unreacted}}_{i,\,\text{Cl}_2}}{n^{\text{in}}_{\text{Cl}_2}} \cdot 100\%. \tag{D.17}$$

## D.3 Calculation of Bauxite Conversion

The bauxite conversion was calculated by two different methods,

- by measuring the amount of $Cl_2$ in the NaOH-scrubber and
- measuring the bauxite mass loss during carbochlorination.

### D.3.1 Conversion Based on the Amount of $Cl_2$ in the NaOH-Scrubber

The amount of reacted bauxite can be related to the amount of reacted $Cl_2$ by the molar mass of bauxite and the stochiometric coefficient of $Cl_2$ during bauxite carbochlorination. Therefore these two values must be estimated before the conversion can be calculated.

#### Calculation of the Molar Mass of Bauxite

The molar mass of bauxite was calculated using the molar masses and weight percentages of the major constituents of bauxite; $Al_2O_3$, $SiO_2$, $TiO_2$ and $Fe_2O_3$. As carbochlorination of bauxite proceeded, the chemical composition of bauxite changed, resulting in a changed molar mass. The molar mass was therefore calculated as a function of time. Assuming the composition profile given in Figure 4.11, the molar mass of bauxite was calculated as

$$Mm_{\text{bauxite}}(t) = \sum_A Mm_A \cdot \text{wt\% } A(t) \tag{D.18}$$

where $t$ is time, $Mm_A$ is the molar mass of substance $A$ and wt% $A(t)$ is the weight percentage of substance $A$ at time $t$. All molar masses are obtained from [90]. The resulting molar mass of bauxite is given in Figure D.1.

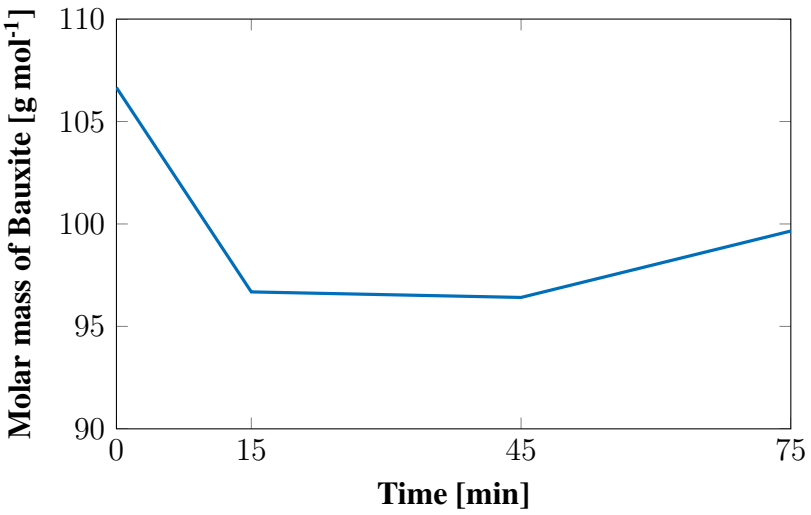


**Figure D.1:** Molar mass of bauxite as a function of time.

### Calculation of the Stoichiometric $Cl_2$ Coefficient

Carbochlorination of the calcined bauxite investigated in this work, can be expressed as

$$\begin{aligned} \text{wt\%}Al_2O_3 + \text{wt\%}SiO_2 + \text{wt\%}TiO_2 + \text{wt\%}Fe_2O_3 + xCl_2 + yCO \\ \longrightarrow AlCl_3 + SiCl_4 + TiCl_4 + FeCl_3 + yCO_2 \end{aligned} \tag{D.19}$$

where $x$ is the stoichiometric coefficient of $Cl_2$, $y$ is the stoichiometric coefficient of CO and $CO_2$. As the carbochlorination proceeds, the wt% of the reactant oxides changes as a function of time. This results in the stoichiometric coefficients $x$ and $y$ also changing as a function of time. Assuming the composition profile given in Figure 4.11, the stoichiometric coefficient of $Cl_2$ was calculated as

$$x(t) = \sum_A x_A \cdot \text{wt\% } A(t) \tag{D.20}$$

where $x_A$ is the stoichiometric coefficient of $Cl_2$ during carbochlorination of substance $A$. For the bauxite investigated in this work, the major constituents $A$ were $Al_2O_3$, $SiO_2$, $TiO_2$ and $Fe_2O_3$. The stoichiometric $Cl_2$ coefficients of $Al_2O_3$, $SiO_2$ and $TiO_2$ are 3, 2 and respectively, assuming Reactions 2.1-2.5. As seen in Reaction 2.4 and 2.5, $Fe_2O_3$ has two possible reaction pathways, giving two possible stoichiometric $Cl_2$ coefficients; 3 and 2. An average stoichiometric $Cl_2$ coefficient of 2.5 was therefore assumed for the carbochlorination of $Fe_2O_3$. The resulting stoichiometric $Cl_2$ coefficient of bauxite is given in Figure D.2.

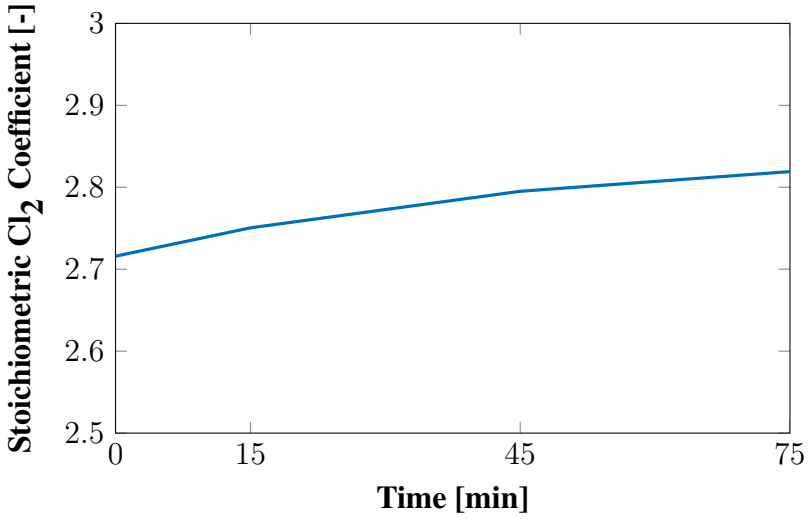


**Figure D.2:** Stoichiometric $Cl_2$ coefficient of bauxite as a function of time.

### Conversion

The conversion of bauxite, based on the amount of reacted $Cl_2$ is given by

$$X_{\text{bauxite}}^{Cl_2-\text{input}} = \frac{\left(n_{Cl_2}^{\text{in}} - n_{i,\,Cl_2}^{\text{unreacted}}\right) \cdot Mm_{\text{bauxite}}}{x \cdot m_{\text{bauxite}}^{i}} \cdot 100\% \tag{D.21}$$

where $m_{\text{bauxite}}^{i}$ is the initial mass of bauxite, before carbochlorination.

### D.3.2 Conversion Based on Mass Loss

The conversion of bauxite based on the measured mass loss is given by

$$X_{\text{bauxite}}^{\text{weight}} = \frac{m_{\text{bauxite}}^{i} - m_{\text{bauxite}}^{f}}{m_{\text{bauxite}}^{i}} \cdot 100\% \tag{D.22}$$

where $m_{\text{bauxite}}^{f}$ is the final mass of bauxite, after carbochlorination.

# Appendix E

# Calculation of Bed Height Reduction

The bed height reduction during carbochlorination was calculated as

$$\text{Bed height reduction} = \frac{h^i - h^f}{h^i} \cdot 100\% \tag{E.1}$$

where $h^i$ is the initial powder bed height and $h^f$ is the final powder bed height.

# Appendix F

# XRF Results

Table F.1 displays the full results from the XRF measurement of the calcined bauxite. Tables F.2-F.4 displays the full results form the XRF measurements of the bauxites carbochlorinated for 15, 45 and 75 min respectively.

**Table F.1:** Chemical composition of the calcined bauxite, measured by XRF.

| | **Chemical composition [wt%]** |
|---|---|
| **$Na_2O$** | 0 |
| **MgO** | 0.345 |
| **$Al_2O_3$** | 62.7 |
| **$SiO_2$** | 14.0 |
| **$P_2O_5$** | 0.263 |
| **$SO_3$** | 0.138 |
| **Cl** | 0.239 |
| **$K_2O$** | 0.109 |
| **CaO** | 0.056 |
| **$TiO_2$** | 2.45 |
| **$Cr_2O_3$** | 0.465 |
| **$Mn_2O_3$** | 0.127 |
| **$Fe_2O_3$** | 20.3 |
| **ZnO** | 0 |
| **SrO** | 0.045 |

Table F.2-F.4 displays the full results form the XRF measurements of the bauxites carbochlorinated for 15, 45 and 75 min respectively.

**Table F.2:** Chemical composition of bauxite carbochlorinated for 15 min, measured by XRF.

| | Chemcial Composition [wt%] | | |
|---|---|---|---|
| | **Top** | **Middle** | **Bottom** |
| **$Na_2O$** | 0.099 | 0.078 | 0 |
| **MgO** | 0.314 | 0.351 | 0.376 |
| **$Al_2O_3$** | 80.2 | 79.3 | 72.6 |
| **$SiO_2$** | 10.9 | 10.9 | 16.6 |
| **$P_2O_5$** | 0.316 | 0.236 | 0 |
| **$SO_3$** | 0.098 | 0.096 | 0.119 |
| **Cl** | 1.43 | 1.73 | 1.55 |
| **$K_2O$** | 0.102 | 0.096 | 0.131 |
| **CaO** | 0.110 | 0.134 | 0.074 |
| **$TiO_2$** | 2.14 | 2.56 | 2.87 |
| **$Cr_2O_3$** | 0.410 | 0.332 | 0.330 |
| **$Mn_2O_3$** | 0.016 | 0.032 | 0.042 |
| **$Fe_2O_3$** | 4.68 | 4.89 | 5.82 |
| **ZnO** | 0 | 0 | 0 |
| **SrO** | 0.023 | 0.048 | 0.039 |

**Table F.3:** Chemical composition of bauxite carbochlorinated for 45 min, measured by XRF.

| | Chemcial Composition [wt%] | | |
|---|---|---|---|
| | **Top** | **Middle** | **Bottom** |
| **$Na_2O$** | 0 | 0 | 0.272 |
| **MgO** | 0.345 | 0.485 | 0.427 |
| **$Al_2O_3$** | 62.7 | 85.3 | 81.0 |
| **$SiO_2$** | 14.0 | 7.77 | 10.2 |
| **$P_2O_5$** | 0.263 | 0.417 | 0.377 |
| **$SO_3$** | 0.138 | 0.221 | 0.143 |
| **Cl** | 0.239 | 1.84 | 2.34 |
| **$K_2O$** | 0.109 | 0.146 | 0.135 |
| **CaO** | 0.056 | 0.413 | 0.300 |
| **$TiO_2$** | 2.45 | 1.62 | 2.33 |
| **$Cr_2O_3$** | 0.465 | 0.342 | 0.332 |
| **$Mn_2O_3$** | 0.127 | 0 | 0.023 |
| **$Fe_2O_3$** | 20.26 | 2.67 | 3.08 |
| **ZnO** | 0 | 0 | 0 |
| **SrO** | 0.045 | 0.031 | 0.041 |

**Table F.4:** Chemical composition of bauxite carbochlorinated for 75 min, measured by XRF.

| | **Chemcial Composition [wt%]** | | |
|---|---|---|---|
| | **Top** | **Middle** | **Bottom** |
| **$Na_2O$** | 0 | 0.159 | 0 |
| **MgO** | 0.356 | 0.332 | 0.429 |
| **$Al_2O_3$** | 75.7 | 84.1 | 87.0 |
| **$SiO_2$** | 9.70 | 5.54 | 5.40 |
| **$P_2O_5$** | 0.216 | 0.069 | 0.191 |
| **$SO_3$** | 0.069 | 0.492 | 0.179 |
| **Cl** | 1.24 | 1.38 | 1.71 |
| **$K_2O$** | 0.159 | 0.096 | 0.154 |
| **CaO** | 0.317 | 0.128 | 0.146 |
| **$TiO_2$** | 2.48 | 2.42 | 1.66 |
| **$Cr_2O_3$** | 0.056 | 0.388 | 0.281 |
| **$Mn_2O_3$** | 0.040 | 0.029 | 0.019 |
| **$Fe_2O_3$** | 10.1 | 5.88 | 3.54 |
| **ZnO** | 0 | 0 | 0 |
| **SrO** | 0.038 | 0.026 | 0.013 |

# Appendix G

# SEM Micrographs of Carbochlorinated Bauxite

The remaining secondary SEM micrographs of the carbochlorinated bauxites, not presented in Section 4.8, are presented in Figure G.1-G.5. Only the micrographs with low and medium magnification are displayed.

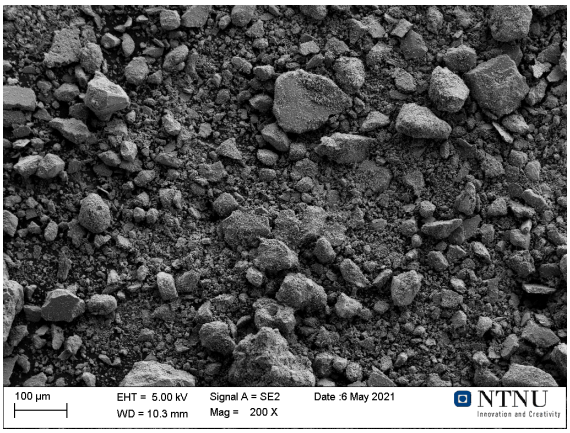


**(a)** 500 X magnification.

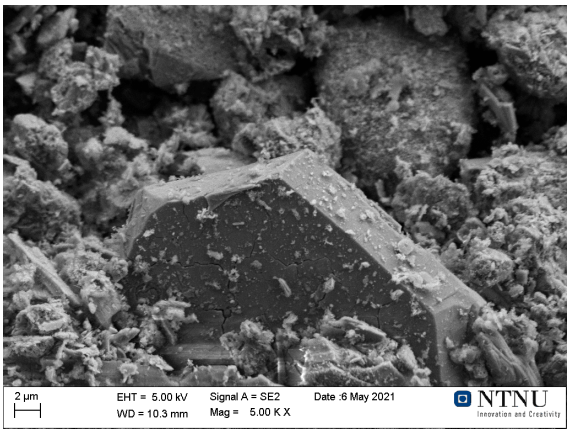


**(b)** 5k X magnification.

**Figure G.1:** Secondary SEM micrographs of bauxite from the middle bed after carbochlorination for 15 min.

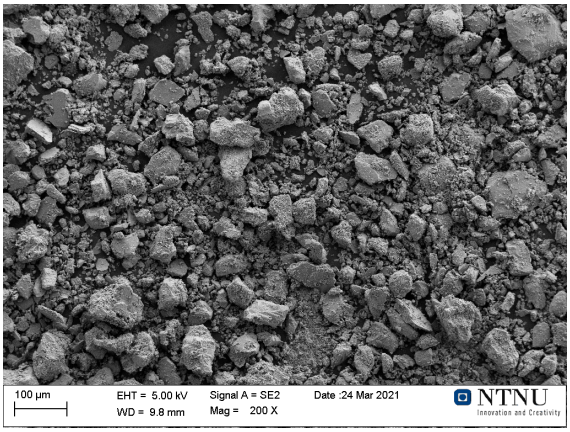


**(a)** 500 X magnification.

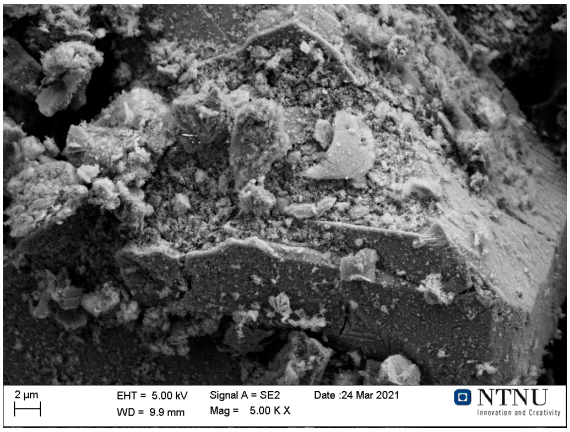


**(b)** 5k X magnification.

**Figure G.2:** Secondary SEM micrographs of bauxite from the middle bed after carbochlorination for 45 min.

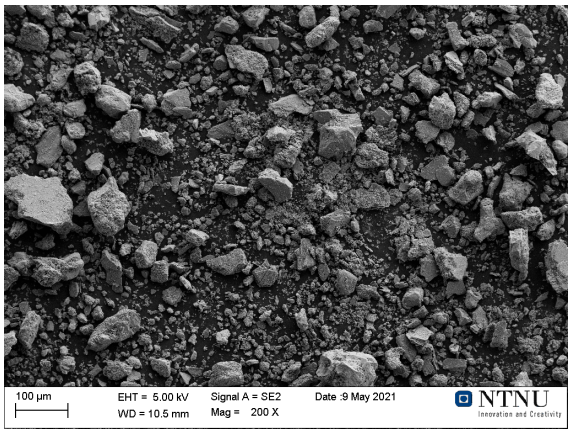


**(a)** 500 X magnification.

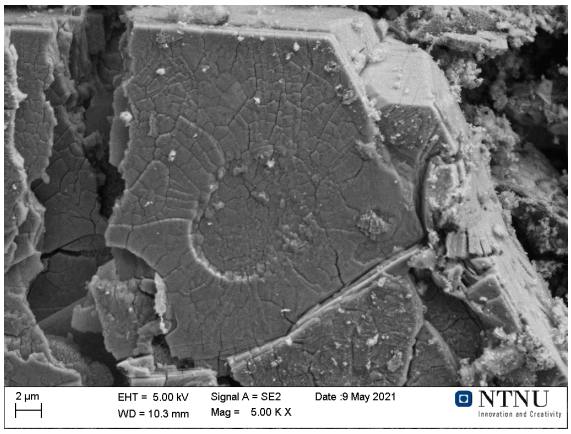


**(b)** 5k X magnification.

**Figure G.3:** Secondary SEM micrographs of bauxite from the middle bed after carbochlorination for 75 min.

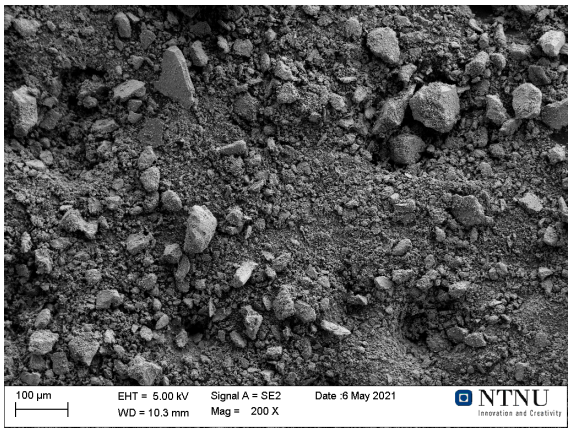


**(a)** 500 X magnification.

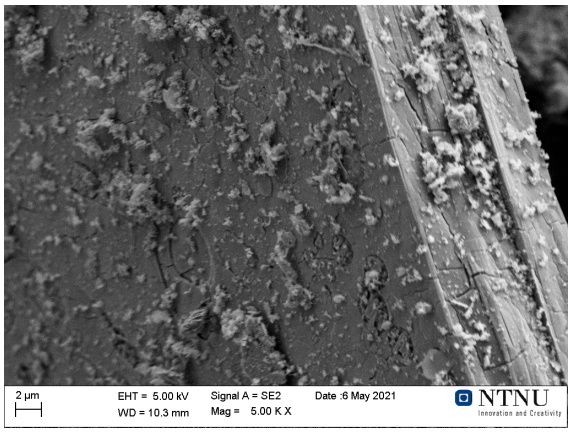


**(b)** 5k X magnification.

**Figure G.4:** Secondary SEM micrographs of bauxite from the bottom bed after carbochlorination for 15 min.

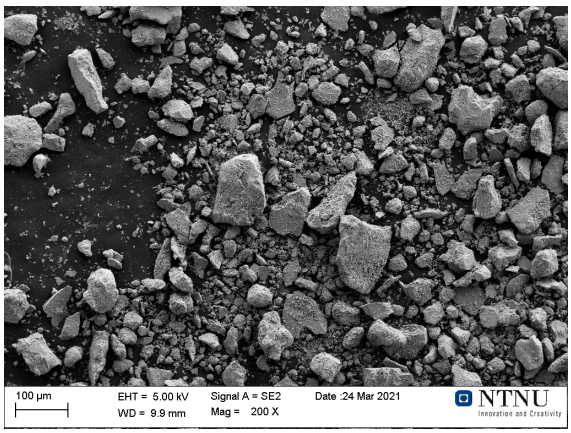


**(a)** 500 X magnification.

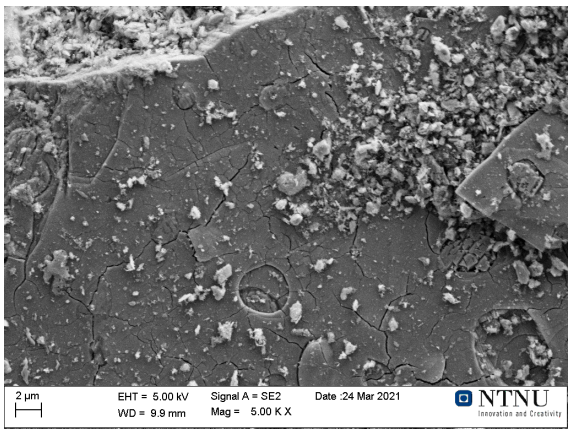


**(b)** 5k X magnification.

**Figure G.5:** Secondary SEM micrographs of bauxite from the bottom bed after carbochlorination for 45 min.

Amalie Grønvold

# $CO_2$-Free Aluminium Production: Production of $AlCl_3$ by Carbochlorination of Bauxite

NTNU
Norwegian University of
Science and Technology